WRDC-TR-89-3032

EFFECTS OF POROSITY ON DELAMINATION OF RESIN-MATRIX COMPOSITES

J.F. Mandell and J.-Y. Tsai
Department of Materials Science and Engineering
Massachusetts Institute of Technology
Cambridge, Massachusetts 02139

April 20, 1990

Final Report for Period June 1984 - June 1987

FLIGHT DYNAMICS LABORATORY
WRIGHT RESEARCH DEVELOPMENT CENTER
AIR FORCE SYSTEMS COMMAND
WRIGHT PATTERSON AIR FORCE BASE, OHIO 45433-6553

NOTICE

When Government drawings, specifications, or other data are used for any purpose other than in connection with a definitely Government-related procurement, the United States Government incurs no responsibility or any obligation whatsoever. The fact that the government may have formulated or in any way supplied the said drawings, specifications, or other data, is not to be regarded by implication, or otherwise in any manner construed, as licensing the holder, by any other person or corporation; or as conveying any rights or permission to manufacture, use, or sell any patented invention that may in any way be related thereto.

This report is releasable to the National Technical Information Service (NTIS). At NTIS, it will be available to the general public, including foreign nations.

This technical report has been reviewed and is approved for publication.

George P. Sendeckyj

GEORGE P. SENDECKYJ, Aero Engr
Fatigue, Fracture & Reliability Gp
Structural Integrity Branch

Joseph G. Burns

JOSEPH G. BURNS, Tech Mgr
Fatigue, Fracture &
Reliability Gp
Structural Integrity Branch

FOR THE DIVISION

William P. Johnson

WILLIAM P. JOHNSON
Actg Chief, Structural Integrity Branch
Structures Division

If your address has changed, if you wish to be removed from our mailing list, or if the addressee is no longer employed by your organization, please notify WL/FIBEC, WPAFB, OH 45433-6553 to help us maintain a current mailing list.

Copies of this report should not be returned unless return is required by security considerations, contractual obligations, or notice on a specific document.

REPORT DOCUMENTATION PAGE

Form Approved
OMB No. 0704-0188

1. AGENCY USE ONLY *(Leave blank)*	2. REPORT DATE	3. REPORT TYPE AND DATES COVERED
	20 Apr 90	Final Report June 84-June 87

4. TITLE AND SUBTITLE

Effects of Porosity on Delamination of Resin-Matrix Components

5. FUNDING NUMBERS

C F33615-84-C-3205
PE 61102F
PR 2302
TA N1
WU 25

6. AUTHOR(S)

J.F. Mandell and J.Y. Tsai

7. PERFORMING ORGANIZATION NAME(S) AND ADDRESS(ES)

Department of Materials Science and Engineering
Massachusetts Institute of Technology
Cambridge, Massachusetts 02139

8. PERFORMING ORGANIZATION REPORT NUMBER

9. SPONSORING/MONITORING AGENCY NAME(S) AND ADDRESS(ES)

Flight Dynamics Laboratory (WL/FIBEC)
Wright Research Development Center
Wright Patterson Air Force Base OH 45433-6553

George Sendeckyj (513/255-6104)

10. SPONSORING/MONITORING AGENCY REPORT NUMBER

WRDC-TR-89-3032

11. SUPPLEMENTARY NOTES

12a. DISTRIBUTION/AVAILABILITY STATEMENT

Approved for public release; distribution unlimited

12b. DISTRIBUTION CODE

13. ABSTRACT *(Maximum 200 words)*

The effect of porosity and moisture content on delamination resistance of unidirectional AS4/3501-6 graphite/epoxy composite was investigated. The results show that the effects of porosity on delamination resistance depend strongly on the mode of loading. Mode I static G_{Ic} levels can be significantly increased at high porosity due to the formation of multiple crack fronts, while G_{IIc} is almost independent of porosity level. Moisture saturation increases the amount of fiber bridging in Mode I, and so increases G_{Ic}, particularly at low porosity; G_{IIc} is reduced slightly by moisture saturation. In fatigue, the increases in G_{Ic} from high porosity and moisture saturation are offset by a lower fatigue crack growth exponent, so that the crack growth rates approach those of the dry control at low cyclic G_I levels. Mode II fatigue crack growth was not strongly affected by porosity level, but the crack growth exponent was lower under wet, high porosity conditions.

14. SUBJECT TERMS

Composite materials, graphite/epoxy, porosity, delamination, moisture effect, interlaminar shear strength, fatigue

15. NUMBER OF PAGES

152

16. PRICE CODE

17. SECURITY CLASSIFICATION OF REPORT	18. SECURITY CLASSIFICATION OF THIS PAGE	19. SECURITY CLASSIFICATION OF ABSTRACT	20. LIMITATION OF ABSTRACT
Unclassified	Unclassified	Unclassified	UL

FOREWORD

This work was performed under Air Force Contract F33615-84-C-3205, sponsored by the Air Force Systems Command, Aeronautical Systems Div/PMRNA, Wright-Patterson AFB, OH 45433. Dr. George P. Sendeckyj, WRDC/FIBE, was the Air Force Program Monitor.

The study was conducted in the Department of Materials Science and Engineering, Massachusetts Institute of Technology, Cambridge, MA 02139. The Principal Invesitgator was Dr. John F. Mandell, and William J. Tsai served as the graduate student Research Assistant throughout the project. The work was performed during the period 6/4/84 through 6/3/87.

TABLE OF CONTENTS

LIST OF TABLES

LIST OF ILLUSTRATIONS

SECTION I

INTRODUCTION

Porosity in epoxy matrix composites may be introduced either by air entrapment during resin mixing or laminate fabrication, or else by nucleation from volatiles (including moisture) during processing[1]. While porosity may generally be kept well below 1 percent under ideal conditions, the fabrication of thick, complex parts or certain higher production rate processes may lead to much higher porosity levels. Improvements in inspection methods, particularly for thick parts, have also led to difficult questions on acceptance criteria for parts containing some regions of high porosity.

Early studies by Greszczuk[2] and others[3,4], established that porosity in resin matrix composites reduces the interlaminar shear strength and compressive strength. Typical results from many studies of glass and graphite fiber reinforced epoxies show a loss of about 7 percent of the interlaminar shear strength for each 1 percent increase in porosity up to roughly 4% porosity, beyond which the rate of strength loss usually decreases[5]. In addition to the widely recognized effect of porosity on shear and compressive strengths, concern has also been expressed over interactions of moisture and porosity possibly generating high osmotic pressures in the presence of common contaminates such as sodium ions[6]. In torsional tests of graphite/epoxy, Hancox[7] has also reported that the effects of hot wet conditioning on shear properties were not reversed by subsequent drying if the porosity content was above 1 percent, which was hypothesized as due to changes in the condition of the interface.

Technology surrounding the study of interlaminar properties has improved markedly in recent years, with greater emphasis on delamination crack propagation in addition to interlaminar shear strength. Recent studies have included interlaminar fatigue crack propagation under Mode I (opening) and Mode II (forward shear) loading[8,9].

The purpose of this study was to reexamine the effects of porosity in the context of fracture mechanics based treatment of delamination resistance including fatigue, and to explore the interaction of moisture with the observed porosity effects. More generally, the goal was to improve on the ability to assess the extent to which porosity would compromise the delamination resistance of composite parts.

SECTION II

EXPERIMENTAL METHODS

2.1 MATERIALS, MOLDING, AND INTRODUCTION OF POROSITY

The material used throughout this study was AS4/3501-6 grpahite/epoxy from Hercules, Inc. Unidirectional prepreg tape 300-mm-wide (Lot. No. 3270) was cut into 150-mm-long pieces and layed up by hand to the required number of plies; all plates were unidirectional with 8, 12, or 24 plies, having a nominal ply thickness of 0.125 mm in most cases. Teflon coated glass fabric (0.075 mm thickness) was used as a crack starter strip, embedded between plies at the mid-thickness. Curing was done by either autoclave or hot press following the manufacturer's suggested cure cycle (given in Figure 1), and using the molding system shown in Figure 2. The arrangement of specimen types and associated starter strips is shown in Figure 3.

A number of methods were explored for introducing controlled porosity, including chemical foaming agents appropriate for epoxy, volatile organic solvents and moisture, and variations in molding conditions. Particular treatments were either brushed on to particular plies (termed embedding in the Tables) or else sprayed on. Table 1 describes particular foaming agents, and Table 2 gives various treatments, percent porosity produced, and plate identification number. Other investigators have introduced porosity by several of these methods, including AZDN[10], MEK[11], Acetone [7], water[12] and process variations[13], while the use of resin starved plies has also been successful, and has shown similar effects to naturally occurring porosity[14]. Resin starved plies were also used in the early phases of this work[15], but were not pursued in the final phase reported here due to the inconvenience of the method. As discussed later, most treatments worked to some extent, and the effects on short beam shear strength and delamination resistance were sensitive primarily to the porosity level, not to the agent used. As a result, it was decided to concentrate most of the work,

particularly fatigue studies, on three simple and representative systems, each with 12 plies: (1) an autoclave control with about 0.5 percent porosity, (2) a hot press control (no vacuum) with about 2.8 percent porosity, and (3) a hot press process with 25 percent of normal pressure and distilled water spray on each ply (about 5 g/m^2 of prepreg), with about 8.7 percent porosity. These three nominal porosity cases cover most of the porosity content range of interest and do not introduce any chemical contaminants. The water spray is applied immediately before layup of the laminate. All of the static and fatigue data for the primary materials with the exception of the autoclave control come from a single plate, and so had relatively little scatter.

2.2 CHARACTERIZATION AND CONDITIONING

The porosity content and size were determined by quantitative microscopy methods. Optical micrographs were taken of polished sections normal to the fibers at a magnification of 80 to 160X. A grid was superimposed over the micrograph, and the fraction of grid intersections falling within pores was manually determined. The resulting ratio of grid intersections falling in pores to total grid intersections is the area fraction of pores on that cross section. The results are from at least two micrographs taken from different areas, each covering an area about 1 mm^2. Porosity measurements for the three porosity cases studied in fatigue tests were determined from a number of different plates. Pore dimensions were determined from the same micrographs using a 7X magnifier with a scale.

Specimens were either conditioned in ambient (air conditioned) laboratory air, or were saturated in deionized water. Moisture content was determined by weight change with surface dried specimens. Specimens held under ambient conditions contained about 0.15 percent to 0.25 percent moisture as determined by drying in a vacuum oven at 75°C until the weight remained constant (about 17 days). Wet specimens were conditioned in 75° deionized water until their weight stopped

increasing, and were then held in room temperature deionized water until tested. Typical weight change data are given in the Appendix and will be discussed later.

The fiber volume contents were determined by nitric acid resin digestion following ASTM D-3171, assuming fiber and matrix densities of 1.799 amd 1.265 g/cm^3, respectively.

2.3 MECHANICAL TEST METHODS

2.3.1 Interlaminar Shear Strength

The interlaminar shear strength (ILSS) study used the short beam shear strength test method of ASTM D-2344. The short beams were placed on supports with a span length five times the thickness of the specimens. Mechanical testing was performed at a constant cross-head speed of 2 mm/min, and the load versus deflection was recorded. The measured peak loads were translated into ILSS using the equation

$$ILSS = 0.75P/(Wt) \quad (1)$$

where P is the peak load, W the specimen width, t the specimen thickness, and the span was 5t in all cases. The specimen is oriented such that the force is applied in the direction of the plate thickness; the specimen width was 6.4 mm in all cases.

Short beam shear fatigue tests were conducted using a servohydraulic machine with load control, a sinusoidal waveform and a force ratio, R, (P_{min}/P_{max}) of 10. Most of the tests were carried out at a frequency of 5 Hz, but one set was done at 2 Hz for comparison. The maximum deflection of the specimen, recorded by computer, was monitored as a function of cycles in the fatigue test. A plot of change in maximum deflection after the first cycle versus number of cycles is shown in Figure 4. As the cycles increase, the deflection at first increases and then becomes stabilized throughout most of the lifetime; near failure there is a rapid increase in the deflection. This rapid increase is found from microscopy study (discussed later) to correspond to development of macroscopic interlaminar cracks, and so is taken as the cycles to failure in the test.

For the wet condition test, water saturated specimens were placed inside a plastic pouch filled with deionized water. The pouch was positioned in the 3-point bending apparatus, and the short beam shear fatigue tests were conducted normally.

2.3.2 Mode I Delamination Test

A schematic diagram of the opening mode delamination test using the double cantilever beam (DCB) specimen is shown in Figure 5. The specimen includes a Teflon crack starter strip and bonded loading hinges. A strip of millimeter scale paper was bonded to the specimen edge to facilitate crack length definition. Static testing was carried out with a constant cross-head speed of 2 mm/min. Crack extention was monitored with a Bausch and Lomb stereo optical microscope with magnification range from 10X to 40X. The opening of the crack was measured from movement of the machine cross-head or piston. The load-displacement data were reduced to the form of a compliance curve to determine an experimental specimen calibration for G_I. A third degree polynominal (Figure 6) was fit to the compliance (C) versus crack length (a) values for each laminate, and dC/da was calculated for use in the Irwin strain energy release rate relationship[13]

$$G_{Ic} = (P_c^2/2W)\, \partial c/\partial a \qquad (2)$$

where P_c is the critical load for crack extension and W is the specimen width.

Mode I interlaminar fatigue crack propagation tests were run using a servohydraulic machine with load control, a sinusoidal waveform, and an R ratio (P_{min}/P_{max}) of 0.1. Most of the tests were carried out at a frequency of 5 Hz, with crack propagation observed using a stereo optical microscope. Specimens were prepared by polishing the edge and applying a layer of silver paint along the expected crack path to enhance detection of the growing crack. For the wet condition tests, a humidifier was used to direct moist air to the crack tip of a water saturated specimen. As discussed later, fatigue crack growth data were taken only after sufficient crack extension to allow the full development of the fiber bridging zone, as evidenced by a constant G_{Ic}.

2.3.3 Mode II Delamination Test

Mode II (forward shear) delamination resistance was determined using the End Notch Flexure (ENF) specimen developed by Russell and Street[8]. The ENF specimen was subjected to 3-point flexural loading pins as shown in Figure 7. The loading pins were wrapped with Teflon film to reduce friction, and the span was 40 times the specimen thickness. Specimens were prepared by polishing the specimen edges and applying a layer of silver paint along the expected crack path to enhance detection of the growing crack.

Crack propagation in this test was unstable under static loading, as the crack would jump a short distance at the critical load. After the onset of crack propagation from the initial Teflon notch, the load was released to allow for a relocation of the specimen so that the crack tip was in the original position relative to the loading pins. Each relocation produced one result: the maximum load at unstable crack propagation. Repetition of this procedure yielded several data points from each specimen. Only the natural crack tests were used to determine G_{IIc}, as the Teflon starter crack gave different results, as discussed later. The Mode II fracture energy was determined from Equation (2), utilizing a compliance versus crack length relationship derived from beam theory [8]. The bending compliance can be expressed in the form

$$C_B = (2L^3 + 3a^3)/8EWh^3 \tag{3}$$

where L = the length between the outer pin and the middle pin
a = crack length measured from the outer pin
E = longitudinal flexural modulus
W = specimen width
h = half thickness of the specimen

Inserting Eq.(3) into Eq.(2) gives the critical strain energy release rate for a Mode II delamination as

$$G_{IIc} = (9a^2 P_c^2)/16EW^2h^3 \tag{4}$$

where P_c is the critical load for crack extension.

As with the other fatigue tests, Mode II interlaminar fatigue crack propagation tests were run on a servohydraulic machine with load control using a sinusoidal waveform and an R ratio (P_{min}/P_{max}) of 10. Most of the tests were carried out at 5 Hz except for one set at 2 Hz. Following the procedures used with the short beam shear fatigue tests, the deflection was monitored by computer during cycling. The results showed that fatigue tests under load control were feasible, producing stable crack propagation, unlike the unstable growth experienced with static loading. A stroke limit was preset so that when the piston stroke exceeded a certain distance (as a result of the increase in the specimen compliance as the crack propagated), the cycling would terminate. This presetting of the stroke limit prevented the crack from growing more than a few millimeters per growth increment. The ENF specimen was then taken from the apparatus and the crack length increment was measured with a stereo optical microscope. After each such fatigue crack advance, the specimen was repositioned. A static load was applied to force the crack to jump and be arrested near the central loading pin. This ensured a straight initial crack front for the next fatigue crack growth advance. As discussed later, continued fatigue crack growth for more than a few mm resulted in very nonuniform advance across the crack front, which was avoided by growing a crack for no more than 2 mm, followed by re-establishing a new crack front by static loading. While tedious, this procedure produced consistent data.

For the wet tests, the presaturated specimen was placed inside a water filled plastic pouch, and a strip of mm scale paper was bonded onto the pouch for crack location. After each fatigue test, the specimen was taken from the pouch and the crack increment was measured under a microscope.

SECTION III

RESULTS AND DISCUSSION

3.1 MICROSTRUCTURE AND MOISTURE ABSORPTION

This section describes the microstructures of samples with various porosity levels and the moisture uptake characteristics of typical cases. Porosity was introduced by several techniques as discussed earlier, summarized in Table 2. Of these, three cases were selected for detailed study, 12AC, 12P, and 12W, having low, medium, and high porosity levels repectivley, introduced by process variations and prepreg moisture level. The pore size and shape distribution and moisture uptake characteristics are characterized for these three cases.

3.1.1 Microstructural Characteristics

The method of introducing porosity did not greatly affect either the pore morphology or the mechanical properties, for a given level of porosity. Figures 8(a)-(d) show typical micrographs of polished sections normal to the (unidirectional) fiber direction for the materials defined in Table 1. With the exception of laminate 24V, which had a very nonuniform porosity distribution, and laminates 12B, 12C, and 12E, which had a layer of residual blowing agent, most of the laminates showed a reasonably uniform distribution of porosity throughout the thickness (with some concentration at tow boundaries for high porosity levels), so that one method of porosity introduction could not be distingushed from others by visual observation of typical micrographs. The only laminates with very high porosity, 12A and 12C, contained the residual blowing agent.

The fiber contents did not vary greatly over most of the porosity range. Average fiber volume fractions were 0.69 for the autoclave control laminates (0.5 percent porosity), 0.69 for the press control laminates (2.8 percent porosity), and 0.67 for the water soaked prepreg laminates (8.7 percent

porosity). As indicated by the thickness variations in Table 3, only laminate 12C with residual blowing agent and very high porosity (29 percent) showed a strong decrease in fiber content. The three primary cases with approximately 0.5, 2.8, and 8.7 percent porosity did not vary significantly in fiber content; the 0.67 -0.69 fiber volume fraction range is at the high end for AS4/3501-6 laminates[18].

The dimensions of pores were evaluated for the three primary materials. Pore dimensions were determined manually from micrographs using a magnifier. As shown in Figure 9(a), the pore dimensions oriented approximately in the thickness and transverse directions were measured. Figures 9(b)-(e) and the Appendix give the results for individual dimensions and aspect ratios. Several observations can be made regarding these data:

(1) As summarized in Table 4, the largest pores present in a sample increase in size as the porosity content increases. The longest pores (L) are about 4 times larger at 2.8 percent porosity as compared with autoclave control samples with 0.5 percent porosity. For a sample with 8.7 percent porosity, the largest pores are about 15 times longer than for the autoclave control. The maximum pore length is roughly proportional to the overall porosity content. The maximum pore width, B, and depth, D, show similar trends but a less rapid increase with porosity content, as do the average pore dimensions in all three directions.

(2) The pore longitudinal and transverse aspect ratios, L/D and B/D, increase as pore length and width increase, since D is nearly constant. The longitudinal aspect ratio shows a flat region betwen 0 and 4 in each material, apparently due to variations in the plane where the longitudinal section was cut through the pore. At the edges, the pore may have a very small value of D if it is pinched between closely spaced fibers. Thus, the L/D aspect ratio down the center of a pore is probably about 1 to 2 for very small pores. The position of the cutting plane through the pore will also affect larger longitudinal pore aspect ratio data.

(3) Transverse aspect ratios are very similar at 0.5 and 2.8 percent porosity, but the longitudinal aspect ratios reach much larger values for the 2.8 percent porosity material.

Qualitative observation of micrographs suggests that the pore size characteristics are generally similar for similar porosity contents, regardless of the method of pore introduction. The pore sizes, shapes and distributions are also generally similar to those reported in the literature[16]. As indicated in Figure 8(e), pores observed on fracture surfaces were often somewhat larger than those found in cross sections, and some complex planar pore geometries were found particularly along individual misoriented fibers

3.1.2 Moisture Absorption

Specimens were tested either in a dry condition, representing ambient atmosphere, or in a moisture saturated condition. Table 5 gives the moisture content data for the primary materials studied. The oven dried specimens were held in a vacuum oven until the weight became constant, about 17 days for the 12-ply cases. As noted earlier, the wet specimens were first held in 75°C deionized water for 30 days (12-ply lamninates reached a constant weight after about 3 weeks), and were then held in 20°C deionized water until testing. No significant weight change was observed at any porosity level after the initial 30-day conditioning, including many specimens monitored in 20°C water for up to 9 months.

The data in Table 5a show a greater weight gain at equilibrium for the higher porosity materials, consistent with the findings in Refs. 7 and 13. Compared with the autoclave control laminates with less than 0.5 percent porosity, the material with 2.8 percent porosity gained 50 percent more weight, while the 8.7 percent porosity material gained 100% more weight. This increase in moisture gain with porosity is similar to data reported by Harper, et al,[13], for 100% R.H. conditioning of AS4/3502; their data showed a 40 to 50 percent increase in weight gain with a

porosity increase from 1 up to 5 percent porosity. While the increased weight at high porosity is very substantial considering the reduced matrix content, Table 5b indicates that it is not as great as expected if all of the pores were filled with water. If the matrix is assumed to absorb 5.9 percent moisture by weight in each case (taken from the 0.5 percent porosity case) then the pores in the two higher porosity cases appear to be about 40 percent full of water at saturation. This condition is apparently very stable with time, as indicated by the stable specimen weights in the Appendix. These curious results were further checked by Differential Scanning Calorimetry (DSC), for which raw data are given in the Appendix. DSC specimens about 3 mm square were cut from short beam or DCB specimens after conditioning, and surface dried before the tests. The small specimen size and preparation method probably expose many pores to the surface, so the data in Table 5b are only semi-quantitative in nature. Despite this, the melt peaks as the initially frozen specimens were heated past 0°C confirm the presence of liquid water at higher porosity. Again, the conclusion is that a fraction of the pore volume contains liquid water, but the DSC data suggest about 10 percent water at 2.8 percent porosity and 25 percent at 8.7 percent porosity, below that calculated from weight gain.

The distribution of liquid water in the pores was checked by testing the interior 60 percent or so of the thickness of saturated material with the surface and edge regions sanded away. Table 5b indicates that the interior material contained about the same amount of liquid water as did the overall specimen, so the water appears to be uniformly distributed through the thickness. Detailed study of this question was beyond the scope of the study, and our weight gain specimens were not large enough for precise study. However, the data consistently indicate the presence of some liquid water in some pores of saturated materials. The study by Harper, et al[13] showed that higher porosity led to higher weight gain at all conditioning humidity levels, although we find no liquid water by DSC in our ambient specimens (Appendix); The ambient materials all have about the same percent of

moisture in the resin, consistent with Ref. 13 at low moisture levels. We conclude from this that there are at least two effects:

(1) The higher porosity materials take up more moisture even in the absence of liquid water in the pores.

(2) Liquid water further increased the weight of our specimens by entering large, interconnected pore zones (Fig. 8e) exposed to the edges or surfaces of the small specimens used in our weight gain study.

The origin of (1), which is much more important, is not certain. It may be that local resin near surfaces can swell more readily due to reduced constraint. The total surface area including pores is about 30 times greater at 8.7 percent porosity than at 0.5 percent. The data for DSC and weight gain in Table 5b would be consistent if the resin gained about 10% weight on average in the 2.8 and 8.7 percent porosity cases, so that only a very small liquid water content would be present in the 2.8 percent material, while the high porosity material, with its large pores, would still have about 25 percent liquid water in the pores.

3.2 STATIC INTERLAMINAR PROPERTIES

3.2.1 Effects of Porosity on Interlaminar Shear Strength

Table 3 and Figure 10 give the results for the short beam interlaminar shear strength (ILSS) as a function of porosity level under dry conditions. While the short beam test is recognized to have many limitations, it does provide a measure of shear strength and requires only small material samples, which was convenient in this study. The failure mode was by an interlaminar crack in all cases reported, and the failure load was clearly defined by a sharp load drop. A few cases, particularly those with residual blowing agent (laminates 12A and 12C) failed initially in compression, so data from these laminates are not reported.

The data for ILSS show a general agreeement with expectations from the literature, including the autoclave control value for AS4/3501-6[18] and the trend of the data in Figure 10[5]. As noted earlier, most studies find that the ILSS decreases by about 7 percent per 1 percent porosity increase at low porosity levels, then at a decreasing rate at higher levels. Appropriate models to fit these data will be discussed later.

3.2.2 Effects of Porosity on Delamination Resistance

Table 6 gives the Mode I (G_{Ic}) and Mode II (G_{IIc}) delamination resistance for materials with various levels of delamination resistance produced by the methods listed in Table 2. As has been noted in many studies[19] the value of G_{Ic} in DCB tests tends to increase as the (stable) crack extends, reaching a plateau value after 1-2 cm of extension. Figure 11 shows G_{Ic} vs. crack extension for several materials; the plateau G_{Ic} values show some deviations as further crack extension occurs, and the G_{Ic} values in Table 6 are an average of 6-8 points from each test. The increase in G_{Ic} with crack extension has been correlated with the development of a region of fiber bridging at the crack

tip[19] which appears to be caused primarily by the nesting of fiber tows[20]. Only at very high porosity, above 20 percent, does the value of G_{Ic} drop significantly, but these materials contained layers of residual blowing agent.

The effect of increasing porosity on the Mode I delamination resistance is generally due to increase of both initial and plateau value of G_{Ic}, as shown in Table 6 and Figures 12a and 12b. Figure 13 gives micrographs of crack cross sections, which show that increase in G_{Ic} with increasing porosity level is associated with the development of multiple crack fronts, as additional cracks are initiated in regions of high porosity away from the main crack plane. The lowest level of porosity necessary to produce multiple cracks has not been explored in detail here; Ref. 23 reports no effect on G_{Ic} of 2 percent porosity.

It is difficult to differentiate precisely between multiple cracking and individual fiber bridging, but in some cases there appear to be clear distinctions. Multiple cracking usually involves the opening of other local Mode I crack zones above and below the main crack, usually separated by a tow or ply thickness. The secondary cracks are typically localized in tow-sized zones and appear to be on the order of a few mm in length. Secondary cracks have also been found to raise the Mode I peel resistance in an earlier (unpublished) study of glass/epoxy laminates which were degraded by boiling water. Similar effects of increasing GIc have also been reported to result from crack branching when off-axis plies are present[25]. Fiber bridging appears as individual fibers crossing between the crack flanks, as distinct from an intact tow or ply. The bridging effect has been associated both with nesting of tows during processing of primarily unidirectional materials [20], and also with the direction ahead of the crack tip where failure is predicted to occur based on Wu's mixed mode fracture model (which also is consistent with the absence of bridging in Mode II)[8]. The extent of bridging has also been associated with the quality of the fiber/matrix bond, with a higher bond strength for AS1 fibers producing less bridging than with AS4 fibers in 3502 epoxy[22].

The effect of high porosity in producing multiple crack fronts in the Mode I DCB test is probably of little practical consequence beyond complicating interpretation of the DCB results. We do not expect that the resulting increase in G_{Ic} has any generality for ply configurations other than unidirectional and crack growth modes other than pure Mode I, as is evident in the Mode II results.

Crack extension in the Mode II ENF specimen was noted earlier to be unstable: as the force is increased, the crack tip remains stationary until the critical condition when the crack jumps ahead to a point near the center of the specimen (Fig. 7). As a consequence, only a single G_{IIc} value is obtained from one loading sequence, and no gradual increase in crack resistance with stable extension is observed, contrary to the case with the Mode I DCB specimens. In pratice, a long specimen is used in the ENF case, and is repositioned after each crack advance so that another separate test can be conducted. The value of G_{IIc} determined on the first loading (with the Teflon starter strip) gives erroneously high values due to yielding and hackle formation in the resin-rich zone at the edge of the starter strip [23-25], so that only subsequent, natural crack tip tests were used to obtain the data reported here.

Figure 14 gives the value of G_{IIc} determined from Eq. (4) for different crack tip positions (Fig. 7). For the range of crack lengths between 0.6 and 2.4 cm, the value of G_{IIc} was unaffected by crack tip position; for shorter or longer cracks Eq. (4) is probably not accurate due to the proximity of the loading points. The results in Fig. 14 define the crack length range over which fatigue crack growth can be studied, as described later.

The values of G_{IIc} for various materials given in Table 6 and Figure 15 are insensitive to the porosity level over a broad range. As before, very high porosity above 20 percent gives very low values of G_{IIc}, but these materials contain residual blowing agent. Outside of the very high porosity cases, the G_{IIc} data are remarkably insensitive to the porosity level and to the method of introducing

the porosity (Tables 2 and 6). The fracture surfaces under static and fatigue loading are dominated by hackle formation in the matrix as reported in other studies[8,22].

3.2.3 Discussion

The data from the low porosity autoclave control material for ILSS, G_{Ic}, and G_{IIc} are consistent with the literature for unidirectional AS4/3501-6[8,9,18]. G_{IIc} is considerably higher than the initial G_{Ic} or the plateau value in most cases. As noted, increasing the porosity (below 20 percent) decreases the ILSS but increases G_{Ic} (particlularly the plateau value), while G_{IIc} is unaffected. Thus, the effects of porosity on the various static interlaminar properties are found to be inconsistent. However, the findings in each case are understandable from simple conceptual models of the interlaminar failure process.

The reason for the increase in G_{Ic} with increasing porosity has already been described as deriving from the formation of multiple crack fronts at the higher porosity levels. This is not observed in Mode II, and G_{IIc} is nearly independent of porosity content up to about 12 percent porosity. The absence of any reduction in G_{IIc} with increasing porosity does require an explanation. There are three apparent factors involved. First, the G_{IIc} value is determined at a point of crack arrest from a previous growth step. The arrest probably occurs at a local region of maximum G_{IIc}. Second, G_{IIc} is determined at this single position, from which the crack extends unstably; it does not propagate in a stable manner, which would sample zones of relatively low and high toughness. Third, if the previous crack increment did arrest in a position of low toughness, where porosity covered much of the crack front, it could advance slightly during subsequent loading to become established at a position of higher crack resistance, analagous to R-curve behavior. For the macroscopic cracks used in thc ENF test, the crack front could reestablish itself by growth equal to the longest pores, about

0.5 mm, with an apparent reduction in G_{IIc} from Eq. (4) of only 4 percent for the 25-mm crack length. Thus, the G_{IIc} value determined from the maximum force represents the local crack front position which will give the highest toughness and is not sensitive to isolated regions of lower crack resistance.

The quantitative effect of pores on the ILSS has received attention in other studies and is complex to interpret. With pores present in varying amounts, it is natural to explore the applicability of fracture mechanics to the ILSS failures. As shown in Figure 16, fracture in the ILSS specimens is not by a simple, smooth crack normal to the maximum tensile direction as in the neat resin[26]. Instead, as is recognized for shear strength or G_{II} tests[23], failure occurs by the formation of an array of local cracks in the matrix zone between fibers, oriented normal to the maximum tensile stress. These are then ruptured by the main shear-mode crack, forming a series of hackles on the surface. This produces a value of G_{IIc} which is much higher than the GIc of the neat resin or the composite. The relatively high G_{IIc} of the composite then requires a relatively large inherent flaw size before fracture mechanics can dominate the ILSS test results. Crack growth in the ILSS test is probably further resisted by the closure of Mode II cracks due to the significant normal compressive stress, once the crack reaches appreciable size.

A quantitative estimate of critical crack size in the ILSS test can be made using the measured G_{IIc} and available analyses of embedded cracks in a pure shear field. A planar circular crack in a pure shear field oriented in the plane of the ply interfaces will have a pure Mode II condition at the edges where the radius is in the logitudinal direction, with pure Mode III at the positions 90 deg. removed. The stress intensity factor at the pure Mode II edges in an isotropic material is given by [27]

$$K_{IIc} = \frac{4S_o(\pi a)^{1/2}}{\pi(2-\nu)} \tag{5}$$

where S_o is the far-field shear stress, a is the radius of the circular crack and ν is Poisson's ratio. For embedded elliptical cracks, the value of K_{II} at the tip of the long axis (assumed parallel to the length) is lower than that in Eq. (5), about 29 percent lower for an ellipse of a/b ratio = 4. Circular cracks are assumed in the calculations here to give a maximum estimate of K_{II}. While a corresponding orthotropic solution could not be located, the effects of orthotropy are not generally expected to be great if the crack length is smaller than the specimen thickness[28]. Poisson's ratio is taken as ν_{LT} = 0.30.

The value of G_{II} can be calculated from K_{II} using the following relationship[30]

$$G_{II} = \frac{A_{11}}{2}\left(\frac{A_{22}}{A_{11}} + \frac{2A_{12} + A_{66}}{2A_{11}}\right)^{1/2} K_{II}^2 \qquad (6)$$

where the A_{ij}'s are compliance terms, with 1 representing the longitudinal direction in the present case. The values of A_{ij} for the AS4/3501-6 are taken as

$$A_{11} = 7.6 \times 10^{-3}(GPa)^{-1}$$
$$A_{22} = 9.9 \times 10^{-2}(GPa)^{-1}$$
$$A_{66} = 0.18(GPa)^{-1}$$
$$A_{12} = -2.2 \times 10^{-3}(GPa)^{-1}$$

For the short beam shear test at failure, Eq. (5) reduces to

$$K_{IIc} = 1.33(ILSS)(a_c)^{1/2} \qquad (7)$$

and G_{IIc} for an embedded circular critical flaw becomes

$$G_{IIc} = 33(ILSS)^2 a_c \qquad (8)$$

where G_{IIc} is in units of J/m^2, ILSS is in MPa, and a is in meters.

If the value of G_{IIc} is taken as 450 J/m^2 (Table 6), then the crtical flaw radii for ILSS values of 115 and 60 MPa are 1.1 mm and 4.0 mm, respectively. These critical flaw dimensions are larger than the largest pores reported in Figure 8. The largest pore size observed for specimens with ILSS values corresponding to 115 and 60 MPa had lengths, L (=2a) of about 0.025 and 0.46 mm,

respectively, although larger values were found on some fracture surfaces. Thus, the lowest ILSS cases, having the largest pores, are still probably not dominated by fracture mechanics unless considerably larger pores or coalesced zones are present. It is even more likely that the lowest porosity materials do not fail by the propagation of a pore as a critical flaw. These results support the use of a flaw-insensitive, reduction in cross-sectional area model rather than one based on fracture mechanics, unless the pore size reaches several millimeters and is fairly circular or through-thickness.

A number of pore models have been proposed for correlation with shear strength data, and other models can be derived which relate more directly to the pore distributions observed in this study. Despite the questionable use of fracture mechanics for the ILSS results presented here, a brittle fracture based model proposed by Corten[31] tends to fit the data quite well, as shown in Fig. 18. Corten's model assumes that the individual pore volume varies linearly with porosity content, and that the pore linear dimension of interest, a, varies with the $V_p^{1/3}$. The assumption of linear elastic fracture mechanics then leads to the prediction that

$$ILSS = C_1(V_p)^{-1/6} \tag{9}$$

In Fig. 18, the constant, C_1, is evaluated at V_p=.028 and ILSS=85 MPa, giving a value of 46.8 MPa. Unfortunately, it is not possible to evaluate both the implied value of G_{IIc} and the pore dimension from the model.

A more direct fracture mechanics based model uses the actual maximum or average pore length, L, from Table 4, fit at the same point to evaluate the constant in

$$ILSS = C_2(a)^{-1/2} \tag{10}$$

The values of C_2 using the maximum and average observed pore lengths, respectively, are 0.91 and 0.61 MPa $m^{1/2}$. When actual pore dimensions are used, the trends of the fracture mechanics criteria are in poor agreement with the data, particularly at low porosity contents. This is most evident when using the maximum pore size for each pore content, which should be the most appropriate case. The

value of G_{IIc} backed out of C_2 for the average pore size case is 17 J/m^2, over an order of magnitude below the G_{IIc} values determined in the ENF test. Thus, as noted before, the ILSS values do not appear to be dominated by fracture mechanics applied to the pores, unless some pores exist which are much larger than those observed.

Also shown in Figure 18 are the predictions of early models by Greszczuk[2]. These models assume that no stress concentrations exist at the pores, and that the in situ matrix strength is reduced according to the reduction in cross-sectional area on the closest-packed pore planes in arrays of spheres or cylinders. All pores are assumed to be embedded in the matrix regions, arranged in the appropriate array. In the application of the models to the case where fibers are present, the reduction in ILSS due to pores is assumed to be determined by the reduction in strength of the matrix regions, independent of the fibers. The model for spherical pores in a cubic array gives

$$ILSS/ILSS_o = 1 - (\pi/4)[6V_p/\pi(1-V_f)]^{2/3} \quad (11)$$

while the cyclindrical pores in a rectangular array gives

$$ILSS/ILSS_o = 1 - [4V_p/\pi(1-V_f)]^{1/2} \quad (12)$$

where $ILSS_o$ is the value with no pores. Both of these models give reasonable agreement with the data except at high porosity values. However, the models appear to contradict the actual porosity distributions (Fig. 8); actual pores are not embedded within the matrix regions, regardless of the array questions. It appears unreasonable to assume that the pores reduce the strength of the matrix when they often cover regions larger than the typical matrix rich zones. In fact, the fibers remain well-bonded to the matrix, and carry much of the shear stress, but have been ignored in Eqs. (11) and (12). Although the resulting predictions for porosity effects imply a decrease in ILSS as the fiber content increases at a constant V_p, no experimental evidence of a clear trend with V_f could be found in the literature.

If these models are applied to the overall reduction in cross-sectinal area of the entire composite, rather than just the matrix phase, they become, respectively,

$$ILSS/ILSS = 1-(\pi/4)(6V_p/\pi)^{2/3} \quad (13)$$

for spheres, and

$$ILSS/ILSS_o = 1-(4V_p/\pi)^{1/2} \quad (14)$$

for cylinders. These equations grossly underestimate the reduction in ILSS as V_p increases (not shown in Fig. 18). The reason that these and other models with pores in well-spaced arrays underestimate the porosity effects is that many of the pores at higher porosity contents become grouped along the tow or ply boundaries (Fig. 8). Furthermore, the models are for pores of round cross section which expand in radius as V_p increases. As noted in Figure 9, the average aspect ratios reach about B/D=2.0 at 8.7 percent porosity and the largest (highest B) pores have aspect ratios of about B/D=5 to 10. A rectangular array of cylindrical pores, each with a rectangular cross section of any B/D ratio gives the following relationship

$$ILSS/ILSS_o = 1-(BV_p/D)^{1/2} \quad (15)$$

where the pores are taken to reduce the gross cross-sectional area of the composite, as in Eqs. 13 and 14. If B/D=2, Eq. (15) gives a closer fit to the data (Fig. 18) than Eqs. (13) and (14), but still is not sufficiently steep at low V_p. Again, the problem is that Eq. (15) assumes uniformly distributed pores. If the other extreme is considered, and the pores are all assumed to be located at ply boundaries, an overestimate of porosity effects at high V_p results. With cylindrical pores of rectangular cross section B x D assumed to be distributed only along ply boundaries, where the ply thickness is t, then

$$ILSS/ILSS_o = 1 - t\,V_p/D \quad (16)$$

independent of B/D. For the present case, t = 0.125 mm and the average D is about 0.0128 mm for V_p = 8.7 percent. Here, the pore effect is a reduction by about 10 percent of $ILSS_o$ per 1.0 percent pores, reaching zero strength at 10 percent pores (Fig. 18).

The actual pore distributions in Fig. 8 at low porosity involve widely distributed pores, while at high porosity they involve an apparent bidistribution, with some pores concentrated at tow and ply boundaries, and others randomly distributed. These are similar to distributions reported in the literature[7]. The pore distributions at the boundaries are complicated by the tilt of the tow boundaries and the fact that the pores concentrate only along the matrix-rich zones of the boundary. The most important result is the presence of large regions without many pores, which appear to keep the reduction in area along any boundary zone from rising much above 40-50 percent at 8.7 percent porosity. Furthermore, these regions have closely packed fibers and probably carry a relatively greater portion of the shear loads than do the matrix rich zones where the pores concentrate. A much more thorough characterization of the pore distributions would be necessary to accurately model these effects, and the distributions are probably sensitive not only to porosity level but to factors like ply configuration, reinforcement style and processing method.

The key question for this part of the study is whether the ILSS is reduced with increasing porosity simply as a result of the reduction in cross-sectional area. The model trends from Eqs. (15) and (16) in Fig. 18 indicate that a combination of boundary pores, distributed pores, and low porosity domains could result in a combined model to fit the ILSS data, but much more thorough characterization would be required to meaningfully apportion the size, shape and amount of porosity in each region as a function of pore content. Instead, the most severe reduction in cross-sectional area has been determined experimentally for the primary materials. It was assumed that failure would occur by a crack wandering across the specimen, through the highest porosity zones. The greatest reduction in area due to pores along such a potential failure path was determined from the same

micrographs used to generate the pore size data. Figure 19a shows typical paths marked on micrographs. The lines shown in Fig. 18 for this approach assume that

$$ILSS/ILSS_o = 1-(W_p/W_T)(W_o/W_T) \quad (17)$$

where W_o is the nominal, straight line width of the section, W_T is the total length of the selected (wandering) path, and W_p is the width taken up by pores along the selected line. Table 8 gives the predicted values for the worst paths on the micrographs. The empirical trend from Eq. (17) using the average values in Table 8 fits well to the experimental data in Figure 18. We concluded from this result and the limitations of the fracture mechanics models that failure in the static ILSS tests under dry conditions follows a flaw-insensitive, reduction in cross-sectional area criterion.

The control value of the ILSS is in a reasonable range from micromechanics modelling of composite (in plane) shear response based on the neat resin shear strength of about 60-70 MPa for 3502 epoxy[26], which is similar to 3501-6. Prediction of the composite shear strength from the matrix properties is complex, reflecting both the higher shear modulus due to the fibers, and also the locally high shear strains in the matrix depending on the local fiber arrangement. It is generally difficult to assign a strength property to a brittle polymer like neat 3501-6 epoxy independent of fracture mechanics, and evidence generally indicates that torsional failures initiate as brittle appearing cracks at inherent flaws or surface defects. Dry neat resin torsion stress-strain curves become somewhat nonlinear prior to failure, but do not show macroscopic yielding; wet resin is more nonlinear[26]. Increases in porosity reduce the shear modulus of the composite moderately [2,7,13] and factors including increased moisture content and temperature reduce the composite shear modulus in a predictable fashion through their effect on the neat matrix [26].

3.3 FATIGUE BEHAVIOR

This section presents the results of fatigue S-N tests on short beam shear specimens and Mode I and II fatigue crack growth. In each case the effects of porosity are investigated using only the three primary materials having 0.5, 2.8, and 8.7 percent nominal porosity levels. All tests are run under ambient conditions; the effects of moisture are considered in the next section. The relationship between the fatigue crack growth results and the short beam specimen S-N results is discussed at the end of this section.

3.3.1 Fatigue of Short Beam Shear Specimens

Short beam shear fatigue tests were conducted as described earlier with an R ratio (min/max force) of 10 (that is, the force applied only in compression, not reversed tension-compression which would provide a reversal in the shear direction). All tests were run to failure, which was defined as the cycles where a rapid increase in the displacement was observed (Fig. 4); this point coincided with the observation of macroscopic delamination cracks. As shown in Figure 19b, these cracks, when viewed in cross section, tended to pass through pores and zones of high porosity at ply and tow boundaries, with more cracks at higher porosity. The mode of failure, by interlaminar crack growth, was observed in all cases where cross sections were taken; no problems with shifts in failure mode were noted.

Fatigue studies were carried out primarily at 5 Hz; the only study of frequency effects was to compare the S-N data for the low porosity material with tests run at 2 Hz. As shown in Figure 20, no significant effect of frequency in the 2-5 Hz range was observed.

All of the S-N results are plotted as semi-log maximum cyclic shear stress vs. log cycles to faiure. The materials are then compared by three methods of normalizing, and are later compared with wet results. (As will be discussed later, the S-N data fit equally well to a straight line on a log-log

plot). Figure 21 compares the raw S-N fatigue data for the three primary materials. The trend lines are least-squares fits including the static strength results from ramp tests at 1 cycle. Table 7 gives the regression lines shown, as well as fits which did not include the static data; wet data, to be discussed later, are also included in Table 7. The points with arrows were specimens which did not fail, and were not included in the curve fits. The Appendix gives tabular results for all individual tests in this study.

The linear fits to the S-N data can be represented by

$$S_{max} = S_o - B \log N \tag{18}$$

for the raw data, where S_{max} is the maximum cyclic shear stress, S_o is the one-cycle intercept, B is the slope of the S-N curve in units of MPa/log cycles, and N is cycles to failure. For the normalized plots

$$S_{max}/S_o = 1\text{-}b \log N \tag{19}$$

where b, the slope of the normalized fatigue S-N plot, is the best measure of the fatigue sensitivity independent of static strength.

Figures 22-24 give normalized S-N curves. Figure 22 gives results where the trend lines in Fig. 21 are normalized by the average ILSS (S_o) in each case and do not necessarily pass through $S_{max}/S_o = 1.0$ at one cycle. In Figure 23, the trend lines fit through the raw fatigue data have been forced through S_o at one cycle and so the normalized curves all pass through $S/S_o = 1.0$. Fig. 24 ignores the static data entirely, as only the raw fatigue results are fit with a least-squares regression (Table 7, Part 5), and the curves and data are normalized by the one cycle intercepts shown. The intercepts differ only slightly from the measured static ILSS data, but there is a significant effect on the spacing of the normalized plots in Fig. 24.

The fatigue response of materials is best compared on normalized plots (Eq. 19), to eliminate effects of static strength differences. However, it is not necessarily true that the semi-log plots are

linear, with the fatigue process a simple extension of the static failure process, and so the appropriate static basis for normalizing the fatigue data is not obvious. In the present case there is little difference between the measured average S_o values and the one-cycle intercept extrapolated from the cyclic results. However, even the small differences in the normalizing parameters significantly affect any conclusions which can be drawn as to the effects of porosity on the fatigue resistance.

The normalized plots in Figures 22 and 23, and the slope of the plots, b, in Table 7, Parts 2 and 4, compare fatigue resistance when the measured static ILSS is included in the data set. These results show little difference between materials with 0.5 and 2.8 percent porosity, but moderately greater fatigue sensitivity at 8.7 percent porosity. However, Figure 24 and Table 7, Part 6 differentiate between the low and moderate porosity cases, and the three materials show progressively greater fatigue sensitivity as the porosity level increases. The correlation coefficients are highest when the static data are included (Table 7). (Limited early data by Greszczuk [2] for glass/epoxy showed no effect of porosity on the value b up to 4.6 percent porosity.)

The three normalizing procedures lead to two possible conclusions as to the effects of porosity. When the static data are included, the conclusion is that the fatigue sensitivity increases only above 2.8 percent porosity. When the static data are excluded, the conclusion is that higher porosity produces greater fatigue sensitivity over the whole porosity range, this in addition to the effects of porosity in reducing the static strength. It would take more data to reach any definitive answer to this question, and the trends may also vary with the test geometry and material configuration. Although the differences are not easy to define given the limited data and typical scatter, the apparent magnitude of the porosity effect is enough to be of importance. The b values from Fig. 24 produce a difference in lifetime for a stress level $S_{max}/S_o = 0.4$ of about 0.25 decades per 1% porosity, averaged over the entire porosity range. While the effect at low to moderate porosity would be negligible if static data are included in the normalization, it would be about 0.5 decades per 1 percent

porosity when static data are excluded. Extrapolation to lower S/S_o levels would produce greater differences (the normalized S-N curves are diverging as the stress decreases).

3.3.2 Mode I Fatigue Crack Growth

Interpretation of fatigue crack growth data in Mode I is complicated by the multiple cracking and fiber bridging effects described earlier, and only limited data was obtained comparing the high and low porosity cases. Crack growth generally progressed in a stable fashion, and no problems were encountered in the testing. All tests were run after extending the cracks statically to reach the plateau region in Fig. 11. Figure 25 gives typical crack growth data for the low porosity material plotted as log da/dN, the crack growth rate per cycle, against log G_{Imax}, the maximum value of G_I in the cycle; the R value was 0.1 in all cases, so there is little difference between a plot of G_{Imax} and G_I. The trend lines are least-squares fits to compare with the Paris Equation

$$da/dN = A_I \Delta G_I^m \tag{20}$$

or, as plotted here,

$$da/dN = A_I G_{Imax}^m \tag{21}$$

the results in Fig. 25 are very similar to those reported in Ref. 29 for dry, low porosity T300/5208. The data show no significant effect of frequency.

As noted earlier, the high porosity material has a much higher plateau G_{Ic} than does the low porosity material, and so fatigue crack growth tests necessarily extend to a higher G_{Imax} range. Figure 26 compares the low and high porosity data. At low crack growth rates, G_{Imax} values closely approach the respective static G_{Ic} values, while the data converge at growth rates approximately 10^{-5} mm/cycle. As shown in cross sections in Figure 27, the multiple cracking present in the high porosity material at high G_{Imax} was not observed at the low crack growth rates, where G_{Imax} was less than 30% of

G_{Ic}. It is not known whether the two materials would follow the same trend below where they converge, but these are extremely low rates where threshold behavior might be anticipated.

When the Mode I data in Fig. 26 are normalized by G_{Ic} in Fig. 28, the fatigue sensitivity of the high porosity material appears to be much greater than that at low porosity. However, this probably only represents a gradual transition from a multiple to a single crack front for the high porosity case. The absolute crack growth rate for the high porosity material never falls above that for the low porosity one at the same G_{Imax}. There was no evidence of a change in the low porosity case to reduce the very limited G_{Ic} fiber bridging effects at low G_{Imax}, but this was not studied in detail. The exponent, m, of 9.34 for the low porosity material is at the upper end of the range of values reported for various neat epoxies in Ref. 32.

3.3.3 Mode II Fatigue Crack Growth

It was indicated earlier that considerable difficulty was encountered with the Mode II fatigue crack growth tests with ENF specimens. Figure 29 shows the result of growing a crack at a constant G_{IImax} level for a distance of up to 20 mm from the initial crack position which was produced by the arrest from a static G_{IIc} test. The crack growth rate consistently decreased by several orders of magnitude, and then stopped altogether. The data were produced by growing the crack for a few mm, shifting the crack tip position to remain within the desired zone (Fig. 14), and growing further. Extensive study of this behavior established that the local crack front region was normal in appearance with no fiber bridging or multiple cracking which could explain the effect. However, through fractography and X-ray study, we found the problem was in the uneven growth of the crack front across the specimen width (crack length is normally measured at the surface). The crack on the interior tended to lag behind that on the edges, producing a deceleration of the edge-measured crack. We determined that the first few mm of crack extension were reliably straight, and so the crack growth data were obtained by growing the crack for increments of less than 2 mm, followed by a static test to reestablish a new crack front, etc.

Data produced in 2-mm increments from a fresh crack front were consistent and reproducible. Figure 30 shows typical results which follow the Paris relationship

$$da/dN = A_{II} G_{IImax}^{m} \tag{22}$$

These results are insensitive to laminate thickness (Fig. 30) or frequency (Fig. 31) and agree closely with results from Ref. 9. (Tests in Ref. 9 used a cantilever beam specimen which did not appear to have the problems with crack front straightness encountered here.)

Figures 32 and 33 and Table 7 compare the Mode II fatigue crack growth data for the three primary porosity levels. The data are all very similar regardless of porosity level, starting near G_{IIc} at low crack rates (Fig. 32), and decelerating with decreasing G_{IImax} following about a 5th-6th power

trend. While the three data sets overlap at both high and low rates in Fig. 33, there is a slight decrease in the exponent, m, from 5.72 to 5.61 to 5.25 as the porosity increases from 0.5 to 2.8 to 8.7 percent.

3.3.4 Discussion

The relative effects of porosity on the (dry) short beam shear S-N curve and the Modes I and II fatigue crack growth resistance follow a similar pattern to that of the static properties. The short beam shear fatigue sensitivity is increased moderately by porosity, the Mode I fatigue crack resistance is complicated by the effects of multiple cracking at high porosity, and the Mode II fatigue crack resistance is insensistive to porosity level. Again, a major concern is to rationalize the ILSS fatigue data in terms of the porosity effects and whether they can be related to the Mode II fatigue crack growth resistance.

It was concluded in the preceding section that the static ILSS data were probably flaw-insensitive, reflecting only the reduction in cross-sectional area due to the pores. We must now explore whether in fatigue, cracks emanate from the pores and grow to cause failure, and whether the lifetime is then dominated by fracture mechanics parameters including the inherent flaw size and fatigue crack growth law. If the lifetime of the short beam specimen is dominated by the process of crack growth from the larger pores, then the S-N curve trend should be predictable by integrating the crack growth Eq.(22) from the initial to the critical crack size at the applied stress level. Eq.(22) in terms of K_{II} rather than G_{II} is given by

$$da/dN = A'_{II}K_{IImax}^{2m} \tag{23}$$

Assuming a constant cyclic load range, and a crack which remains sufficiently small so that Eq.(5) is unchanged during growth except for the increase in crack length, a, the cycles to failure will be (following Ref. 32)

$$N = [1/a_o^{(m-1)} - 1/a_c^{(m-1)}]/[(m-1)A_{II}(1.25)^{2m}S_{max}^{2m}] \tag{24}$$

where a_o is the inherent (embedded circular) flaw length and a_c is the critical flaw length for unstable crack growth at the static G_{IIc}.

The results in Fig. 32 are fit at the low to moderate porosity levels by the material constants $m = 5.7$ and $A_{II} = 3.37 \times 10^{-18}$, giving $A_{II} = 69.4 \times 10^{-12}$ through Eq.(6), if da/dN is in units of m/cy, and K_{II} is $MPam^{1/2}$, and G_{II} is in J/m^2. For all values of a_o investigated, the term involving a_c is negligibly small. This leaves a simplified relationship for the typical geometry and materials constants in this study as

$$N = 24.2 \times 10^8 \, S_{max}^{-2m} \, a_o^{1-m} \tag{25}$$

and, for $m = 5.7$

$$N = 24.2 \times 10^8 \, S^{-11.4} \, a_o^{-4.7} \tag{26}$$

Since the value of the constant is not well established for the flaw geometries of practical concern, this can be generalized assuming only the measured exponent, m, to

$$N = C_3 \, S^{-2m} \, a_o^{1-m} \tag{27}$$

which can be fit to the S-N data at one point when the appropriate value of m is used. The value of a_o can be taken from the flaw distribution data in Table 4.

Eq. (27) predicts a power law short beam fatigue S-N curve which would be linear on a log-log plot, unlike the semi-log representations which have been used thus far. There is a clear prediction of the slope of the S-N curve (-2m) and the strong sensitivity to the initial flaw size. The fatigue crack growth trend, m, and the S-N curve trend have been shown to correlate for a number of neat and reinforced thermoplastics in the opening mode [34,35]. When the S-N data from Fig. 21 are replotted on a log-log basis in Figure 34, they conform almost as well to a linear relationship (Table 7, Part 7). However, the exponents of the best linear fits are much greater than the expected $2m = 11.4$ from Eq. (27). Thus, Eq.(27) does not accurately predict the experimental data. If the constant is evaluated as in Eq.(26) rather than curve fit, the predicted curves are in even poorer agreement. The only parameter that is predicted at all well is the spacing of the S-N curves, which derives from the differences in a_o. If the average flaw dimensions from Table 4 are inserted into

Eq.(26) with a constant value of Smax, there is predicted to be a 3.68 decade longer life for the 0.5 percent porosity case than for the 8.7 percent case, with the 2.8 percent case falling in between. These are not greatly different from the actual data in Fig. 34.

Another possibility is that some of the pores grow, not to a critical length, but enough to further reduce the shear strength. Table 9 compares the predicted extension of circular embedded pores of radius a (half of the maximum value of L in Table 4) at the shear stress level where the three S-N curves in Fig. 21 reach 10^5 cycles. The value of G_{II} for each pore length and stress level is calculated from Eqs.(5) and (6), and the rate of crack extension is determined from extrapolations of the trend lines in Fig. 32, with the rate multiplied by 10^5 to determine the amount of crack extension after 10^5 cycles. The results in Table 9 indicate negligible crack growth from pores prior to specimen failure at all porosities with the values of L in Table 4. Calculations for even larger pores are also shown at the bottom of Table 9 for 2.8 and 8.7 percent porosity materials. For the high porosity material, the larger pore size of 1.0 mm radius would show extension of about 7 percent in 10^5 cycles (dry). This pore size is over four times as long as the longest measured pores, but pores of this general size can be found on typical fracture surfaces, Fig. 8e. The equivalently larger pore for 2.8 percent porosity of 0.25 mm still shows negligible growth. It should also be noted that all but the 1-mm pore G_{II} values fall below the measured da/dN range and the extrapolated da/dN values used in the calculations may fall well below any fatigue crack growth threshold. Thus, it is concluded that only exceptionally large, fairly circular pores might show significant fatigue crack growth in the typical fatigue lifetime of a short beam specimen; more elliptically shaped pores of the same (major axis) length would have a lower G_{II} at their tips as discussed earlier. It is very unlikely that pore growth would be significant in the low and medium porosity cases, but it could be at high porosity.

If the S-N data for low porosity cases are not dominated by fatigue crack growth, then there must be another explanation for the behavior. In fact, neat resin torsional fatigue S-N data are

available for 3501-6 epoxy in Ref. 36. If the data in Ref. 36, are fit excluding the static strength at one cycle, the value of b is 0.082. (In Ref. 36 the data are fit with a bilinear relationship, but a single line appears equally valid.) Thus, the (dry) neat resin torsional fatigue shows a value of b which is very close to those for the ILSS tests in this study, and it is concluded that the short beam results at low to moderate porosity levels simply reflect the resin fatigue resistance. The tensile and torsional fatigue of the neat resin are reported to be similar in Ref. 36, with failure by brittle crack normal to the maximum tensile stress direction. Both Ref. 36 and a recent tensile study with a similar resin at MIT[37] conclude that the neat resin fails when a crack nucleates from a flaw, with no significant stable crack growth. The neat resin S-N data in tension do not correlate with Mode I fatigue crack growth trends[36], but show a higher apparent m value than predicted by the crack growth data, much the same as with the Mode II ILSS data using Eq. (26) in Fig. 34. Fatigue S-N data for neat epoxy specimens appear to be dominated by the process of crack nucleation from flaws, not stable fatigue crack growth. It appears reasonable to draw the same conclusions for the short beam fatigue S-N data at low and moderate porosity levels, so that the fatigue lifetime is determined primarily by the cycles to nucleate cracks from many pores relatively late in the specimen lifetime. The cracks then coalesce and reduce the cross-sectional area to cause failure.

A relevant study of flaws by Hojo and Hayashi[38] used artificial through-width flaws in unidirectional graphite/epoxy short beam specimens under fatigue loading. They found that flaws larger than about 1 mm long would propagate to cause specimen failure under fatigue loading, while smaller flaws would not directly cause failure. Their fracture mechanics based model predicted the specimen lifetime only for flaws above the critical 1 mm size. A through-crack of 1 mm total length would have a stress intensity factor at its tip equivalent to an embedded circular crack of about 1.3 mm diameter or an elliptical crack with an aspect ratio of 4 having total major axis length of 2 mm,

assuming isotropic material with the thickness much greater than the crack length. Thus, the findings in Ref. 38 are generally consistent with those in this study.

Finally, the increased fatigue sensitivity of the high porosity material must be explained. Assuming that the ILSS failure is flaw-insensitive, then there must be a further reduction in cross-sectional area due to fatigue in the 8.7 percent porosity material to explain its steeper normalized S-N curve as compared with the 0.5 percent porosity case. From the ratio of static ILSS data, the cross-sectional area of the failure plane of the high porosity case is 65.5 percent of that of the 0.5 percent porosity case. The slopes of the normalized S-N curves, b, are 0.075 and 0.090 for the low and high porosity cases, respectively. Taking the value S at 10^5 cycles, 42.5 MPa for the high porosity case, this value would need to be increased to 47 MPa to achieve a b value of .075 . This implies that, if no pore growth is expected in the low porosity material, the high porosity material increase in b can be explained by a further reduction in cross-sectional area during fatigue, prior to failure. By this reasoning, the original cross section of the high porosity case was 34.5 percent pore at the most severe potential failure path, and this was increased to 40.8 percent by crack growth and coalesence from pores during fatigue. (Complications due to the timing of pore growth during the fatigue process have been ignored, with the assumption that most of it occurs early in the lifetime.)

No direct evidence of pore growth has been found in unfailed fatigue specimens, and fatigue fracture surfaces appear much like static areas (Fig. 8e). However, it seems very likely that the required modest increase in area reduction may occur for the following reasons:

1. At high porosity, many of the boundary regions contain closely packed cracks in matrix rich regions (Fig. 8) which could readily coalesce. The stress intensity between closely spaced pores is higher than that given by Eq.(5)[27]. Furthermore, at the lower fatigue stress levels, the matrix may become more sensitive to stress concentrations at pores, since it is not as close to the shear yielding condition.

2. Any coalescence of pores in the boundary region could then produce a flaw large enough to propagate significantly as a fatigue crack (Table 9), and some such pores may already exist, as noted on the fracture surfaces (Fig. 8e).

3. Even though smaller pores may not propagate as fully developed fatigue cracks, some extension due to the maximum tensile stress within the local matrix region may occur, although a fully developed Mode II (hackled) failure process may not be possible. The conditions for nucleation of cracks from pores may be possible even if the G_{II} value is too low for continued propagation.

Thus, it is concluded that the most likely explanation of the reduced b value at high porosity is that some expansion of the pore/crack area occurs fairly early in the lifetime as a result of fatigue. Conditions necessary for the macroscopic fatigue crack propagation of an initially flawed area to produce specimen failure do not appear to exist. The failure is expected to be dominated by the fatigue of the matrix over the reduced cross-sectional area. As with the neat resin, fatigue lifetime is probably dominated by the conditions for nucleation of resin cracks, not by the propagation characteristics.

In this view, it would be expected that the increasing cross-sectional area reductions would be more prominent at higher cycles. The data in Fig. 21 tend to support this: if the 8.7 percent porosity data for cycles less than 1,000 are fit separately (including the static data), the b value is decreased to 0.81, close to the low porosity cases. However, there are insufficient data to firmly conclude from this, and the low cycle data frequently fall above the fit line in other cases as well.

3.4 MOISTURE EFFECTS

This section compares wet and dry static and fatigue data of high and low porosity materials. The dry condition is ambient laboratory air, while the wet condition is water saturated; all tests were run at room temperature. The moisture content data and wet test procedures have been described in earlier sections. Extensions of the dry failure mechanisms discussed earlier to the wet condition are described in the discussion at the end of this section.

3.4.1 Short Beam Shear Properties

Table 10 gives the static ILSS values for wet vs. dry conditions. Both the high and low porosity materials show a lower strength when wet; the reduction in strength is 18 percent at low porosity and 23% at high porosity. As noted earlier (Table 5), the high porosity material absorbs more moisture, and the average moisture content in the resin is probably higher. As Table 10 indicates, even after conditioning in 95° water, the loss in ILSS is reversible if the specimens are redried prior to testing. Some nonreversible strength loss with high porosity material was reported in Ref. 7 and 40, but this was not observed here. The loss in wet strength appears to derive entirely from the reversible effect of water on the matrix. Wet (saturated) vs. dry torsion tests on neat 3502 epoxy resin specimens were reported to show a 17% strength loss for the wet material[26], nearly the same as that found here. Thus, there appear to be no significant effects from factors such as fiber/matrix interface failure (to be discussed more later) or osmotic pore pressure[6] in these tests.

Figures 35-40 present the wet vs. dry S-N fatigue data for the 0.5 and 8.7 percent porosity material. In each case the data are plotted directly and also normalized by the static strength (normalized curves are forced through $S/S_0 = 1.0$). The low porosity material in Figs. 35 and 36 shows overlapping normalized data wet and dry, with a slightly lower slope, b, for the wet (regression parameters are given on Table 7). Thus, we can conclude that a saturation moisture content in the

resin and testing in liquid water have no significant effect on the fatigue resistance beyond the drop in static strength when the porosity level is very low and the pores are small.

Figures 37 and 38 indicate that the high porosity material with larger pores shows a slightly greater relative static strength loss (Table 10) and a moderate increase in fatigue sensitivity, (b), due to water (Figure 38, Table 7, Part 4).

Figures 39 and 40 compare the wet results for the two porosity levels. In Figure 39, the combined effects of high porosity on both static and fatigue properties result in much lower maximum stresses to cause failure at high cycles for the high porosity material under wet conditions. At 10^6 cycles, the failure stress of the high porosity material is reduced to about 42 percent of that at low porosity. The normalized data in Figure 40 show significantly greater fatigue sensitivity for the high porosity material. The reason for the greater water sensitivity in fatigue at high porosity will be discussed later.

3.4.2 Mode I Crack Growth

The wet Mode I static G_{Ic} values in Table 10 show a significant increase in plateau value as compared with the dry data. The low porosity material increases from 258 dry to 569 J/m^2 wet, while the corresponding high porosity material increase is from 471 to 663 J/m^2. These wet increases are associated with a greater amount of bridging fibers across the crack tip as shown in Figure 41. Thus, the origin of the water effect is analogous to the effect of higher porosity producing multiple cracking and increasing G_{Ic}, but here the wet environment produces more interfacial failure and fiber bridging which increases the crack growth resistance. When the saturated Mode I low porosity specimens are redried, the value of G_{Ic} returns to 330 J/m^2, close to the initial control level. Results reported for AS1/3501-6 were similar to those observed here, showing increase in wet vs. dry G_{Ic}, with much greater fiber bridging in the wet case[41,42]. Other studies have shown either moderate increases in G_{Ic} due to water [8], or else no effect[9]. The high porosity material, which already has extensive multiple cracking when dry, shows less increase in G_{Ic} due to wet conditions.

Figures 42-47 compare wet and dry Mode I fatigue crack growth data for low and high porosity materials. The wet vs. dry data for the low porosity case are much like Fig. 26, which compared high and low porosity cases under dry conditions. When the value of G_{Ic} is increased by increasing the extent of fiber bridging or multiple cracking, the fatigue crack growth exponent, m, drops. The crack growth data at low G_{Imax} values then tend to converge on the control case with a lower static G_{Ic} but a higher m. This is apparently due to the reduction in multiple cracking or fiber bridging when the G_{Imax} value is reduced. When the data are normalized by the respective G_{Ic} (Figure 43), the higher G_{Ic} material is much more fatigue sensitive, but this condition may not persist at very low G_{Imax}.

There are no adequate data in the very low G_{Imax} range to judge whether the wet trend in Fig. 42 (or the high Vp trend in Fig. 26) would actually become identical to that of the control case, but this would be expected if the extent of multiple cracking and fiber bridging became equal to the control. As noted earlier, the reason that the extent of multiple cracking and fiber bridging are reduced at low G_{Imax} values is hypothesized to be the reduced region of sufficiently high crack-tip stress levels away from the immediate crack plane, which does not allow other fibers to be brought into the crack tip process zone.

Figures 44 and 45 compare wet and dry data for the high porosity material. Differences in G_{Ic} are less significant here, and the normalized data (Fig. 45) show little effect of water on the fatigue crack growth resistance. Comparisons between the high and low porosity materials under wet conditions in Figures 46 and 47 similarly show little difference, reflecting the similarly high G_{Ic} values. In general, any material or conditions with a high G_{Ic}, 500 J/m^2 or more, show a lower crack growth exponent, m in Eq. (21), of 5 to 7, while the control dry material with low porosity and little fiber bridging, with G_{Ic} = 258 J/m^2, shows a much greater exponent of 9.4. This increase in fatigue sensitivity with an increase in G_{Ic} is analogous to that in neat polymers, where m is typically about 2 for tough thermoplastics having a yield zone which is sensitive to fatigue, while a much higher exponent is observed with thermoset polymers like brittle epoxies, which have little identifiable yielding at the crack tip[32].

3.4.3 Mode II Crack Growth

The static G_{IIc} data (Table 10) show a decrease of about 18-20 percent for both porosity levels when the materials are saturated and tested in water, relative to dry materials tested dry. Testing in 100 percent relative humidity has about the same effect as testing in water, but testing in water with initially dry material reduces the decrease in G_{IIc} as compared with that for presaturated material. The drop in G_{IIc} due to water is almost identical to the drop in ILSS in Table 9, and is presumed to have the same origin. The data cited earlier for the effect of water on neat 3502 epoxy [22] shows a nearly identical drop in shear strength, with little change in strain at failure. Both the neat resin strength and the product of the ultimate strength and strain, a good measure of resin toughness, drop about 15-20 percent due to water saturation at room temperature. Thus, the neat resin shear stress-strain properties appear to be a direct indication of composite ILSS and G_{IIc} insofar as moisture effects are concerned.

The Mode II fatigue crack data are given in Figures 48-54. The low porosity material shows a slight reduction in crack growth resistance, but the normalized data in Figure 49 overlap at both low and high da/dN levels. The high porosity material shows a more significant drop in exponent, m, from 5.25 to 4.20 when wet (Figs. 50 and 51). Comparison of the wet behavior for the high and low porosity materials shows a marginally better normalized performance at low porosity (Fig. 52). The latter comparison is very similar to that under dry conditions in Fig. 33. Figure 54 compares data for the high porosity material initially saturated, tested in liquid water vs. 100 percent relative humidity air, and initially dry material tested in liquid water; the differences between the three cases are insignificant. Thus, neither the presence of liquid water nor the moisture content away from the immediate crack tip region (to the depth which can diffuse in the several hours it requires to run the test) appear critical in determining the effect of water on the Mode II fatigue crack growth data.

3.4.4 Discussion

Comparison of wet and dry results at different porosity levels supports the interpretation of the short beam shear data developed in previous sections. In particular, the low porosity material with smaller pores continues to respond in a manner consistent with a flaw-insensitive model, with moisture effects deriving directly from the sensitivity of the neat resin shear strength to moisture content. The high porosity material shows a slightly greater response to water saturation than does the neat resin strength, and this will be considered in the context developed in the last section of some limited crack growth in fatigue, but not to the extent of producing failure directly by fatigue crack growth.

Figure 36 indicates that there is no effect of moisture on the normalized S-N fatigue life of low porosity material; the only effect is in the initial strength. For the high porosity material (Fig. 38), there is an increase in the normalized S-N curve slope, b, from 0.090 (dry) to 0.10 (wet), given in Table 7, Part 2. It was argued in the case of dry S-N data that the high porosity material must have some crack growth and coalescence from pores which reduces the cross-sectional area beyond that in the static condition. The crack growth may either be in Mode II if the pores lengthen, or Mode III if they increase in width, as discussed earlier. Assuming that the growth is by Mode II fatigue crack extension, then the effect of moisture should be present in both the short beam shear and Mode II fatigue crack growth data. The Mode II fatigue crack growth will occur at much lower values of G_{IImax} under wet conditions, due both to the lower G_{IIc} and lower m value when wet (Figure 50).

Table 9 gives predicted pore growth data for wet and dry conditions. The amount of pore growth (expansion of pore length by crack growth) predicted for the largest pore at 10^5 cycles and the actual short beam stress level from the S-N curve at 10^5 cycles is 15%, about twice that for the dry case at its corresponding shear stress level. Had the S-N curve for the wet material had the same normalized slope as for the dry case (b = 0.090, Table 7, Part 2), then there would have been about

four times more pore growth. Thus, the reduced wet Mode II fatigue crack growth curve in Fig. 50 leads to the prediction that the short beam shear S-N curve will be steeper for the wet condition despite the lower maximum shear stress values expected due to the lower static strength. The moderate increase in b for the normalized S-N curve when wet is qualitatively predicted if it is assumed that failure is flaw-insensitive but that a significant reduction in cross-sectional area occurs as result of localized flaw growth following the measured Mode II fatigue crack growth curve. The low porosity material has pores which are too small to grow significantly under this influence, and the normalized wet and dry S-N curves are nearly indentical (Fig. 36).

The increased Mode I fiber bridging and the decreased G_{IIc} under wet conditions also suggest a possible decrease in fiber/matrix bonding due to water. This question was briefly investigated by directly measuring the in situ bond strength with the microbonding test described in Ref. 42. Data for wet and dry materials given in Table 10 show no significant effect on the force to debond fibers of similar diameter. The wet case was not immersed during testing, but an effort was made to maintain dampness on the polished cross section where the test is run by compressively loading the ends of individual fibers. The microdebonding test effectively measures bond strength, as opposed to bond fracture toughness. It is possible that water reduces the resistance to interfacial debond crack growth, but this was not investigated.

SECTION IV

CONCLUSIONS

We can draw a number of conclusions on the effects of porosity on the dry and wet delamination resistance of AS4/3501-6 graphite/epoxy. Although the pore distributions appear typical of this class of materials, and the results tend to agree with those of other studies, the conclusions apply directly only to this widely used material system with unidirectional fibers. We should also recognize that the results from the short beam shear test may not represent those from other shear tests.

Interlaminar Shear Strength. Pores reduce the static ILSS approximately in proportion to the reduction in cross-sectional area on the weakest (fracture) plane, thus following a flaw-insensitive criterion. The largest pores observed at 8.7 percent porosity are not of adequate size to produce a fracture mechanics dominated static behavior based on measured G_{IIc} values. Moisture saturation reversibly reduces the static room temperature ILSS by about 20 percent, approximately the amount reported for the neat resin. Short beam shear fatigue S-N results show greater fatigue sensitivity at high porosity, with the effect at moderate (2.8 percent) porosity subject to interpretation. The low to moderate porosity fatigue sensitivity is approximately that reported for the neat resin, and does not appear to involve significant effects of fatigue crack growth from the pores prior to failure, based on fracture mechanics calculations and Mode II fatigue crack growth data. At high porosity, some crack growth from pores relatively early in the lifetime may be important, but not to the extent of producing failure based on growth of a macroscopic crack; instead, failure appears still to be based on a reduction in area, but with part of that reduction from fatigue crack growth in addition to the

original pore area. The fatigue trends are similar under wet conditions, with slightly more apparent crack growth at high porosity as a result of the reduced resistance to Mode II fatigue crack growth.

Mode I Delamination. Due to the effects of fiber bridging, Mode I static and fatigue crack growth results are taken in the plateau region, after at least 15 to 20 mm of crack extension. The static G_{Ic} value is increased significantly as the porosity increases, up to about 12 percent porosity. The increased G_c is caused by multiple cracking generated in regions of high porosity, so that multiple crack growth fronts are formed. Wet conditions further increase G_{Ic}, due primarily to increased fiber bridging; this is particularly significant at low porosity levels. The high static G_{Ic} levels under wet conditions and at high porosity do not produce comparably high fatigue crack growth resistance. A lower crack growth exponent for the higher G_{Ic} cases results in a convergence of the Mode I fatigue crack growth data to a similar range for low crack propagation rates in the range of 10^{-5} to 10^{-6} mm/cycle. As the cyclic G_{Imax} level is reduced, the extent of multiple cracking for high porosity material and fiber bridging for the wet material are reduced, so that the crack fronts appear similar to the dry control case at low growth rates where the data converge.

Mode II Delamination. The static Mode II G_{IIc} values were insensitive to the porosity level up to 12 percent porosity. G_{IIc} decreased by about 20 percent under wet conditions for both high and low porosity materials. The dry fatigue crack growth results (normalized by G_{IIc}) showed very little effect of porosity level, while the wet results showed slightly reduced fatigue crack growth resistance at high porosity.

Pore Size Effects. The results of this study indicate that the reduction in fatigue resistance caused by porosity may depend more strongly on pore size and shape than on the average porosity content. If pores are 0.5 mm or less in maximum dimensions and are well dispersed, then the

reduction of interlaminar strength is due only to the reduction in cross-sectional area, and moisture only reduces the strength to the extent that it reduces neat resin strength. If the pores become as large as a 1-mm radius crack, then significant fatigue crack extension may occur in the short beam specimens. The crack growth may simply cause a further reduction in cross-sectional area, as is apparent in this study; however, a larger delamination could also grow to sufficient size to produce a truly fracture mechanics dominated macroscopic crack failure. The size of the pore which produces signifcant effects will vary with ply configuration and local stress state, but the 1- to 2-mm size range appears critical, depending on pore shape.

REFERENCES

1. Kardos, J.L., Dudokovic, M.P. and Dave, R. "Void Growth and Resin Transport During Processing of Thermosetting Matrix Composites," Advances in Polymer Science, 80 (1986) p. 101.

2. Greszczuk, L.B., "Effect of Voids on Strength Properties of Filamentary Composites," Proc. 22th Conf., SPI Reinforced Plastics Div., Society of the Plastics Industry, New York (1967) Section 20-A.

3. Hand, W., "Quality Control of Filament Wound Materials For Deep Submergence Vessels," Proc. 20th Conf., SPI Reinforced Plastics Div., Society of the Plastics Industry, New York (1965) Section 1-E.

4. Fried, N., "Response of Orthogonal Filament Wound Materials to Compressive Stress," Proc. 20th Conf., SPI Reinforced Plastics Div., New York (1965) Section 1-C.

5. Judd, N.C.W. and Wright, W.W., "Voids and their Effects on the Mechanical Properties of Composites - An Appraisal," SAMPE J. 14 (1978) p. 10.

6. Ashbee, K.H.G. and Wyatt, R.C., "Water Damage in Glass Fibre/Resin Composites," Proc. Roy. Soc. A312 (1969) p. 349.

7. Hancox, N.L., "The Influence of Voids on the Hydrothermal Response of Carbon Fiber Reinforced Plastics," J. of Materials Science, 16 (1981) p. 627.

8. Russell, A.J. and Street, K.N., "Moisture and Temperature Effects on Mixed-Mode Delamination of Unidirectional Graphite-Epoxy Composites", Delamination and Debonding Materials, ASTM STP 876, Philadelphia (1985) p. 349.

9. Russell, A.J. and Street, K.N., "The Effect of Matrix Toughness on Delamination: Static and Fatigue Fracture under Mode II Shear Loading of Graphite Fiber Composites," Toughened Composites, ASTM STP 937, N.J. Johnston, Ed., ASTM, Philadelphia (1987) p. 275.

10. Yoshida, H., Ogasa, T., and Hayashi, R., "Statistical Approach to the Relationship between ILSS and Void Content of CFRP, " Composites Sci. and Tech, 25 (1986) p.3.

11. Olster, E.F., "Effects of Voids on Graphite Fiber Reinforced Composites," AD-746560, U.S. Naval Air Systems Command, Washington, D.C., July, 1971.

12. Brand, R.A., Brown, G.G., and McKague, E.L., "Processing Science of Epoxy Resin Composites," AFWAL-TR-83-4124, Air Force Wright Aeronautical Laboratories, January 1984.

13. Harper, B.D., Staab, G.H., and Cohen, R.S., "A Note on the Effects of Voids upon the Hygrol and Mechanical Properties of AS4/3502 Graphite/Epoxy," J. of Composite Materials 21 (1987) p. 280.

14. Bohlmann, R.E., Renieri, G.D., and Kozarewiscz, J.J., "Development of Acceptance Criteria for Graphite/Epoxy Structures," McDonnell Douglas Report A7361, 1981.

15. Thomas, R.D. and Cable, C.W., "Quality Assessment of Glass Reinforced Plastic Ship Hulls in Naval Applications," Ocean Engr. and M.S. Thesis, Dept. of Materials Sci. and Engr., MIT (1985).

16. Stone, D.E.W. and Clarke, B., "Ultrasonic Attenuation as a Measurement of Void Content in Carbon-Fiber Reinforced Composites," Nondestructive Testing 8 (1975) p. 137.

17. Hancox, N.L., "The Effects of Flaws and Voids on the Shear Properties of CFRP," J. Materials Science, 16 (1981) p. 285.

18. Hercules, Inc., Product Literature for ASA/3501-6.

19. Sidey, G.R. and Bradshaw, I.J., "Some Investigations of Carbon-Fiber-Reinforced Plastics under Impact Loading," Proceedings of International Conference on Carbon Fibers, Their Composites and Applications, The Plastics Institute, London (1971).

20. Johnson, W.S. and Mangalgiri, P.D., "Investigation of Fiber Bridging in Double Cantilever Beam Specimens," J. Composites Technology and Research, 9 (1987) p. 10.

21. de Charentenay, F.X., Harry, J.M., Prel, Y.J. and Benzeggagh, M.L., "Characterizing the Effect of Delamination Defect by Mode I Delamination Test," Effects of Defects in Composite Materials, ASTM STP 836, ASTM, Phildelphia (1984) p. 84.

22. Bradley, W.L. and Cohen, R.N., "Matrix Deformation and Fracture in Graphite-Reinforced Epoxies," Delamination and Debonding of Materials, ASTM STP 876, W.S. Johnson, Ed., ASTM, Philadelphia (1985) p. 389.

23. Hibbs, M.F., TSE, M.K., and Bradley, W.L., "Interlaminar Fracture Toughness and Real-Time Fracture Mechanism of Some Toughened Graphite/Epoxy Composites'" Toughened Composites, ASTM STP 937, N.J. Johnston, Ed., ASTM, Philadelphia, (1987) p. 115.

24. Trethewey, B.R., Carlsson, L.A., Gillespie, J.W., and Pipes, R.B., "Mode II Interlaminar Fracture During Static and Fatigue Loading," CCM Report 86-26, U. of Delaware (1986).

25. Russell, A.J. and Street, K.N., "Factors Affecting the Interlaminar Fracture Energy of Graphite/Epoxy Laminates," Proceedings, Fourth International Conference on Composite Materials, Japan Society for Composite Materials (1982) p. 279.

26. Zimmerman, R.S., Adams, D.F., and Walrath, D.E., "Investigation of the Relations Between Neat Resin and Advanced Composite Mechanical Properties," NASA CR-172303, NASA-Langley Research Ctr., Hampton, VA (May, 1983).

27. Tada, H., Paris, P.C., and Irwin, G.R., The Stress Analysis of Cracks Handbook, Del Research Corp., Hellertown, PA (1973) pp. 24.7-26.3.

28. Cinar, A. and Erdogan, F., "The Crack and Wedging Problem for an Orthotropic Strip," Inter. J. Fracture, 23 (1983) p. 83.

29. Ramkumar, R.L. and Whitcomb, J.D., "Characterization of Mode I and Mixed-Mode Delamination Growth in T300/5208 Graphite Epoxy," Delamination and Debonding of Materials, ASTM STP 876, W.S. Johnson, Ed., ASTM, Philadelphia (1985) p. 315.

30. Paris, P.C. and Sih, G.C., "Stress Analysis of Cracks," Fracture Toughness Testing and Its Applications, ASTM ASTP 381, ASTM, Philadelphia (1965) p. 60.

31. Corten, H.T., "Micromechanics and Fracture Behavior of Composites," Modern Composite Materials, L.J. Broutman and R.H. Krock, Eds., Addison-Wesly Pub., Reading, MA (1967) Ch. 2.

32. Hertzberg, R.W. and Manson, J.A., Fatigue of Engineering Plastics, Academic Press, New York (1980) p. 123.

33. Hertzberg, R.W., Deformation and Fracture Mechanics of Engineering Materials, Wiley, New York (1976) p. 473.

34. Mandell, J.F., McGarry, F.J., and Li, C.G., "Fatigue Crack Growth and Lifetime Trends in Injection Molded Reinforced Thermoplastics," in High Modulus Fiber Composites in Ground Transportation and High Volume Applications, ASTM STP 873, D.W. Wilson, Ed., ASTM, Philadelphia (1985) p. 36.

35. Mandell, J.F., "Fatigue Behavior of Short Fiber Composites," in The Fatigue of Composite Materials, K.L. Reifsnider, Ed., Elsevier Scientific (to be published).

36. Odom, E.M. and Adams, D.F., "A Study of Polymer Matrix Fatigue Properties," NADC Report 83053-60 (1983).

37. Acton, A., "The Fatigue of Graphite Fiber-Reinforced Thermoplastic and Thermoset Matrices," Ph.D. Thesis, Dept. of Materials Science and Engineering, MIT (1986).

38. Hojo, M. and Hayashi, R., "Effects of Interlaminar Defects on the Shear Strength of CFRP Laminates," Trans. Japan Soc. Comp. Mat. 10 (1984) p. 50.

39. Kaeble, D.H., Dynes, P.J., Crane, L.W., and Maus, L., "Interfacial Mechanisms of Moisture Degradation in Graphic-Epoxy Composites," J. Adhesion 7 (1974) p.25.

40. Johnson, W.S. and Mangalgiri, P.D., "Influence of the Resin on Interlaminar Mixed-Mode Fracture," Toughened Composites, ASTM STP 937, N.J. Johnston, Ed., ASTM, Philadelphia (1987) p. 245.

41. Law, G.E. and Wilkins, D.J., "Delamination Failure Criteria for Composite Structures," NAV-GD-0053, Naval Air Systems Command, Washington, D.C. (May, 1984).

42. Mandell, J.F., Grande, D.H., Tsiang, T.-H., and McGarry, F.J., "Modified Microdebonding Test for Direct In-Situ Fiber/Matrix Bond Strength Determination in Fiber Composites," in Composite Materials: Testing and Design (Seventh Conf.) ASTM STP 893, J.M. Whitney, Ed., ASTM, Philadelphia (1986) p. 87.

Table 1 Organic Foaming Agents

CHEMICAL	TRADE NAME	SUPPLY COMPANY	CHEMICAL COMPOSITION	DECOMPOSITION TEMPERATURE (°C)	DECOMPOSED GAS	DECOMPOSITION PRODUCTS
A. Sulfonyl Hydrazides						
P-toluene sulfonyl	Celogen TSH	Uniroyal	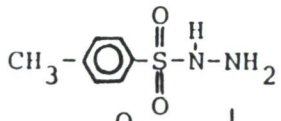	110-120	N_2, H_2O	
P,P'-oxybis (benzen sulfonyl hydrazides)	Celogen OT	Uniroyal	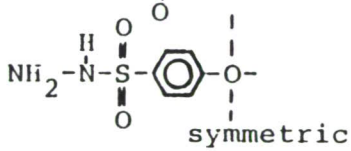 symmetric	158-160	N_2, H_2O	Nonpolar aromatic sulfur containing polymer (84 wt/o)
B. Azo-Compounds						
Azodicarbonamide	Kempore 200	Olin	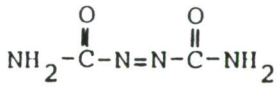	190 (in air) 150 (with activator)	N_2, CO, CO_2	Hydrazobisformamide, cyanuric acid, and urazol (68 wt/o)
Azo tetramide derivatives	Nitropore ATA	Olin		120-140 (with activator)	N_2	
1,1'-Azobis	Vazo 88	DuPont	symmetric 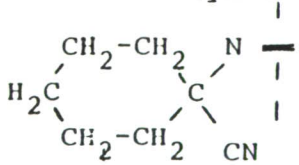	100	N_2	Hydrogen cyanide (HCN) and tetramethylsuccinonitrile (TMSN)
2,2'-Azobis	Polyzole AZDN or AZDN	Olin	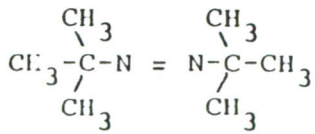	103	N_2	HCN and TMSN

TABLE 2

TREATMENT USED TO INTRODUCE POROSITY AND RESULTING POROSITY CONTENT

LAMINATE I.D.	TREATMENT USED	AVERAGE POROSITY CONTENT*
8 Press Control	None	5.4
8 V	AZDN between plies 4 and 5	11.5
8G	Vazo 88 between plies 4 and 5	10
Primary Materials		
12AC	None (Autoclave)	0.5 $\pm$ 0.09
12P	Without vacuum (Press)	2.8 $\pm$ 0.25
12W	Water spray between each ply and 1/4 of regular pressure (Press)	8.7 $\pm$ 0.66
12 Press Control	None	2.4
12 V	AZDN between plies 6 and 7[a]	8.2
12 A	Nitropore ATA and activator between plies 6 and 7[b]	23.3[d]
12 B	Nitropore ATA between plies 6 and 7[b]	8.0
12 C	Kampore 200 and activator between plies 6 and 7[a]	29.0[d]
12 D	Kampore 200 between plies 6 and 7[a]	8.1
12 E	Celogen TSH between plies 6 and 7[a]	8.7[d]
12 F	Celogen OT between plies 6 and 7[a]	9.6
12-369V	AZDN between plies 3 and 4, 6 and 7 and 9 and 10[a]	11.0
12 T1	Acetone spray on plies 3,6,9[a]	3.4
12 T2	Water soaking plies 6 and 7 for 1 day[c]	6.8
12 T3	Water soaking plies 6,7,8 for 1 day[c]	11.6
12 T4	Xylene spray on plies 3,6,9[a]	8.0
12 T5	Water spray on plies 3,6,9[a]	10.4
24 AC	None (Autoclave)	0.5 $\pm$ 0.11
24 Press Control	None	2.4
24 V	AZDN between plies 12 and 13[a]	5.0[e]

* Averages were obtained from at least 2 locations, by quantitative microscopy.

a The amount of blowing agent or liquid spray used was about 0.1 gram per 194 cm^2.

b The amount of blowing agent with actiator used was about 1 gram.

c The water uptake was about 5 grams per ply.

d A layer of residual blowing agent left between plies 6 and 7 in the cured laminate.

e Non-uniform distribution of porosity.

TABLE 3

INTERLAMINAR SHEAR STRENGTH VS. POROSITY CONTENT

NO. OF PLIES	LAMINATE	THICKNESS* (CM)	SPAN LENGTH (CM)	ILSS* (MPA)	AVE. POROSITY CONTENT** (VOL %)
24	24 PRESS CONTROL	0.296	1.34	82.5±4.6	2.4
	24 V	0.296	1.47	64.4±1.4	5.0
	24 AC	0.298	1.50	107.5±5.9	0.5±0.11
	12 AC	0.150	0.76	115.1±4.7	0.5±0.09
12	12 P	0.151	0.76	92 ±3.1	2.8±0.25
	12 AC	0.152	0.76	75.4±3.7	8.7±0.66
	12 PRESS CONTROL	0.148	0.76	84.9±2.8	2.4
	12 V	0.155	0.76	66.4±0.6	8.2
12	12-369V	0.146	0.76	63.3±1.8	11.0
	12 A	0.158	0.76	37.5±3.5°	23.3
	12 CC	0.201	1.02	27.1±12.1°	29.0
	12 T2	0.140	0.76	67.4±2.1	6.8
	12 T3	0.140	0.76	57.2±5.2	11.6
	8 PRESS CONTROL	0.105	0.53	67.0±4.8	5.4
8	8 V	0.104	0.53	54.2±0.7	11.5
	8 G	0.105	0.53	54.7±1.6	10.1

* Averages were obtained from 3 specimens
** Averages were obtained from at least 2 regions
° Compressed Failure Mode, ILSS not valid

Table 4

Pore Dimensions for Laminates of Three Nominal Porosity Contents.*

Pore Dimension	Laminate I.D.	12AC (V = 0.5%) p	12P (V = 2.8%) p	12W (V = 8.7%) p	12AC (V = 0.5%) p
B (μm)	Maximum	25	50	76.5	12.5
	Average	11.0	14.0	26.3	8.8
	Std. Dev.	5.5	10.3	17.8	3.7
D (μm)	Maximum	18.8	31.3	39.1	13.8
	Average	8.0	11.0	12.8	8.6
	Std. Dev.	3.7	6.6	7.0	2.7
L (μm)	Maximum	26.3	113.8	458.8	22.5
	Average	14.8	51.9	89.8	13.0
	Std. Dev.	6.1	40.5	120.4	4.5

* Detailed Data in Appendix.

Table 5

5(a) Equilibrium Weight Change for Saturated and Vacuum Oven Dried Laminates

Laminate	Porosity Content (%)	Oven Dried % Wt. Loss	Saturated State % Wt. Gain	Total % Change (Saturated - Oven Dried)
12AC	0.5	-0.25	+1.5	+1.8
12P	2.8	-0.20	+2.5	+2.1
12W	8.7	-0.18	+3.3	+3.5

* Dried in a vacuum oven at 100°C for 17 days.
** Conditioned at 75°C in deionized wateer for one month, and then left in deionized water for at least another 45 days (see Appendix data).

Table 5 (Cont.)

5(b) Liquid Water Content of Pores at Saturation

(1) From Weight Gain

Assumed densities: Fiber 1.8 g/cm^3 ; Matrix 1.265 g/cm^3 .

Nominal V_p (%)	Weight Gain (%)	V_m (%)	Assumed Matrix wt. Gain (%)	% Pore Volume Filled with Liquid Water
0.5	1.8	30.5	5.9	0*
2.8	2.1	28.2	5.9	44.6
8.7	3.5	24.3	5.9	39.5

* Assumed in order to calculate matrix weight gain.

(2) From Differential Scanning Calorimetry Melt Peak (Data in Appendix).

Nominal V_p (%)	No. tests	Volume % Liquid Water in Specimen	% Pore Volume Filled with Liquid Water
0.5	2	0.025	5
2.8	2	0.295	10
8.7	3	1.810	20
8.7	2	1.88*	22

* Interior 50% of material only; edges and surfaces sanded away.

Table 6

MODE I AND II STATIC INTERLAMINAR FRACTURE ENERGY

LAMINATE I.D.	V_p (%)	INITIAL G_{Ic}* [J/m^2]	PLATEAU G_{Ic}** [J/m^2]	NATURAL CRACK G_{IIc}° [J/m^2]
24 AUTOCLAVE CONTROL	0.5	227	270	439
24 PRESS CONTROL	2.4	159	294	440
24 V	5.0	345	429	450
12 AC	0.5±0.09	214	265	420
12 P	2.8±0.25	222	291	458
12 W	8.7±0.66	381	471	365
12 PRESS CONTROL	2.4	207	285	445
12 V	8.2	252	364	384
12-369V	11.0	247	390	436
12 A	23.3	14.6	17.8	129
12 C	29	68	58.8	92
12 T1	3.4			387
12 T2	6.8			411
12 T3	11.6			434
12 T4	8.0			428
12 T5	10.4			414
8 PRESS CONTROL	5.4	173	187	452
8 V	11.5	238	315	418
8 G	10	219	238	

* Averages were obtained from 2 tests
** Averages were obtained from 7 tests
° Averages were obtained from 3 tests

Table 7

Regression Parameters for Fatigue S-N and Crack Growth Data.

1. Best Fit S-N Curve Including Static ILSS Values

Test Cond.	Laminate I.D.	V_p(%)	Intercept (MPa)	Slope B	Corr. Coeff.(r)
DRY	12AC	0.5	116	8.8	0.971
	12P	2.8	92	7.1	0.980
	12W	8.7	76	6.7	0.990
WET	12AC	0.5	95	6.2	0.951
	12W	8.7	59	5.8	0.984

2. S-N Curve Normalized by the Average Static ILSS

Test Cond.	Laminate I.D.	V_p(%)	Intercept (MPa)	Slope b
DRY	12AC	0.5	0.99	0.075
	12P	2.8	1.01	0.078
	12W	8.7	1.01	0.090
WET	12AC	0.5	1.01	0.066
	12W	8.7	1.10	0.100

3. S-N Curve Forced Through the Average Static ILSS

Test Cond.	Laminate I.D.	V_p(%)	Intercept (MPa)	Slope B	Corr. Coeff.(r)
DRY	12AC	0.5	117.7	9.0	0.988
	12P	2.8	92.2	7.1	0.989
	12W	8.7	75.3	6.6	0.993
WET	12AC	0.5	93.5	5.9	0.978
	12W	8.7	56.9	5.9	0.989

Table 7 (Cont.)

4. S-N Curve Normalized by the Average Static ILSS, Forced Through S/So = 1.0 at 1 Cycle

Test Cond.	Laminate I.D.	V_p (%)	Intercept (MPa)	Slope b
DRY	12AC	0.5	1.0	0.077
	12P	2.8	1.0	0.074
	12W	8.7	1.0	0.090
WET	12AC	0.5	1.0	0.064
	12W	8.7	1.0	0.097

5. Best Fit S-N Curve of Fatigue Data w/o Static ILSS Values

Test Cond.	Laminate I.D.	V_p (%)	Intercept (MPa)	Slope B	Corr. Coeff. (r)
DRY	12AC	0.5	113	7.9	0.913
	12P	2.8	94	7.5	0.950
	12W	8.7	78	7.1	0.986
WET	12AC	0.5	100	7.4	0.906
	12W	8.7	62	6.5	0.975

6. S-N Curve w/o Static ILSS Value Normalized by Intercept

Test Cond.	Laminate I.D.	V_p (%)	Intercept (MPa)	Slope b
DRY	12AC	0.5	1.0	0.070
	12P	2.8	1.0	0.081
	12W	8.7	1.0	0.091
WET	12AC	0.5	1.0	0.074
	12W	8.7	1.0	0.102

Table 7 (Cont.)

7. Best Fit Log-Log S-N Curve Including Static ILSS Values

Test Cond.	Laminate I.D.	V (%) p	Intercept (Log MPa)	Slope	Corr. Coeff.(r)
DRY	12AC	0.5	2.07	0.0416	0.963
	12P	2.8	1.97	0.0416	0.962
	12W	8.7	1.89	0.0526	0.985

8. Mode I Delamination

Specimen I.D.	V p	Dry Slope m	Dry A I	Wet Slope m	Wet A I
12AC	0.5%	9.4	1.58×10^{-25}	6.6	1.0×10^{-20}
12W	8.7%	5.0	1.26×10^{-15}	5.5	3.16×10^{-18}

9. Mode II Delamination

Specimen I.D.	V p	Dry Slope m	Dry A II	Wet Slope m	Wet A II
12AC	0.5%	5.7	1.78×10^{-17}	5.0	6.31×10^{-15}
12P	2.7%	5.7	1.0×10^{-17}		
12W	8.7%	5.2	3.98×10^{-16}	4.2	1.10×10^{-12}

Table 8. Reduction in Cross-Sectional Area Along Potential Fracture Paths in Short Beam Specimens

V_p (%)	Reduction in Area (%)* Individual	Average	Predicted ILSS (MPa)
0.5	1.7, 3.3, 1.7	2.2	115
2.8	27.2, 28.7, 25.3	27.1	86
8.7	54.2, 42.7, 43.3 42.7	45.7	64

* $(W_p/W_T)(W_o/W_T)$ in Eq. 17.

Table 9

Predicted Crack Growth from Pores in Short Beam Shear Fatigue

Nominal V_p(%)	Condition	a_{max} (mm)	S at 10^5Cycles (MPa)	G_{II} (J/m^2)	Increase in a after 10^5 Cycles (%)
(Measured Pore Max. L(-2a), Table 4:)					
0.5	dry	0.0132	73.5	2.3	$2x10^{-6}$
	wet	0.0132	63.0	1.7	$1x10^{-4}$
2.8	dry	0.0569	56.0	5.9	$4x10^{-4}$
8.7	dry	0.229	42.5	13.7	0.03
	wet	0.229	30.4	7.0	0.25
(For Pores 4.4 Times Longer Than Measured Max. L :)					
2.8	dry	0.250	56.0	25.9	0.026
8.7	dry	1.0	42.5	59.6	16.0
	wet	1.0	30.4	30.5	20.0

Table 10

Wet vs. Dry Static Properties and Fiber/Matrix Bond Strength

Wet (Saturated) vs. Dry (Ambient) Interlaminar Properties at 20°C

V_p (%)	Condition	ILSS (MPa)	G_{Ic} (J/m^2)	G_{IIc} (J/m^2)
0.5	Dry	115.4±4.7	258	420
	Wet	93.7±5.5	569	337
2.8	Dry	93.0±3.3	291	458
	Wet	78.1±2.7	-	-
	Wet (Severe Cond.)	77.9±5.3	-	-
	Redried from Severe Cond.	89.9±4.0	-	-
8.7	Dry	75.4±3.7	471	365
	Wet	58.0±2.2	663	297

* 30 days in 95°C deionized water.
** 30 days vacuum oven dried, 55°C.

Compressive Force to Debond Fibers of Average Diameter

Conditioning	Debonding Force (gm)
Dry (Ambient) Control	2.86 ± 0.44
75°C Water, 1 Week	2.80 ± 0.23
95°C Water, 1 Month	2.60 ± 0.16

* Tested at 20°C, damp surface.

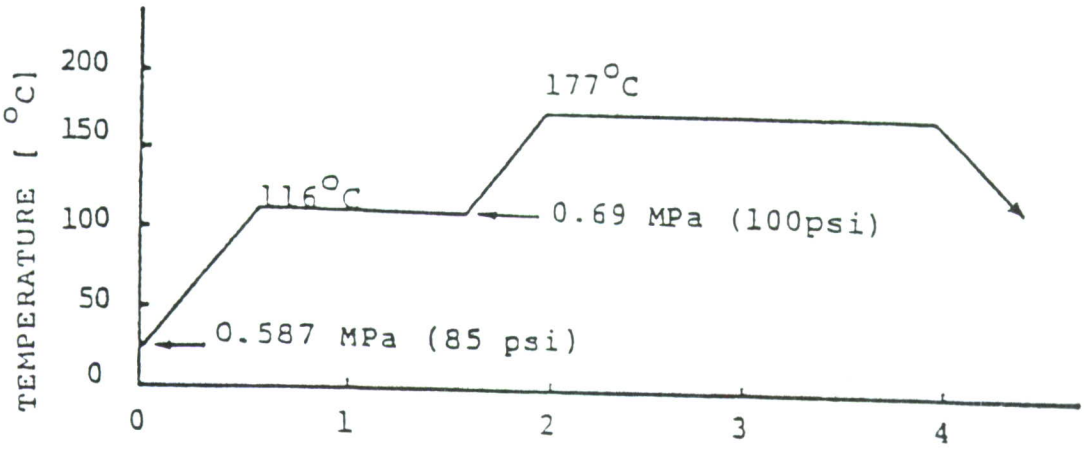

For Autoclave or Hot Press Molding

1. Place vascuum-bagged layup in hotpress or autoclave.
2. Vent the vacuum bag to atmosphere pressure. (for autoclave, apply minimum vacuum of 625 mm of Hg)
3. Apply pressure of 0.587 MPa (85 psi).
4. At a rate of 2.5° C/min. raise the laminate temperature to 116°C. Hold for 1 hour.
5. Raise pressure to 0.691 MPa (100 psi), for autoclave, vent the vacuum bag to atmosphere pressure.
6. Raise temperature at a rate of 2.5°C/min. to 177°C. Hold for 2 hours.
7. At the rate of 3°C/min., lower laminate temperature to 92°C. Release the pressure.
8. Remove layup and unbag.

Figure 1. Curing Cycle

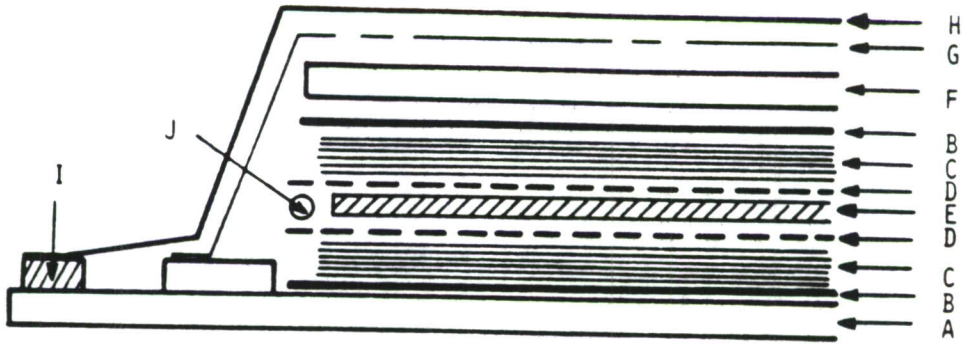

A	BOTTOM PLATE
B	IMPERMEABLE TEFLON SHEET
C	PAPER BLEEDER
D	PERMEABLE TEFLON SHEET
E	PREPREG LAYUP (LAMINATE)
F	TOP PLATE
G	AIR BREATHER
H	VACUUM BAGGING (HS-6262 Blue Nylon Bagging)
I	VACUUM TAPE
J	THERMOCOUPLE

Figure 2. Vacuum Bag Arrangement.

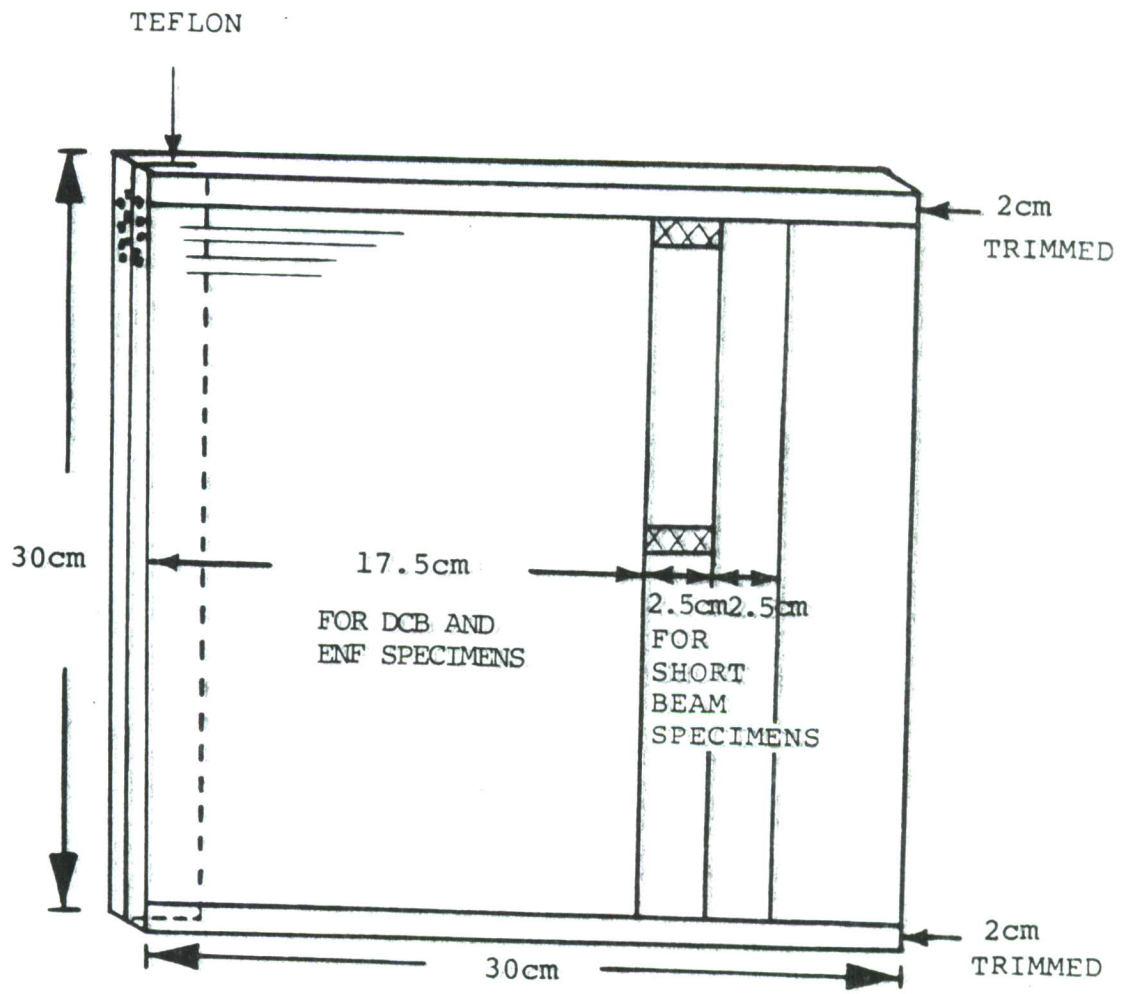

Figure 3. Specimen Layout.

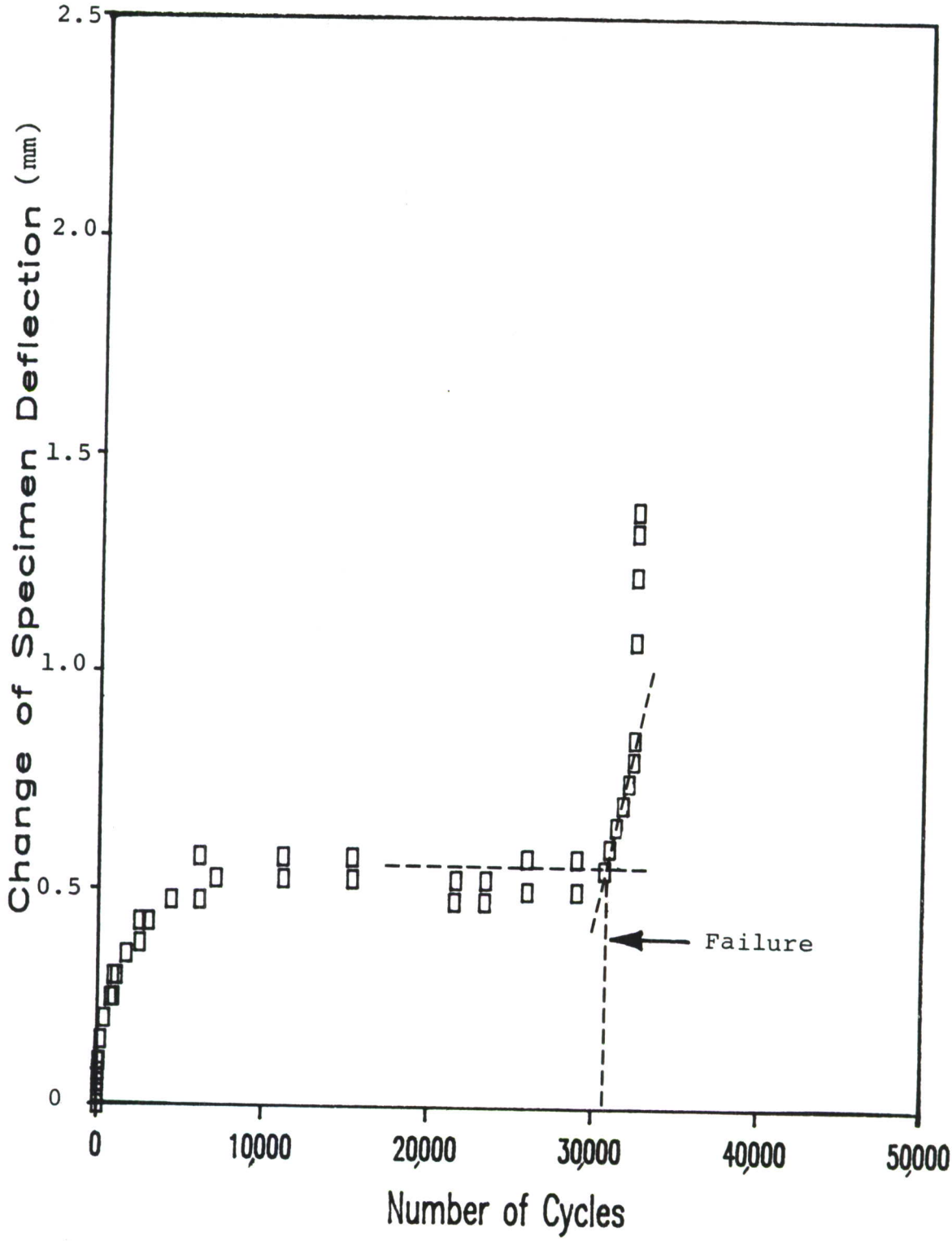

Figure 4. Typical Change in Deflection vs. Number of Fatigue Cycles for Short Beam Specimen; Definition of Failure.

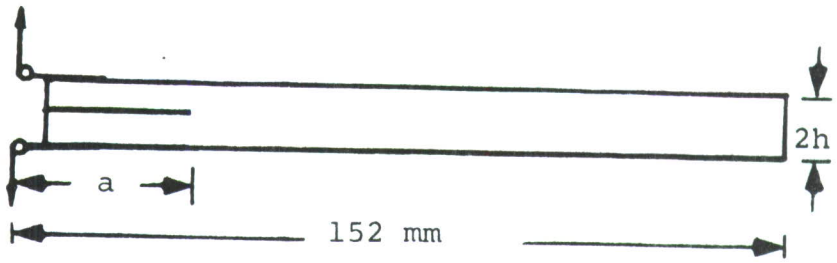

(Width: W= 20 mm)

Figure 5. Mode I Double Cantilever Beam (DCB) Specimen.

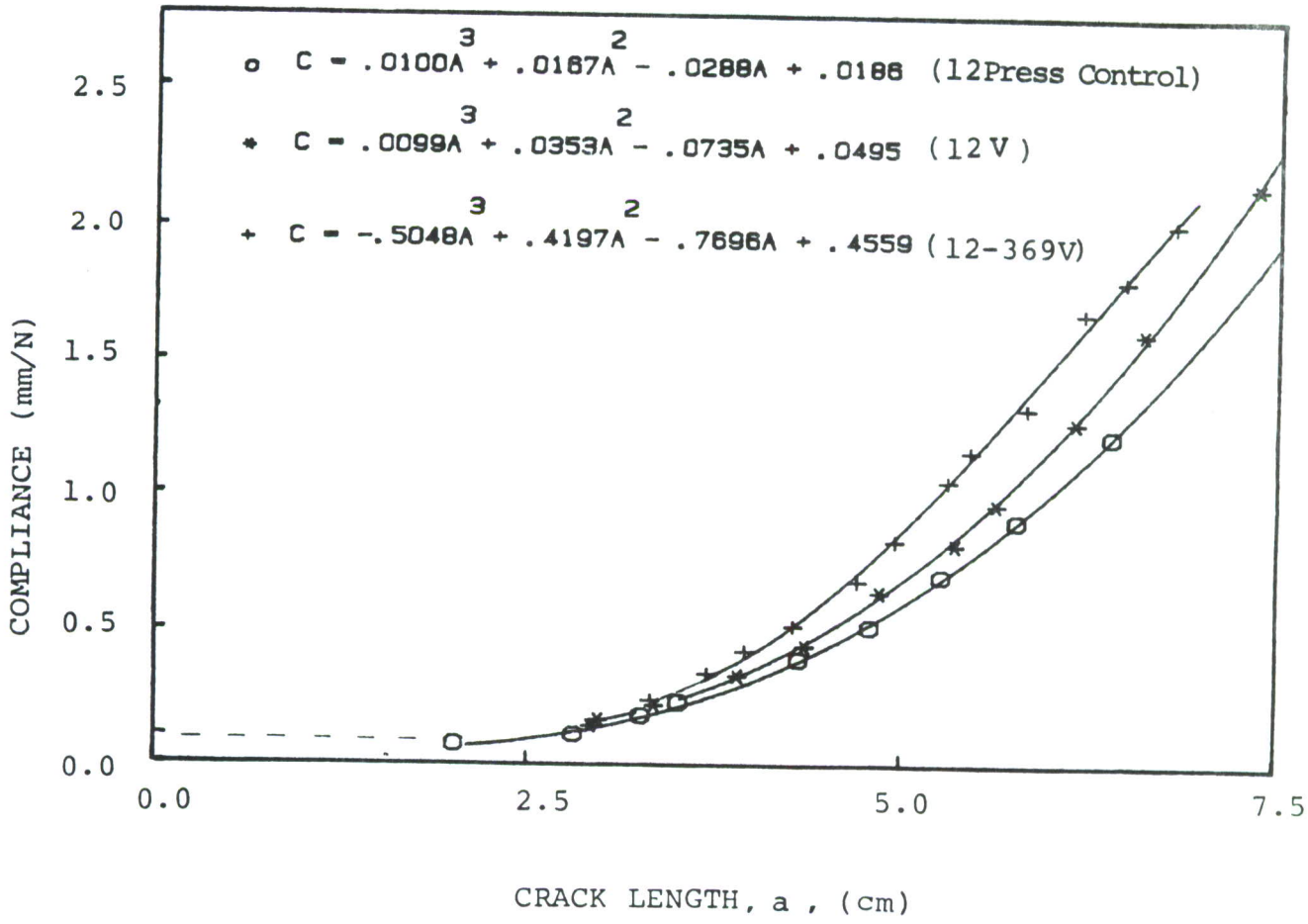

Figure 6. Experimental Compliance Curves for 12-ply DCB Specimens.

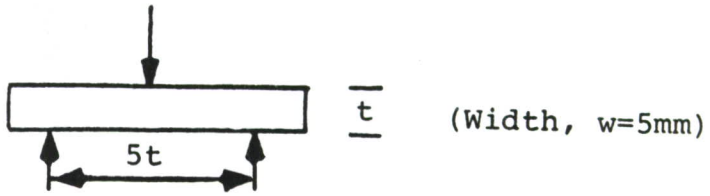

Short Beam Shear

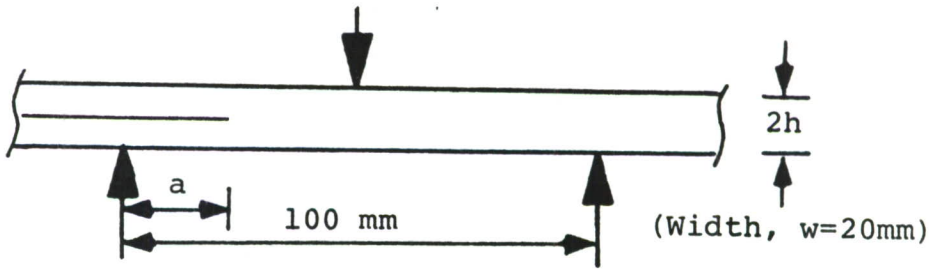

End Notched Flexure

Figure 7. Short Beam Shear and Mode II End Notched Flexure Specimens.

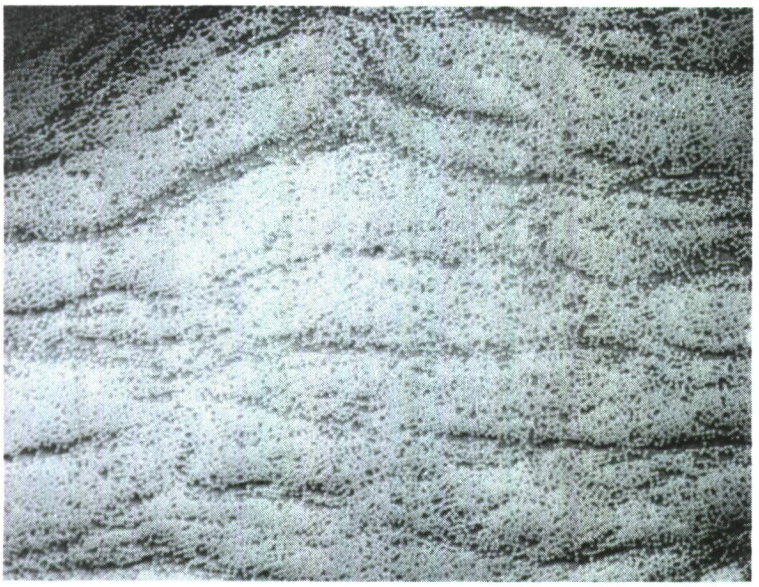

(x80)

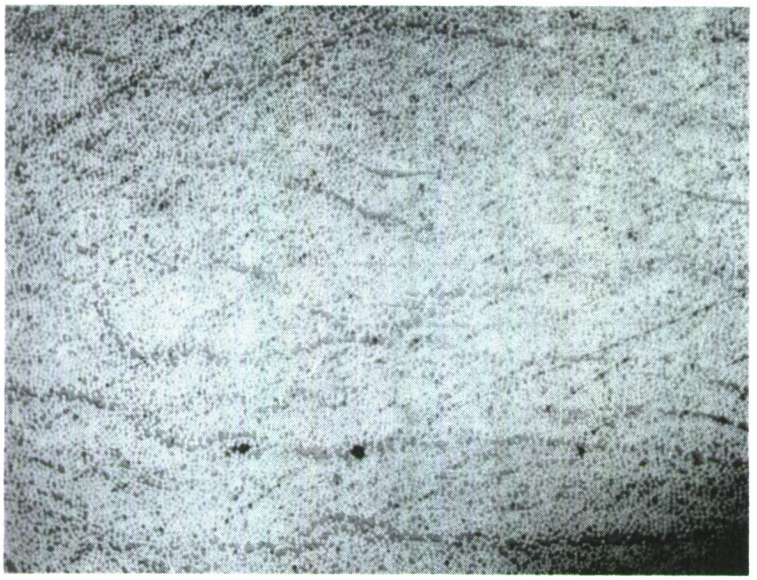

(x80)

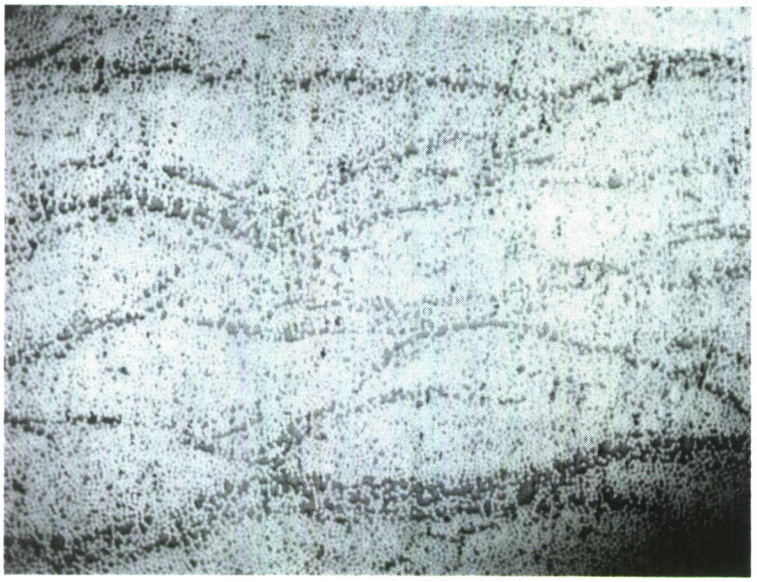

(x80)

Figure 8. (a) Micrographs of Transverse Sections from Material 12AC (V_p=.5%);

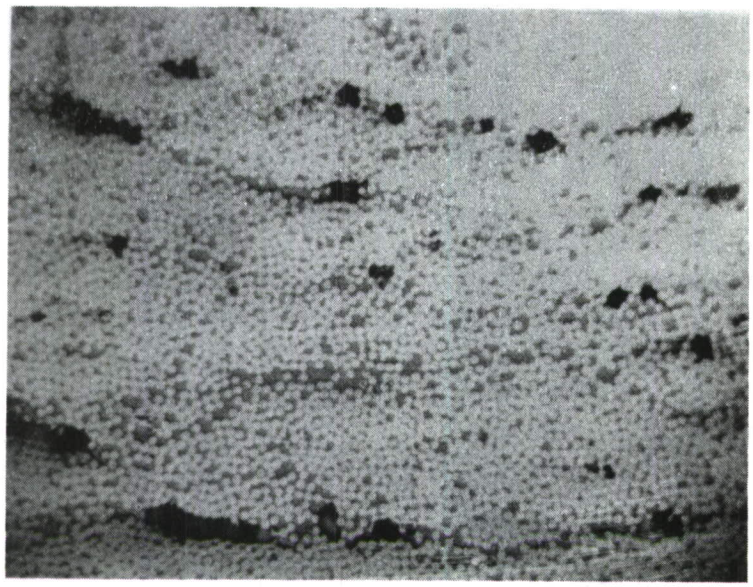

(x160)

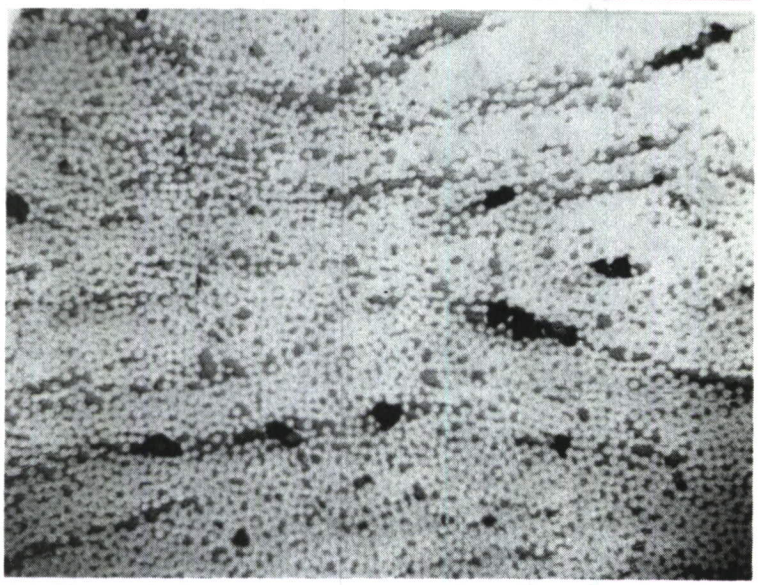

(x160)

(x80)

Figure 8. (b) Micrographs of Transverse Sections from Material 12P (V_p=2.8%);

(X125)

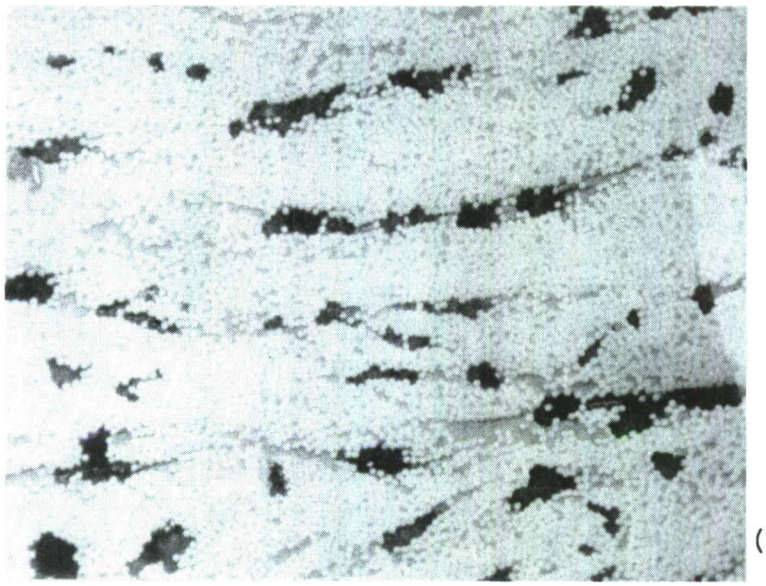

(X125)

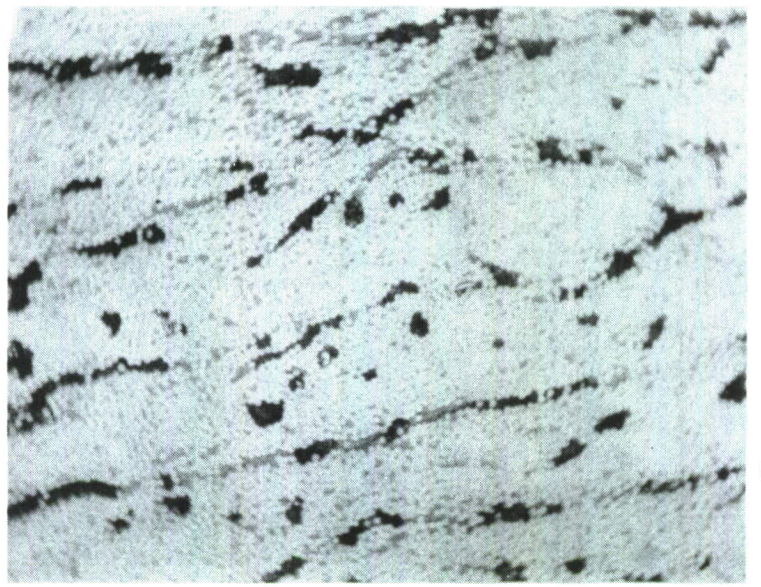

(x125)

Figure 8. (c) Micrographs of Transverse Sections from Material 12W (V_p=8.7%);

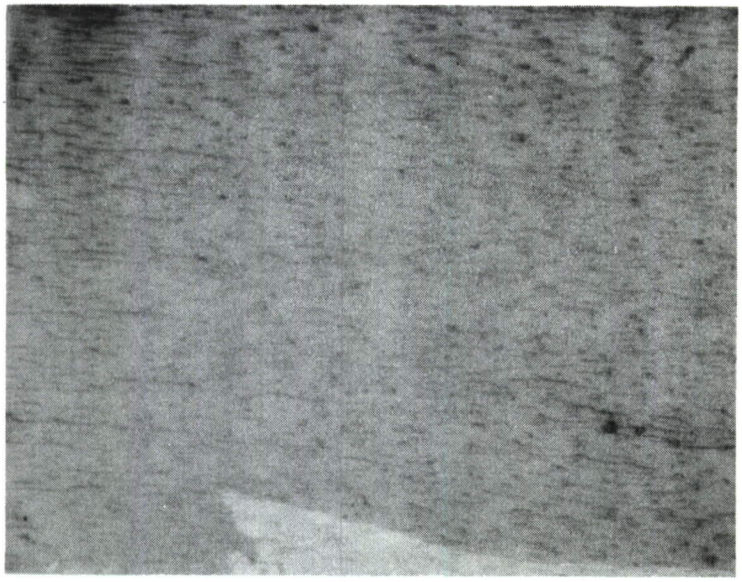

MATERIAL 12AC (V_p=0.5%)

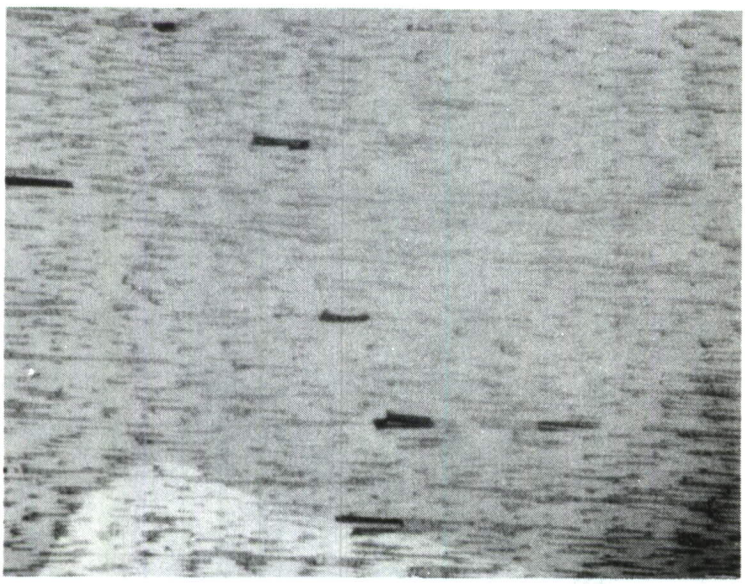

MATERIAL 12P (V_p=2.8%)

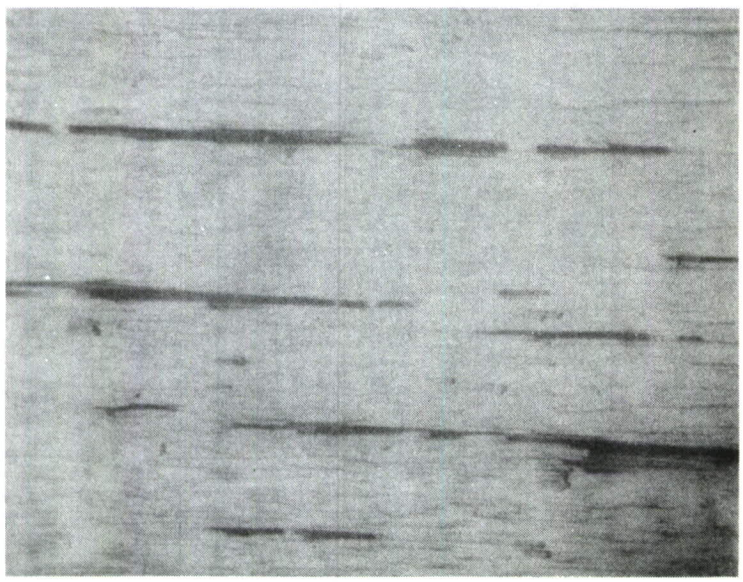

MATERIAL 12W (V_p=8.7%)

Figure 8. (d) Micrographs of Longitudinal Sections from the Three Materials; (x80)

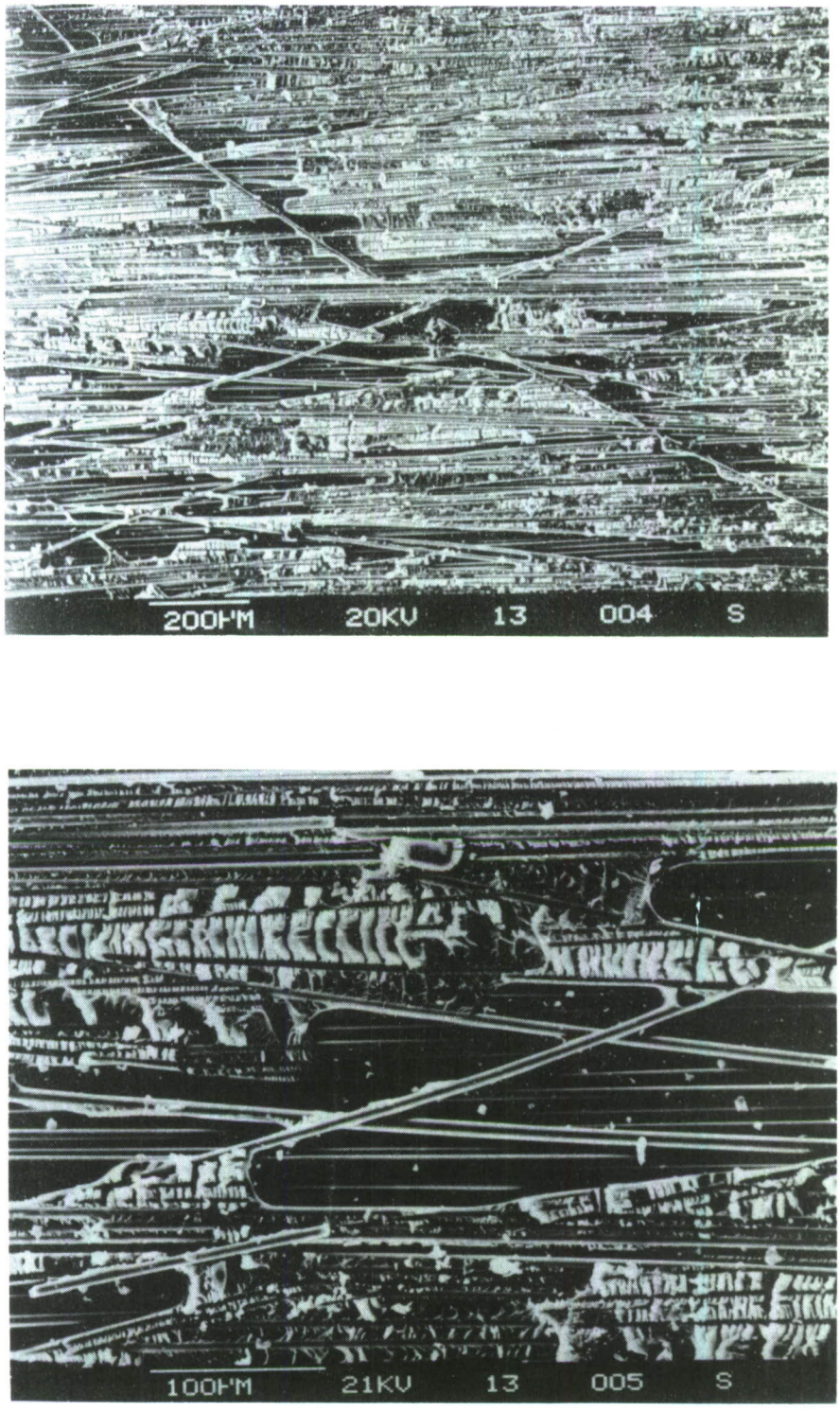

Figure 8. (e) Short Beam Fracture Surfaces from Material 12W Showing Large Interconnected Pore at Misoriented Fibers at Two Magnifications.

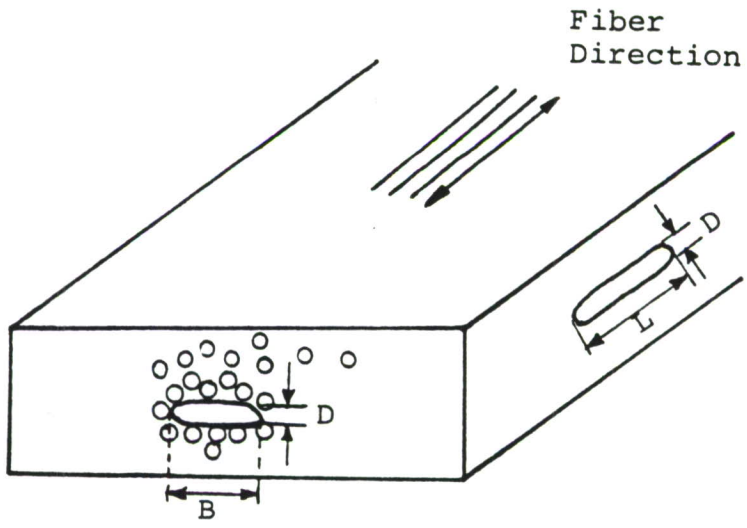

(a) Schematic

Figure 9 Pore Dimensions

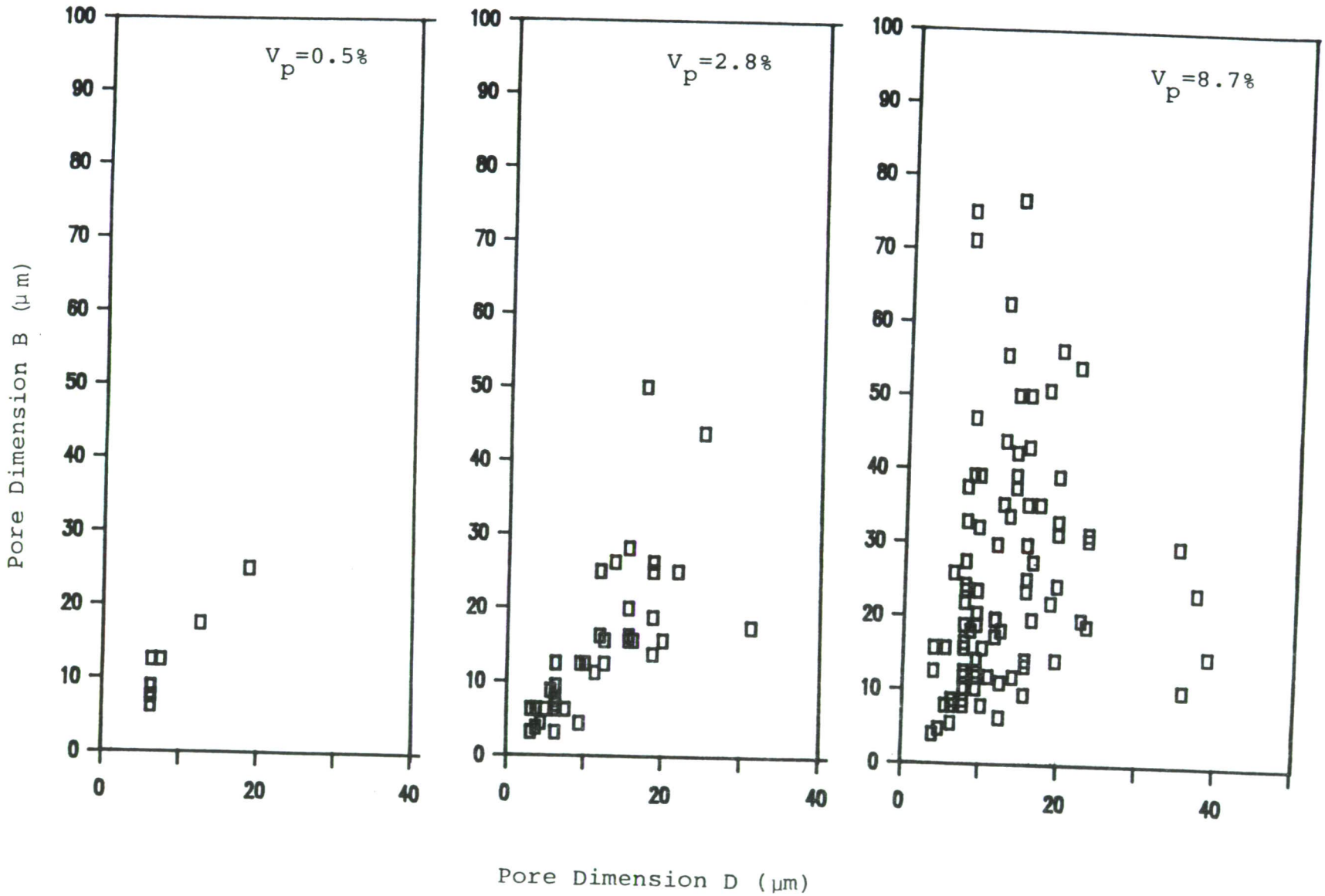

Figure 9. (b) Pore Dimensions B vs. D from Transverse Sections;

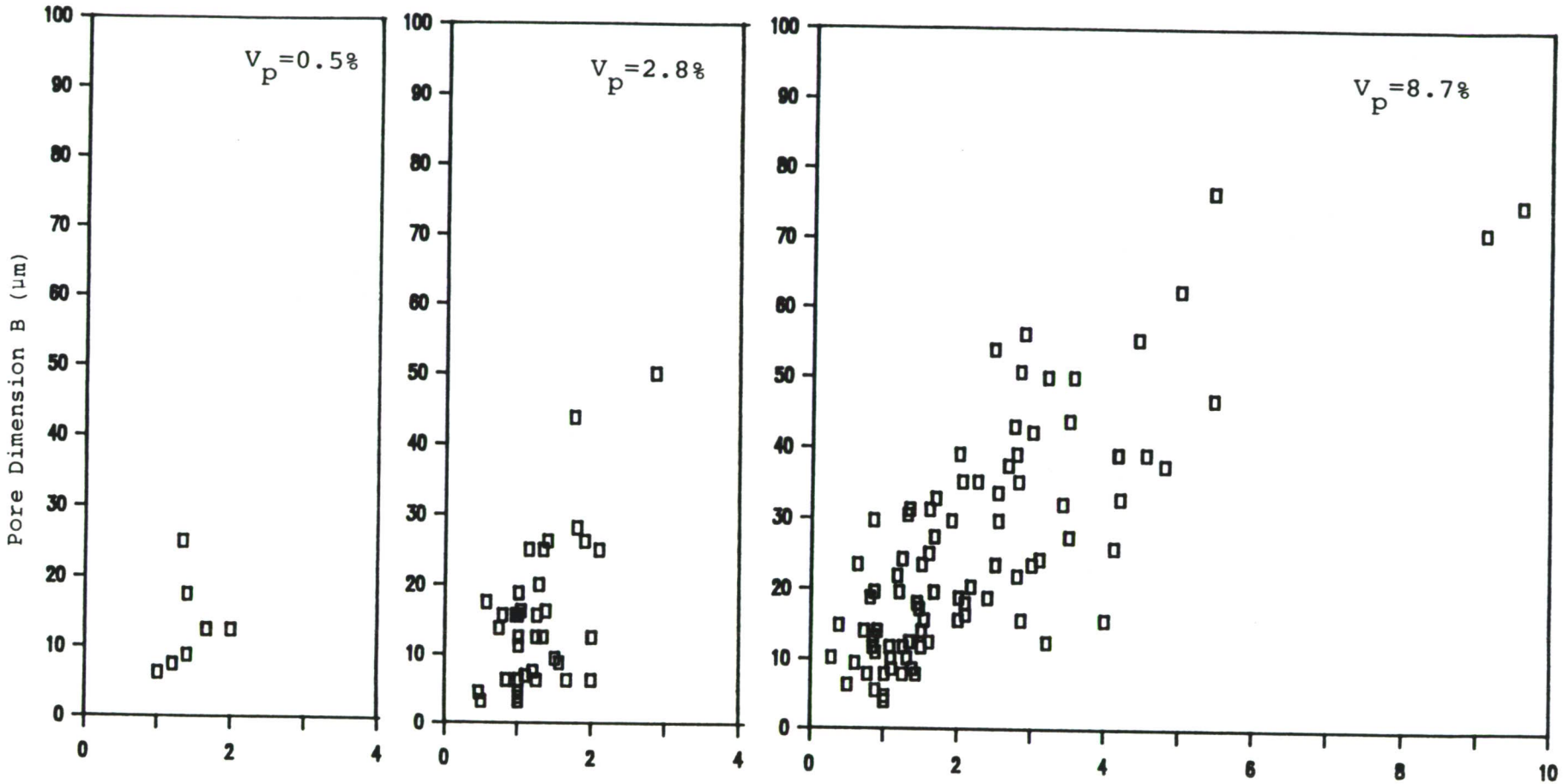

Figure 9. (c) B vs. Aspect Ratio B/D;

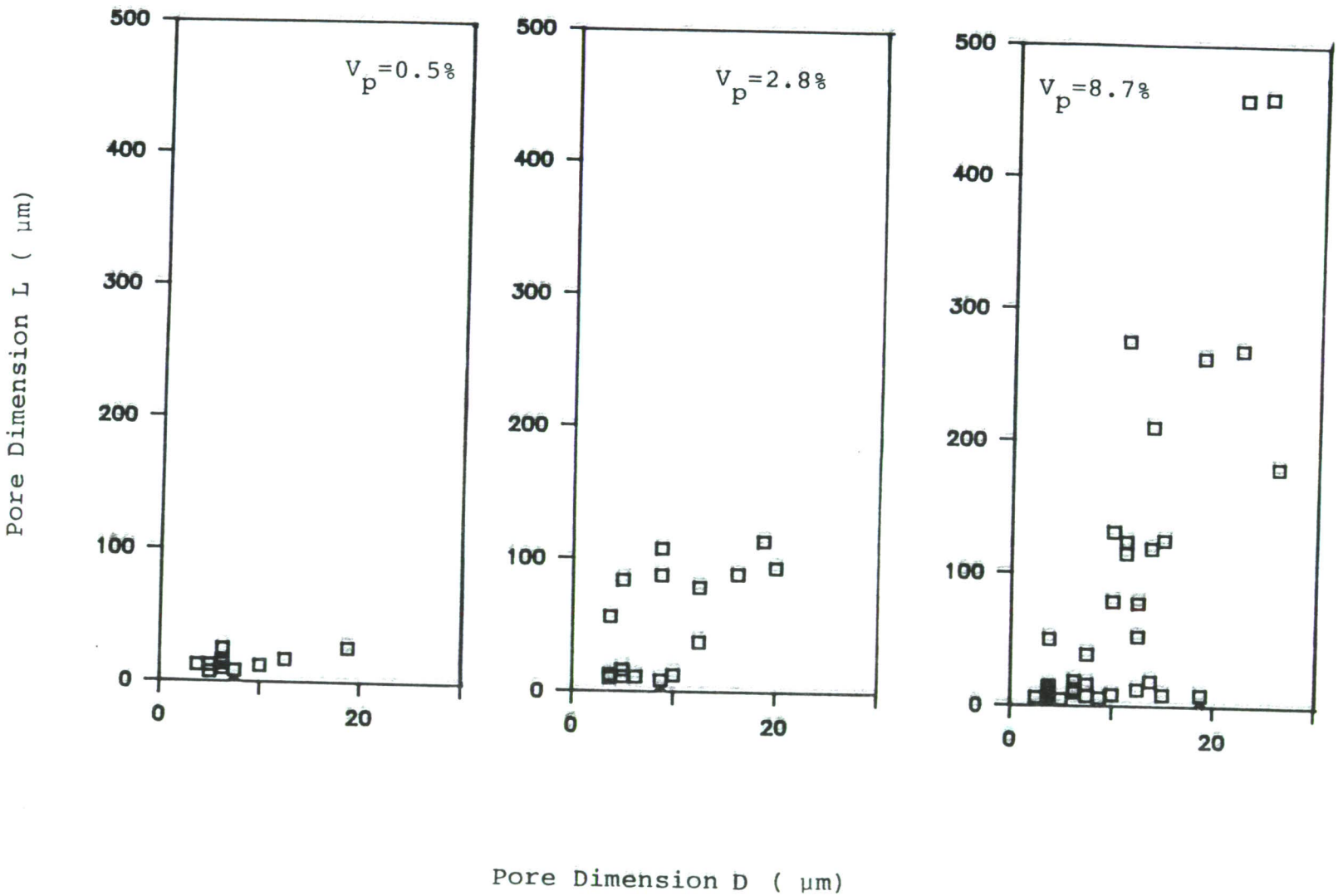

Figure 9. (d) Pore Dimensions L vs. D from Longitudinal Sections;

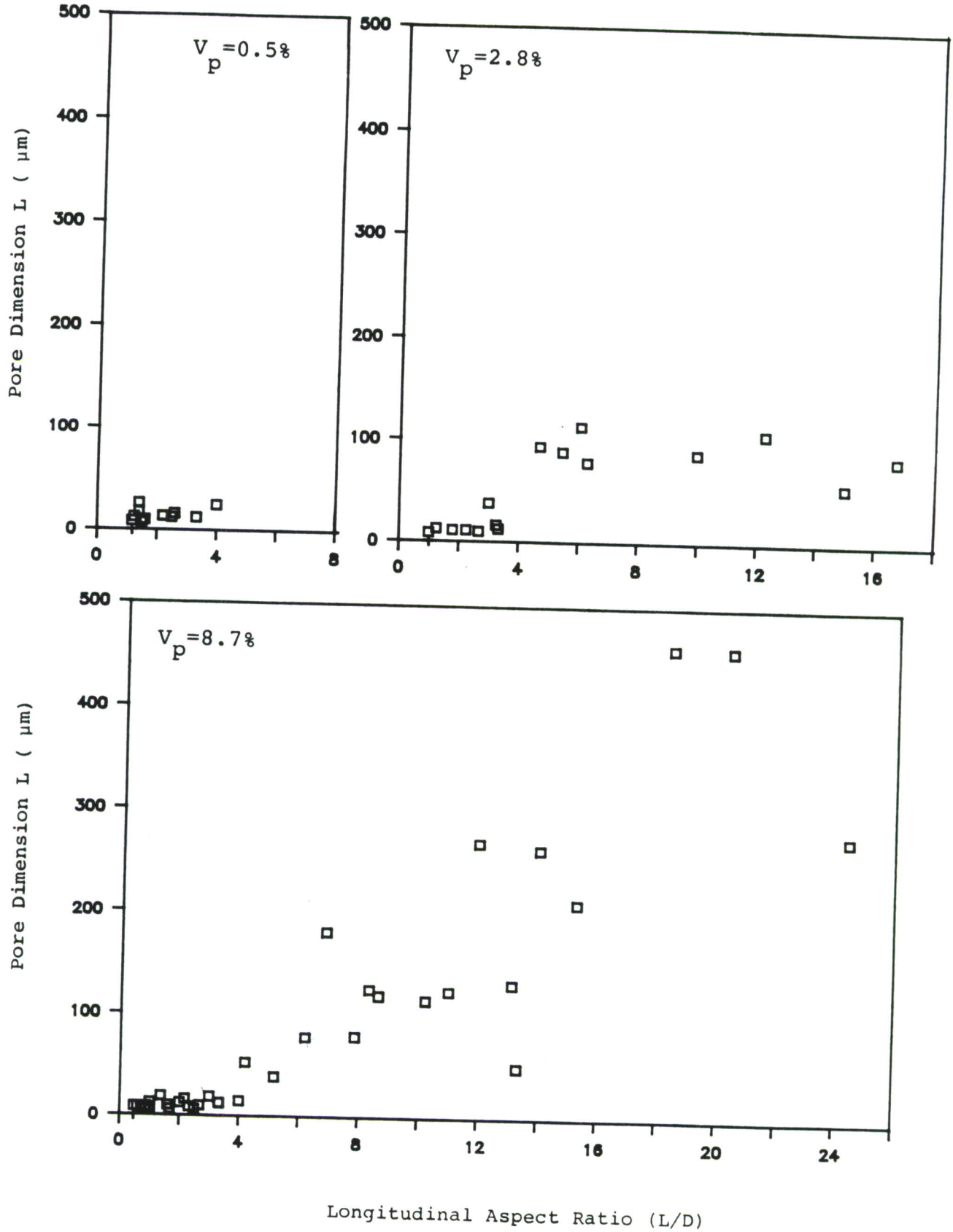

Figure 9. (e) L vs. Aspect Ratio L/D.

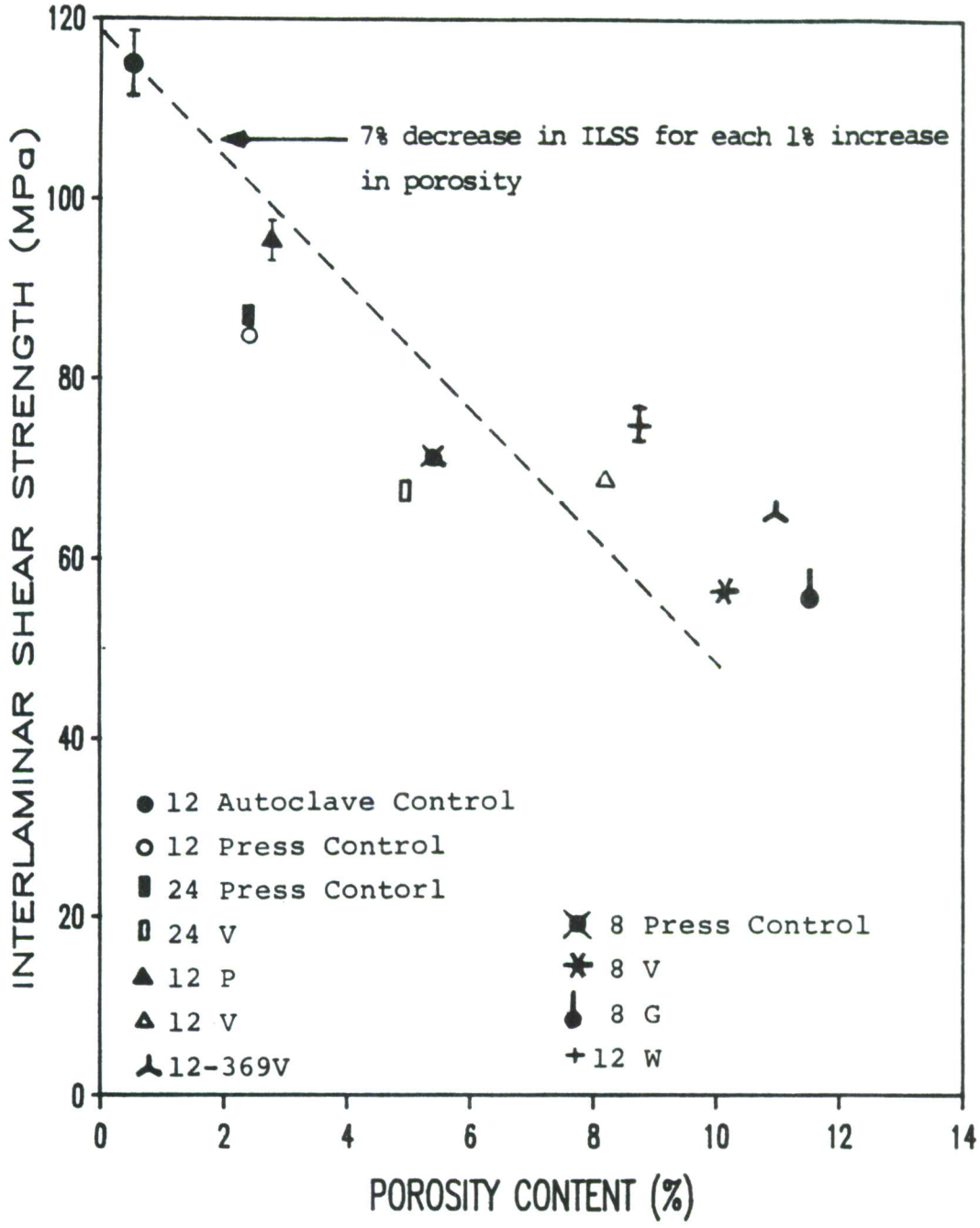

Figure 10. Interlaminar Shear Strength vs. Porosity Content.

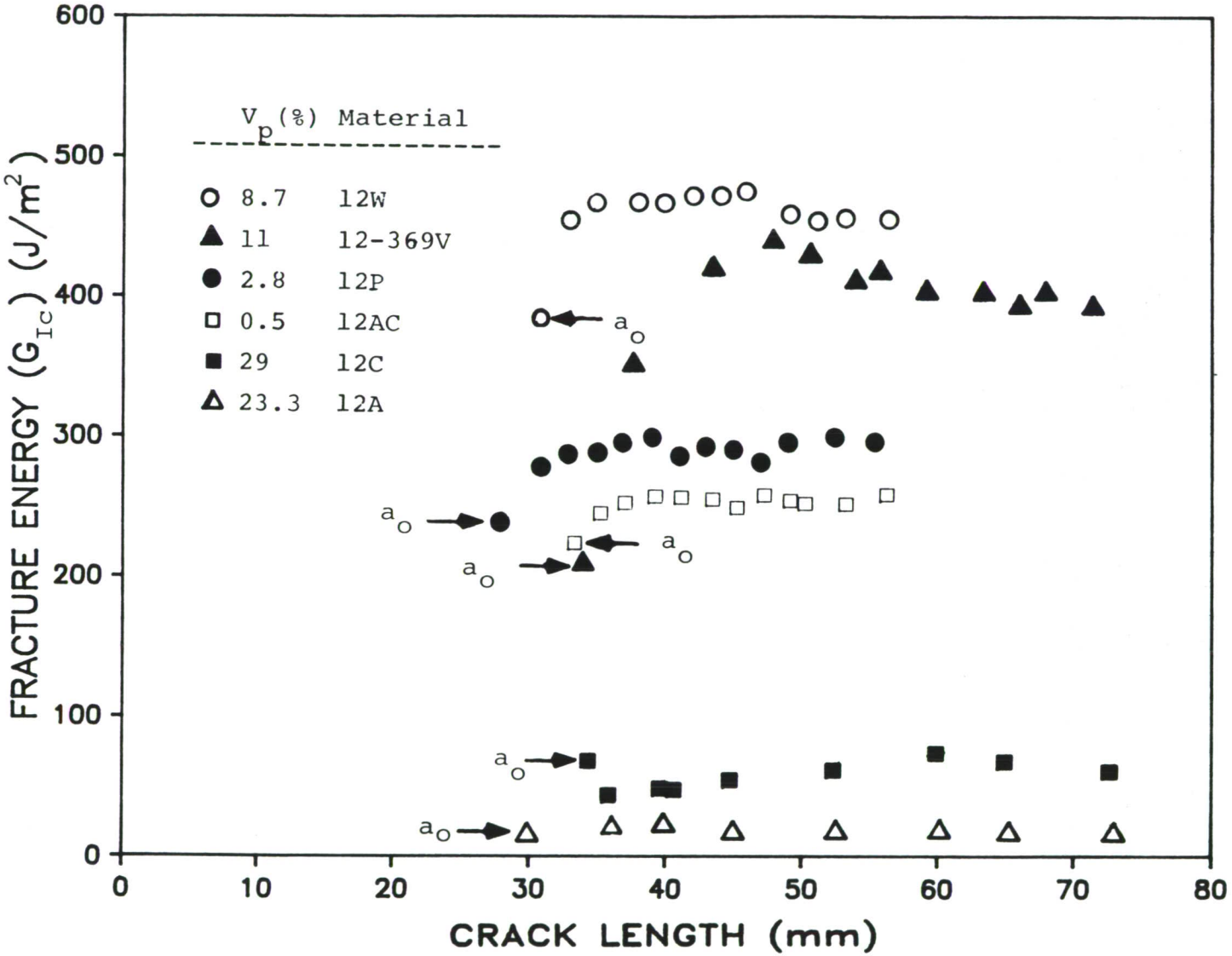

Figure 11. G_{Ic} vs. Crack Extension for Several 12-ply Materials.

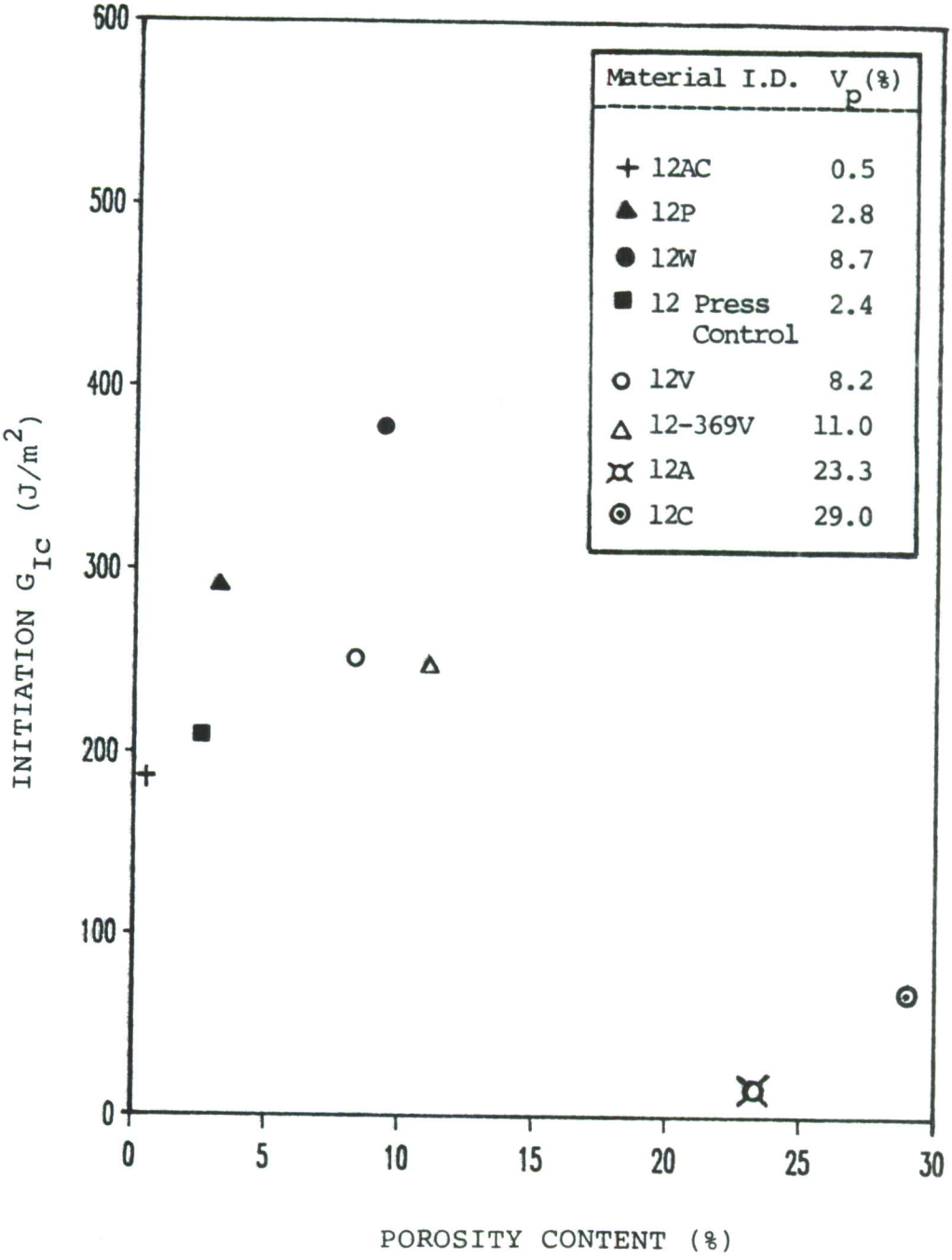

Figure 12. (a) Initiation G_{Ic} vs. Porosity Content;

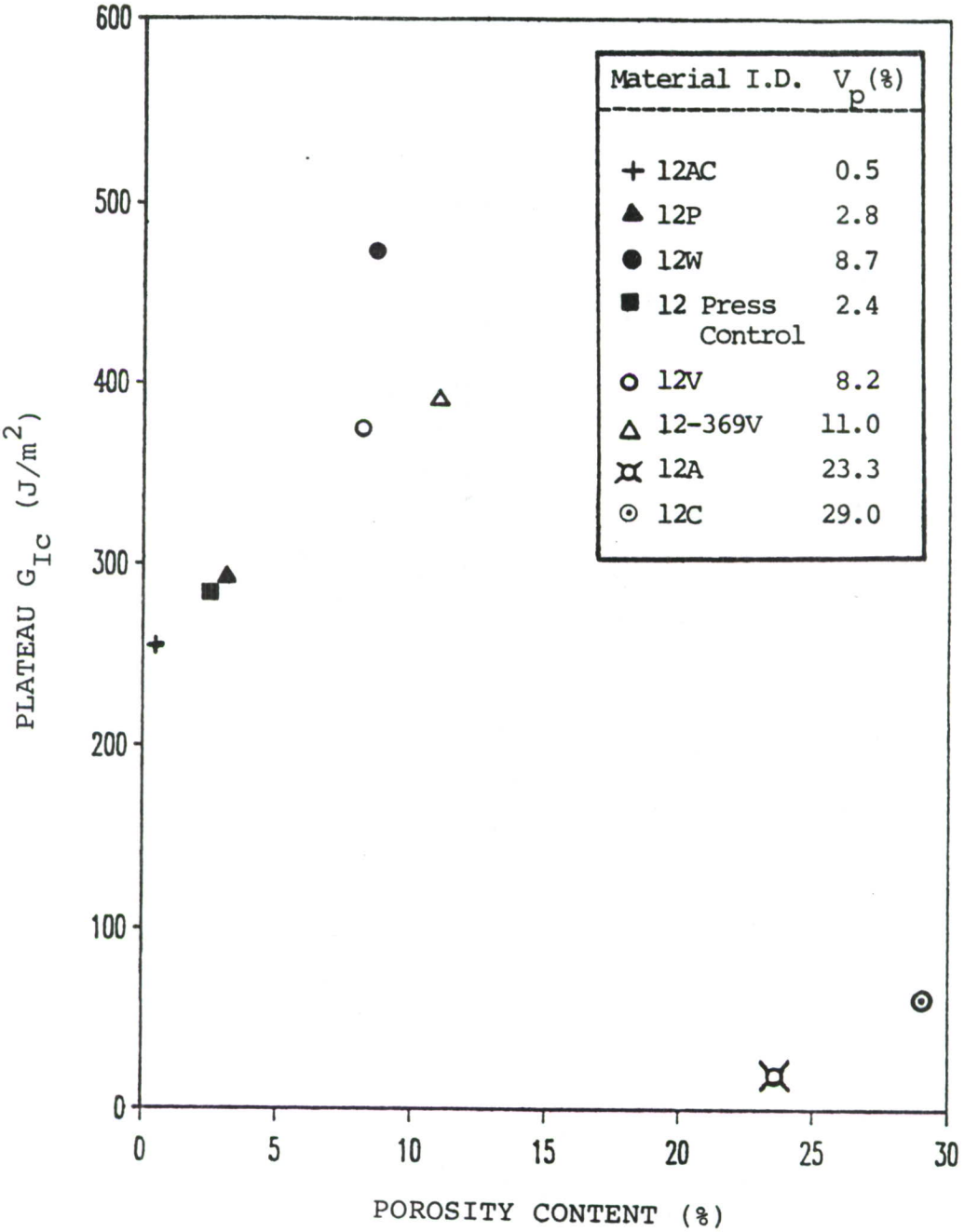

Figure 12. (b) Plateau G_{Ic} vs. Porosity Content.

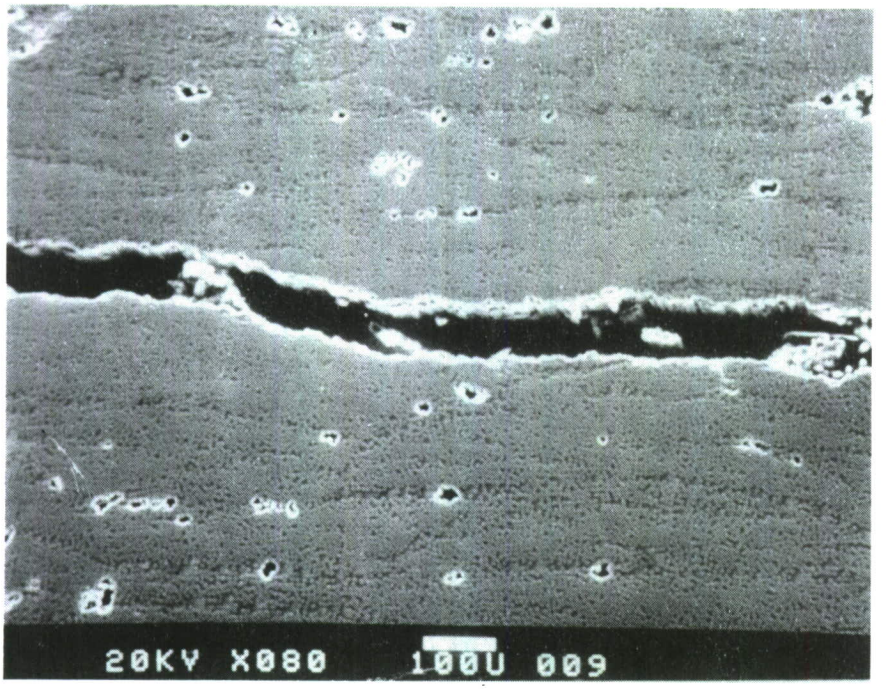

12 PLY PRESS CONTROL
(2.4% POROSITY)

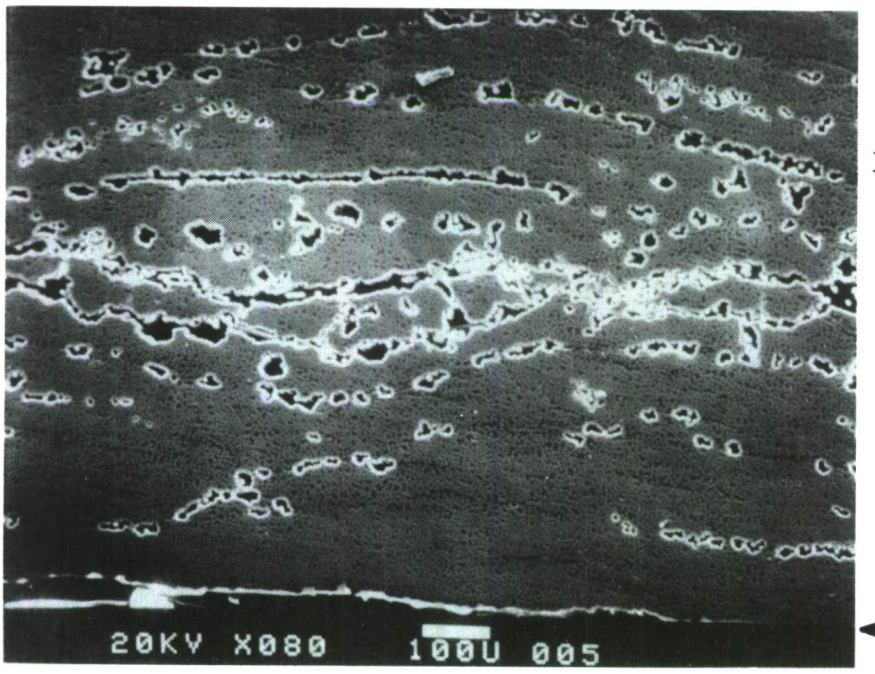

12 V (8.2% POROSITY)

← Main Crack Surface

Figure 13. Transverse Sections (SEM) through Mode I Cracks Showing Multiple Cracking at High Porosity.

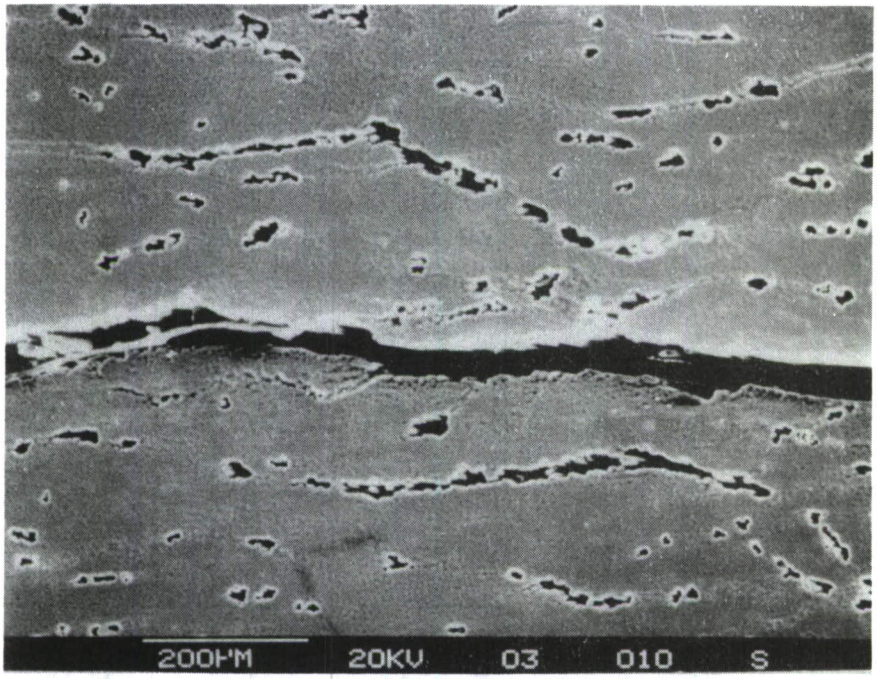

12 W (8.7% POROSITY)

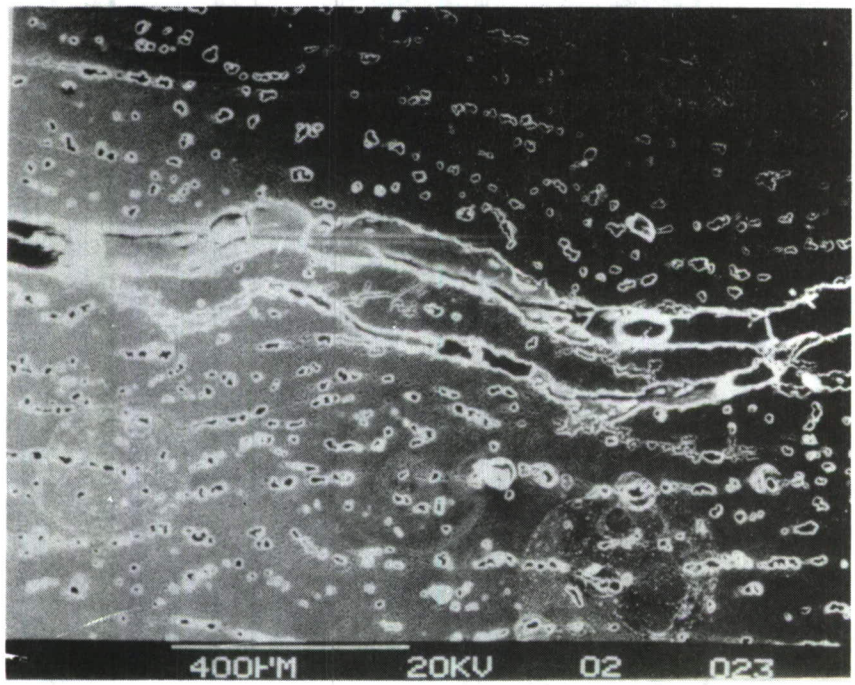

12 W (8.7% POROSITY)

Figure 13 (Continued)

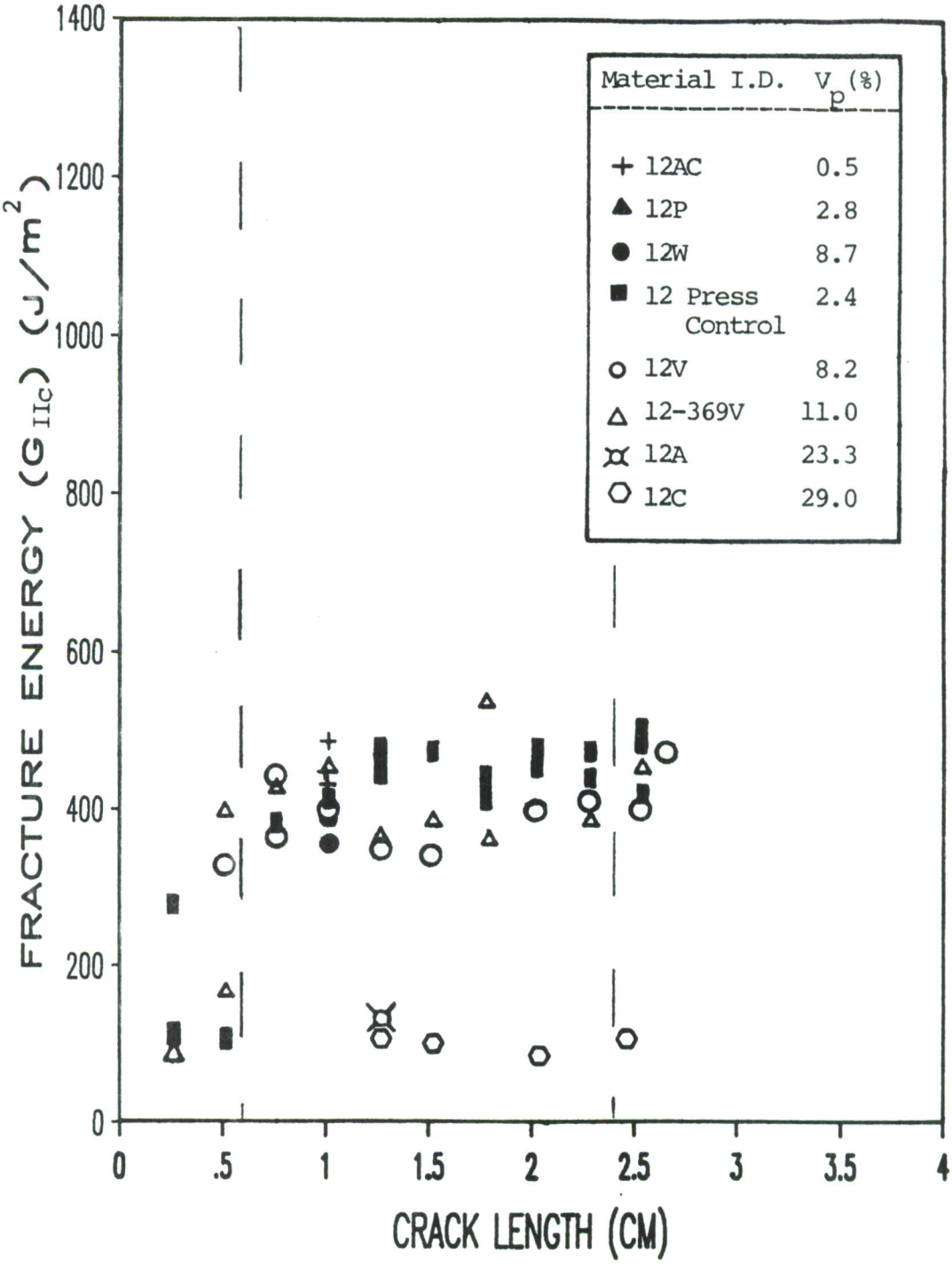

Figure 14. G_{IIc} vs. Crack Length (Crack Tip Position, a, Fig. 7) for Several 12-ply Materials.

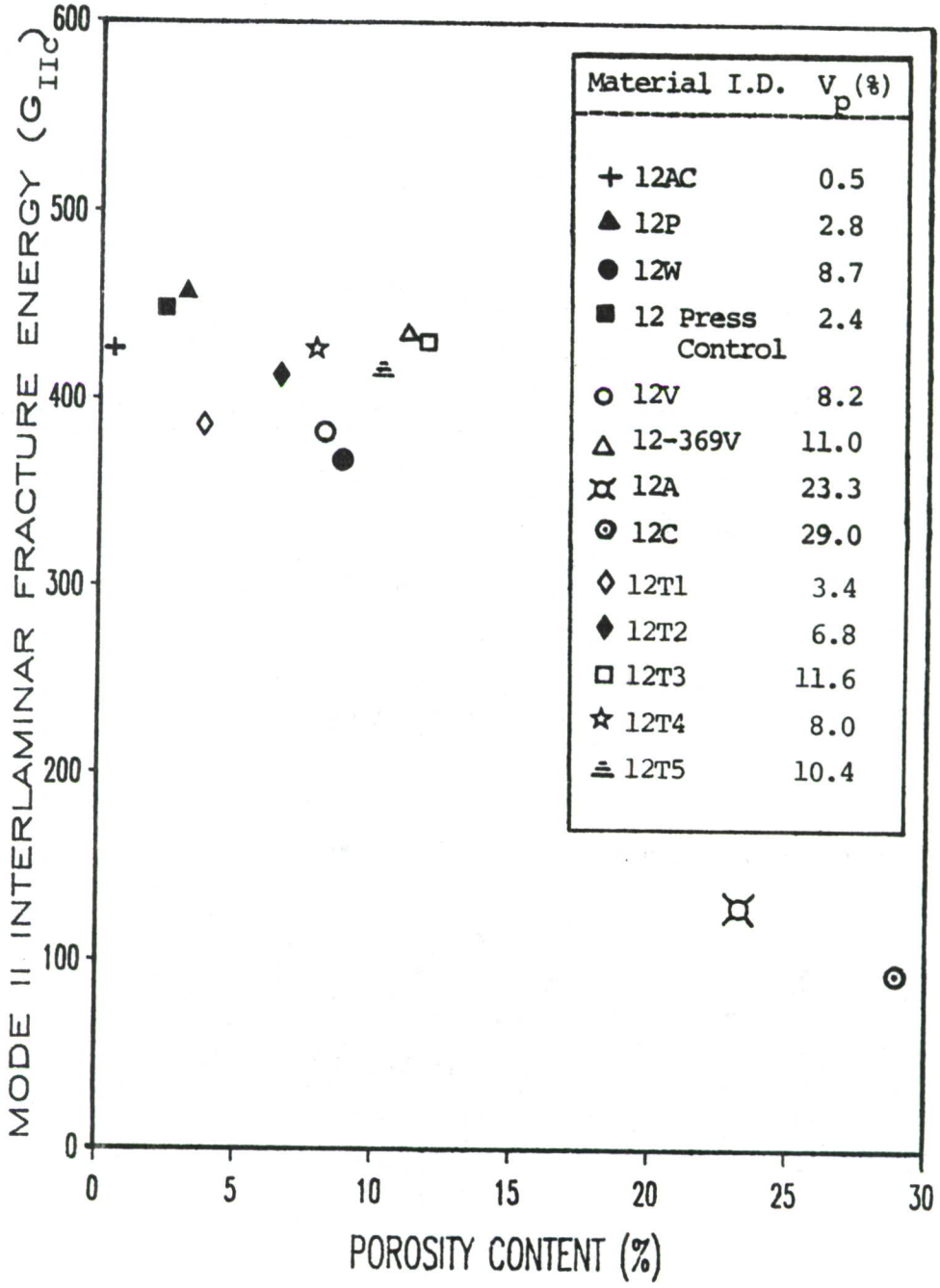

Figure 15. G_{IIc} vs. Porosity Content.

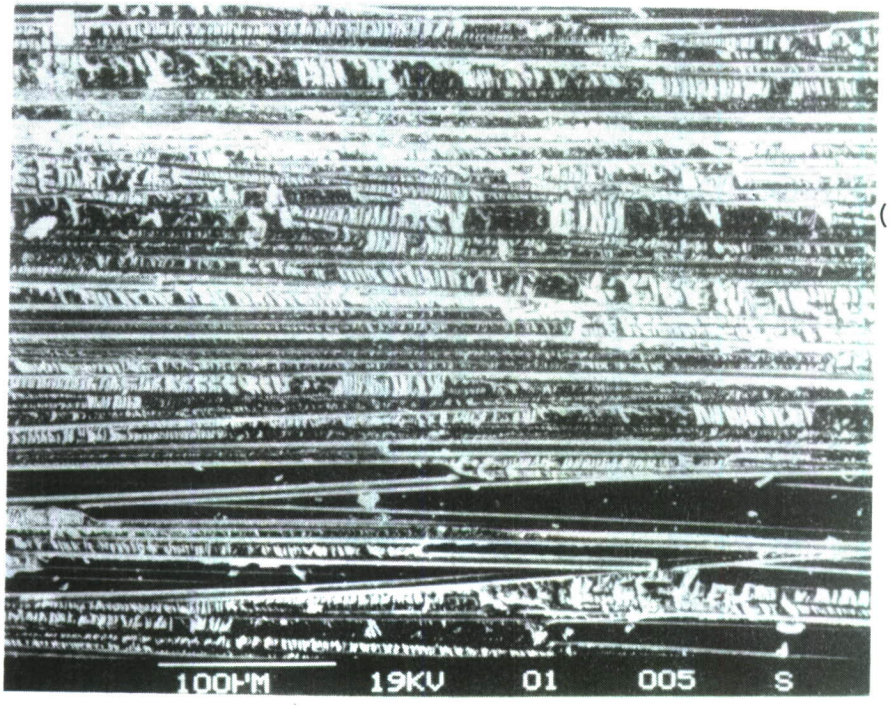

(STATIC)

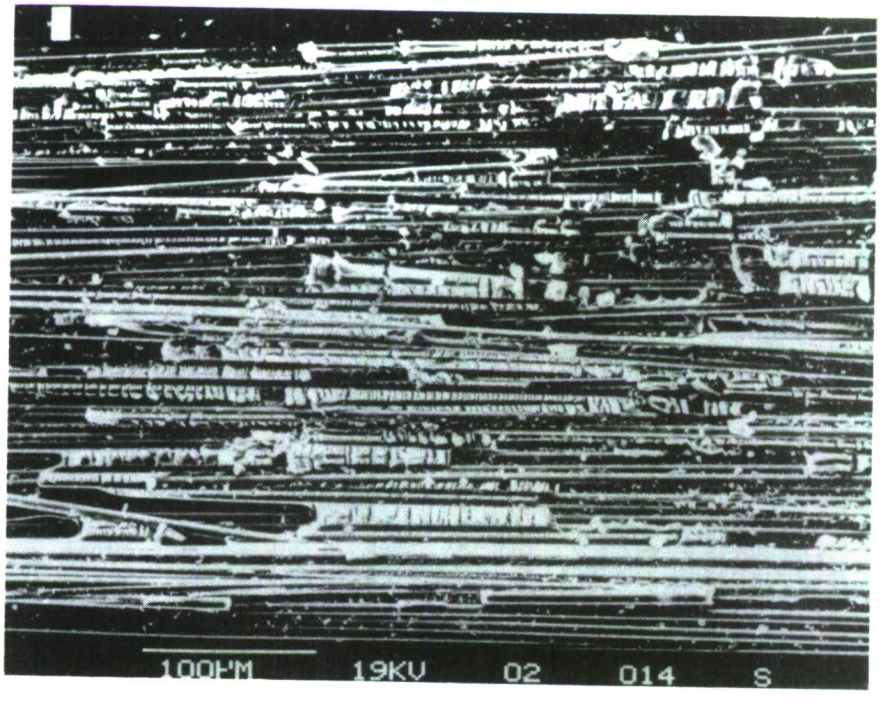

(FATIGUE)

Figure 16. Mode II Static and Fatigue Crack Growth Fracture Surfaces (V_p=8.7%, dry).

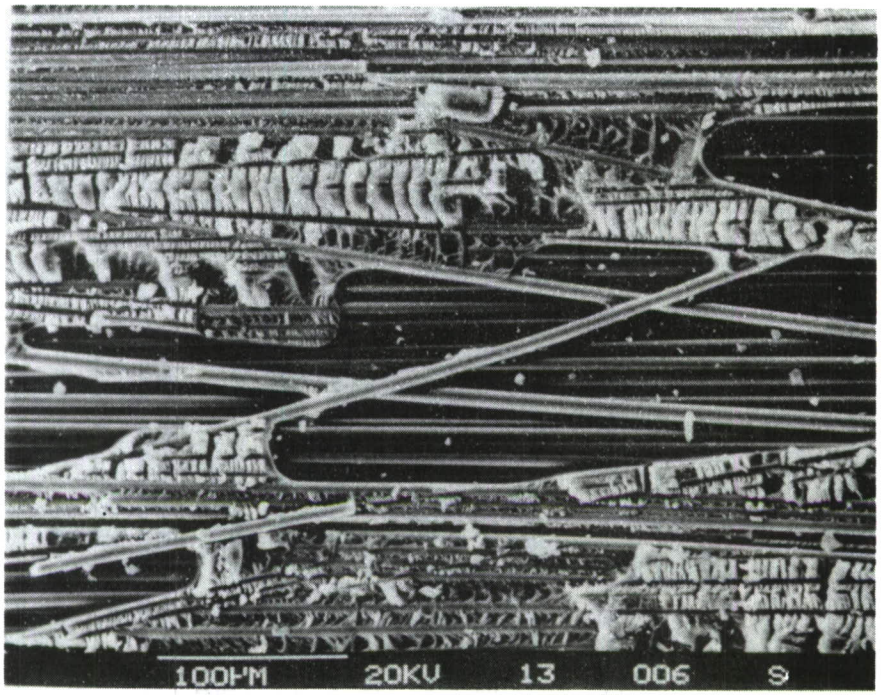

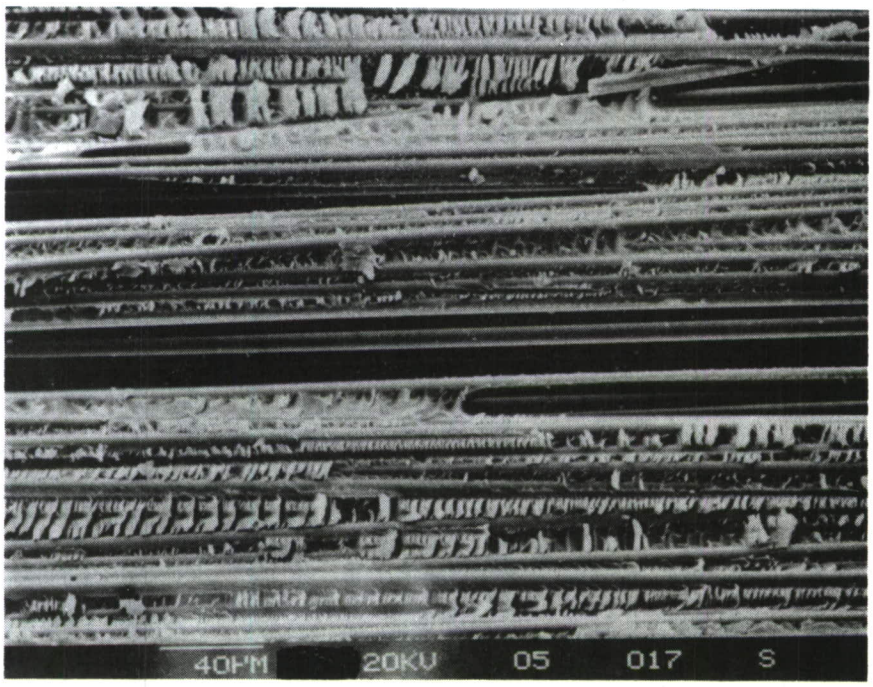

Figure 17. Short Beam Fatigue Fracture Surfaces (V_p=8.7%, Dry).

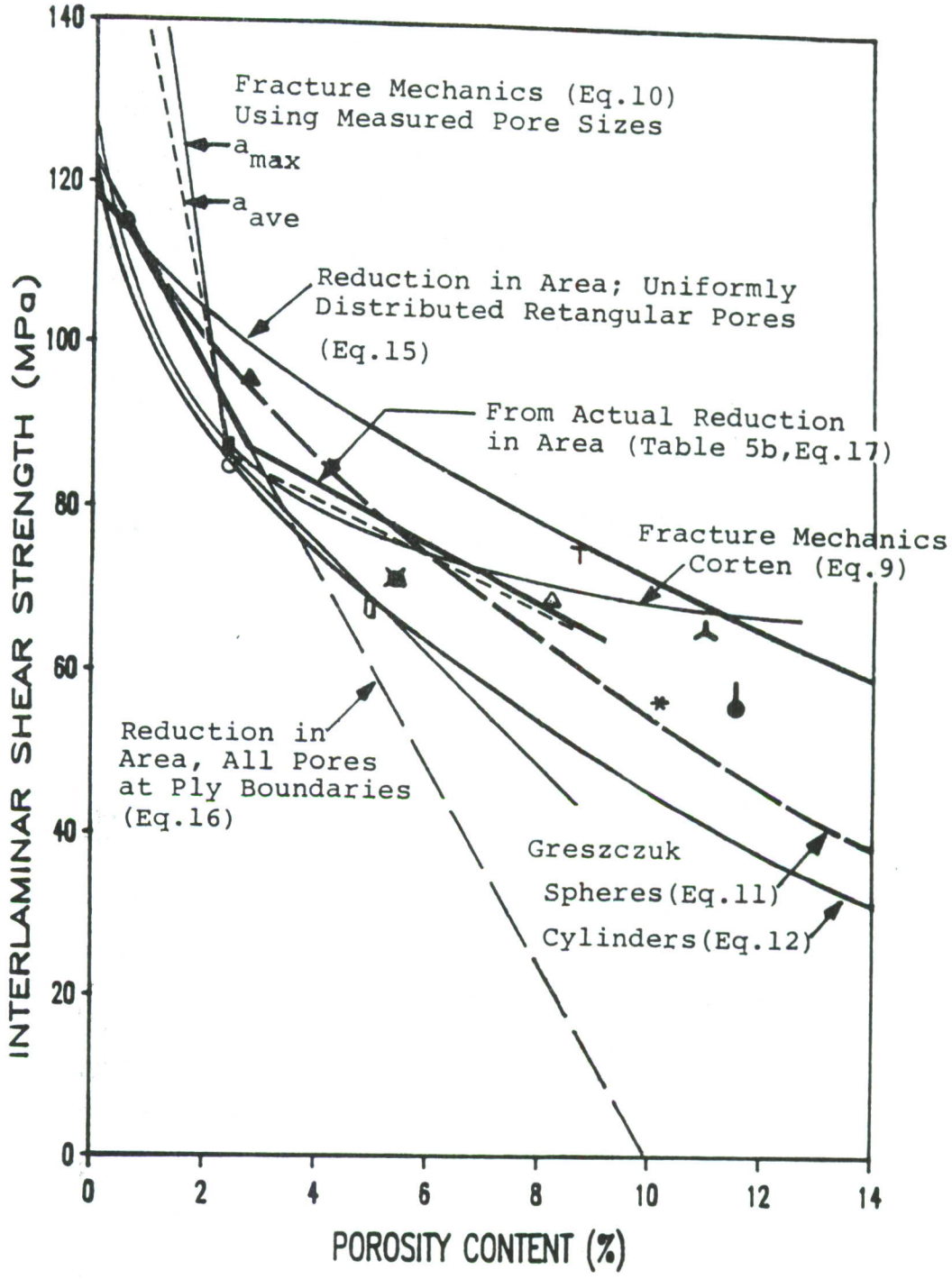

Figure 18. Predicted ILSS vs. Porosity Compared with Experimental Data from Figure 10.

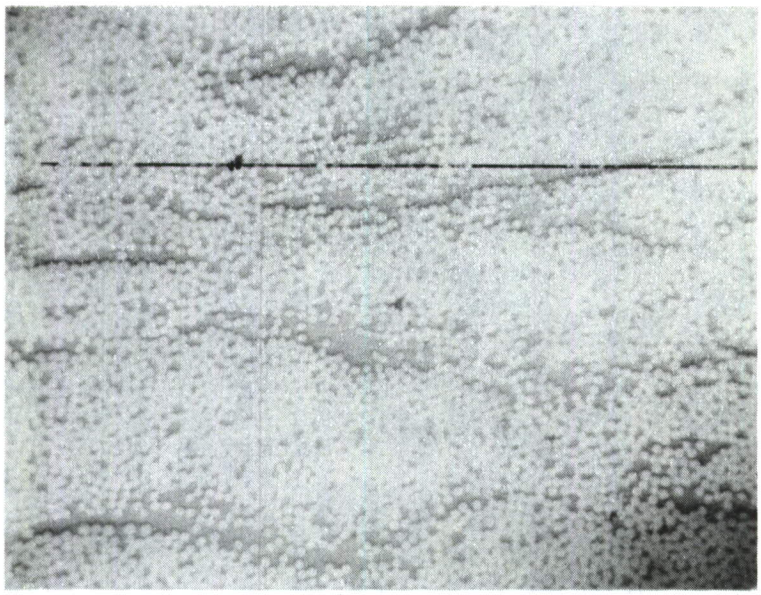

12AC (x160)
(V_p=0.5%)

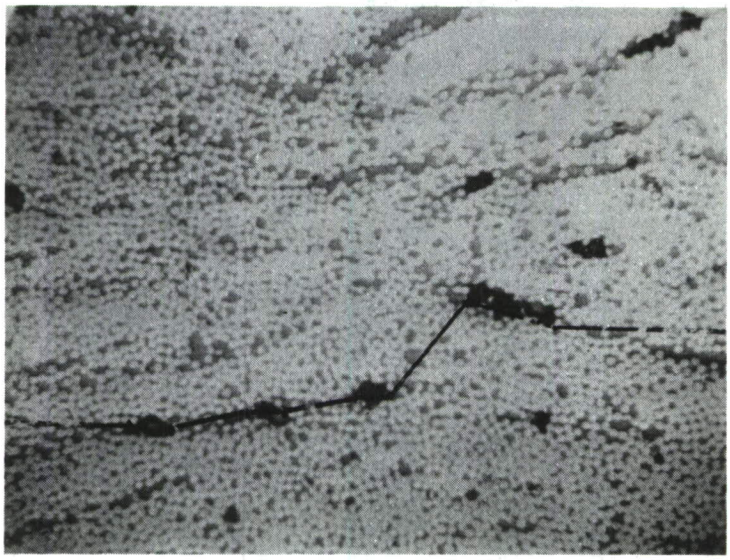

12P (x160)
(V_p=2.8%)

12W (x128)
(V_p=8.7%)

Figure 19. (a) Typical Paths of Greatest Reduction in Area on Micrographs.

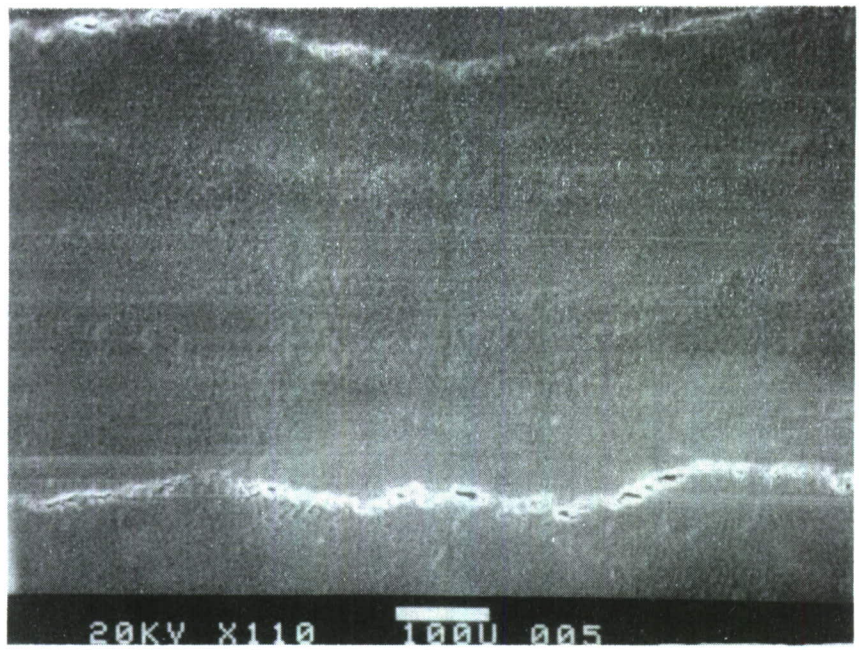

Material 12AC (V_p=0.5%)

Material 12P (V_p=2.8%)

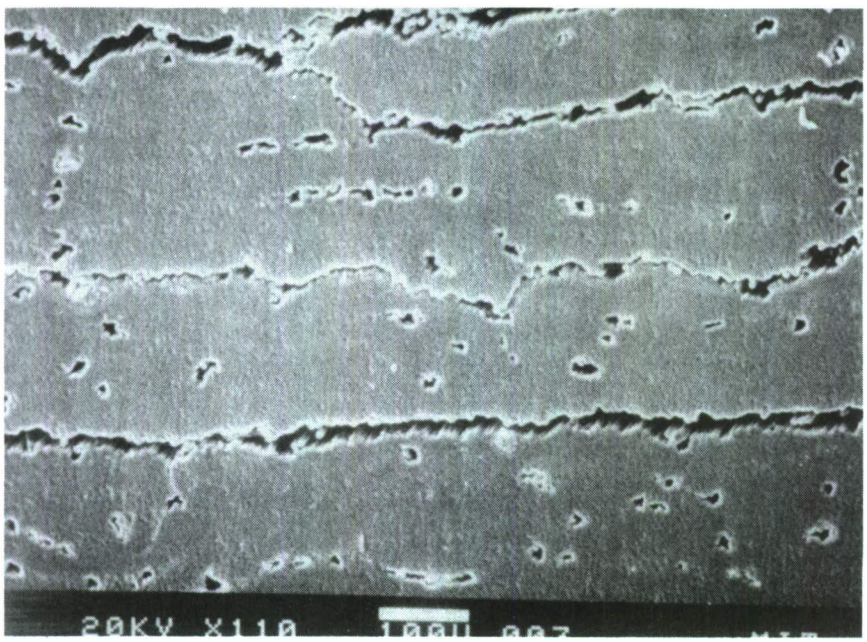

Material 12W (V_p=8.7%)

Figure 19 (b) Typical Cross-Section through Fatigue Cracks in Short Beam Specimens.

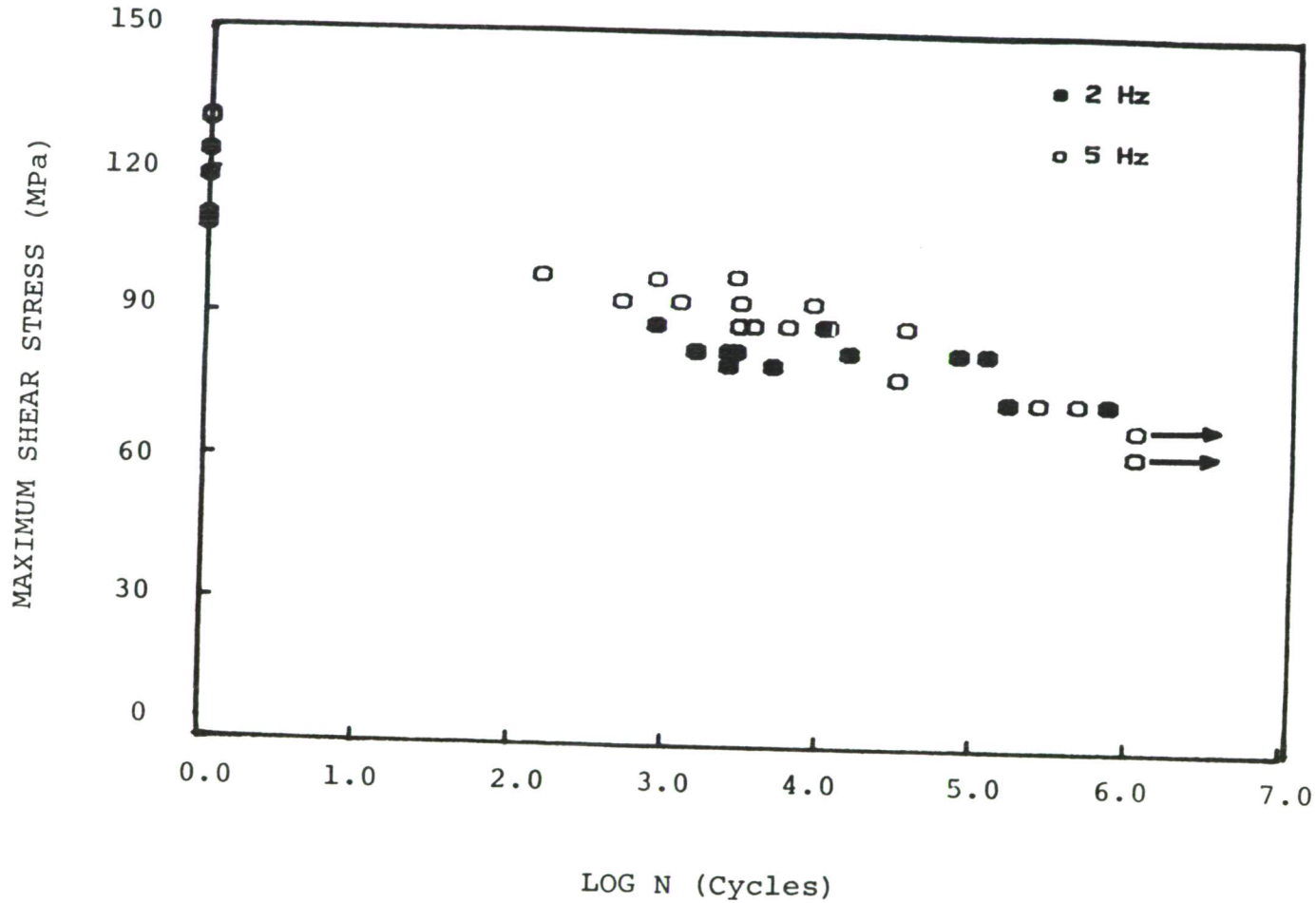

Figure 20. Short Beam Shear Fatigue S-N Data at 2 and 5 Hz Frequency (V_p=.5%).

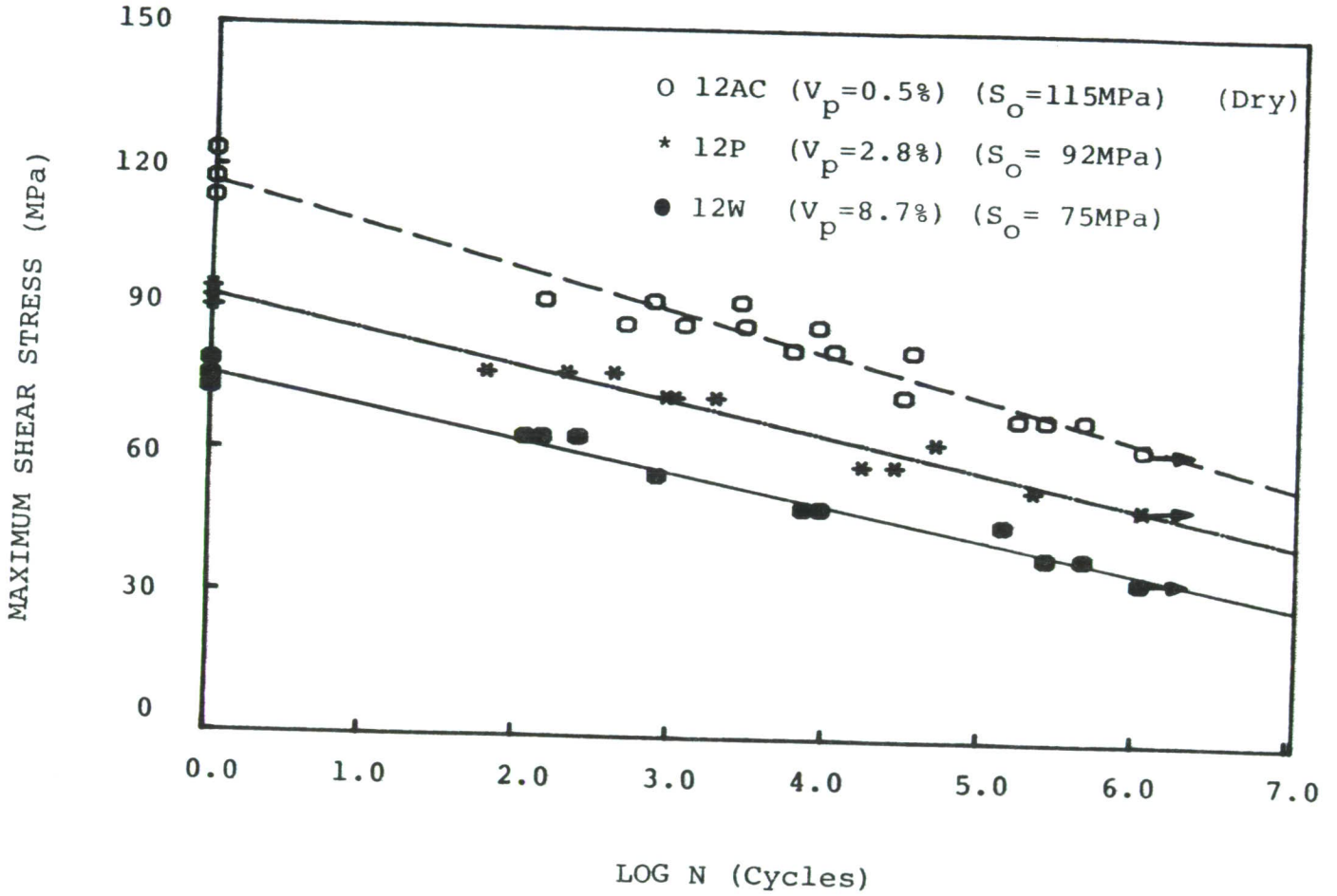

Figure 21. Effect of Porosity Level on Short Beam Shear Fatigue S-N Data.

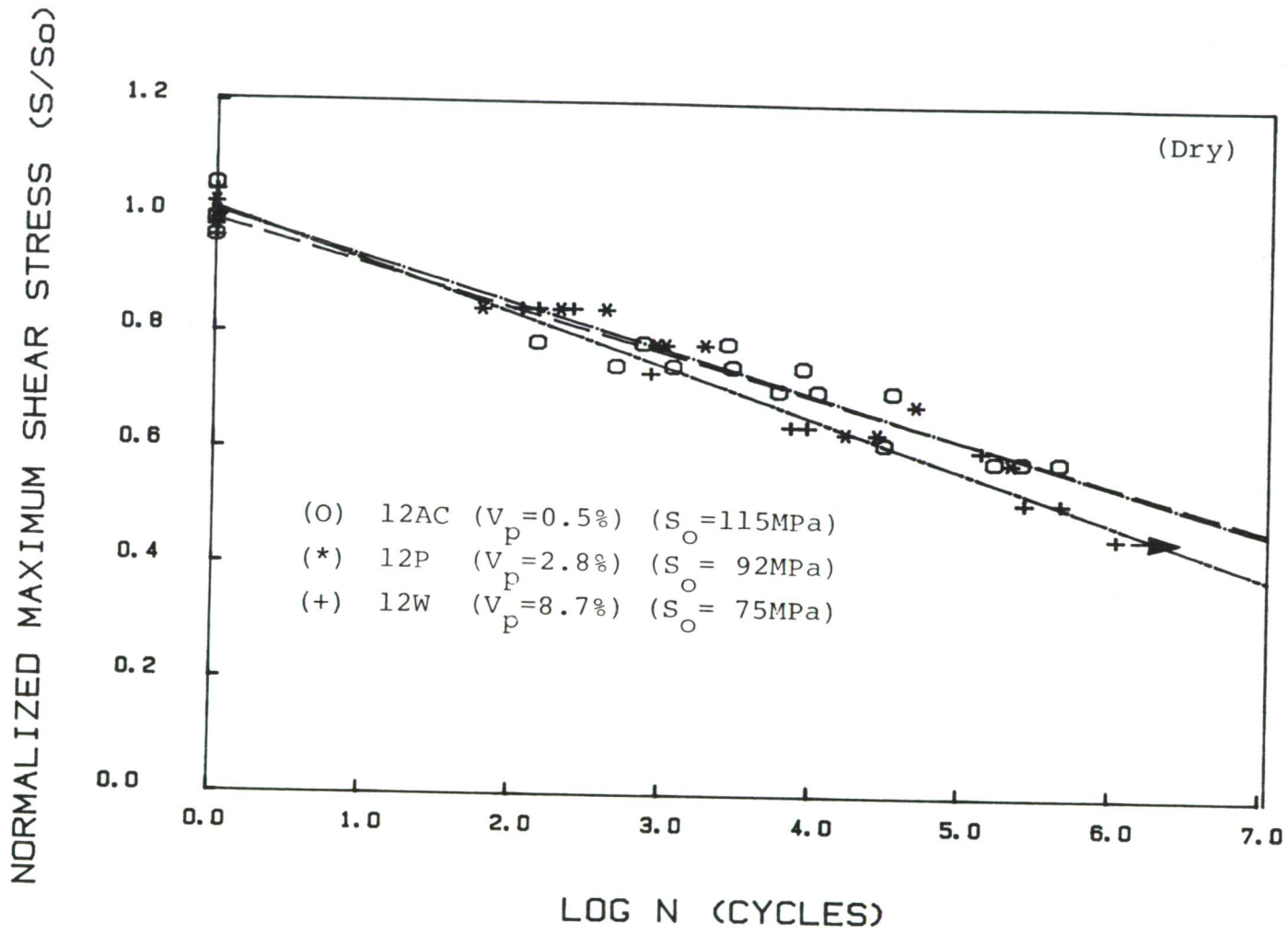

Figure 22. Data from Figure 21 Normalized by the Static Average ILSS (S_o).

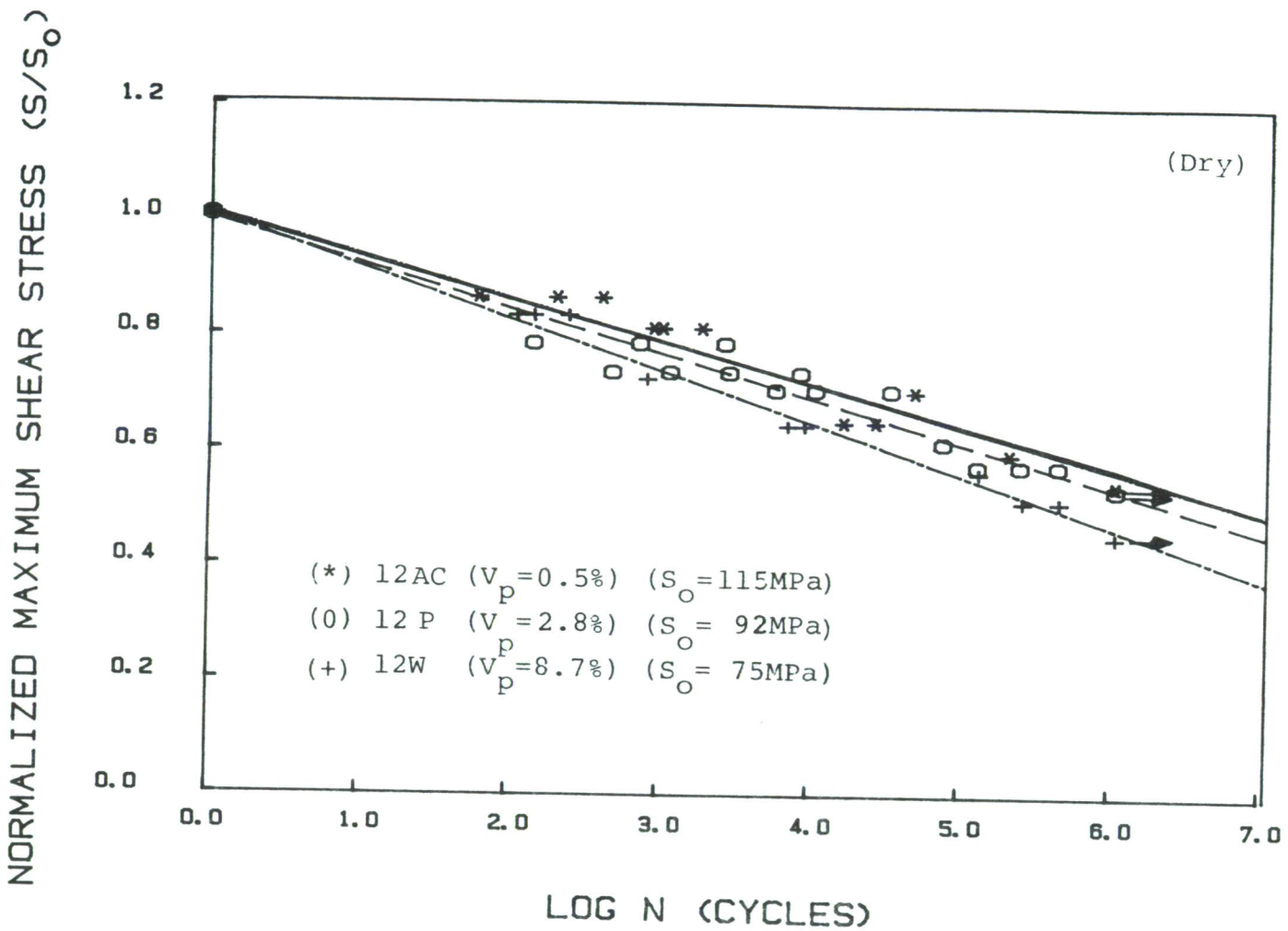

Figure 23. Data from Figure 22, but with Curve Fits Forced through $S/S_o = 1.0$.

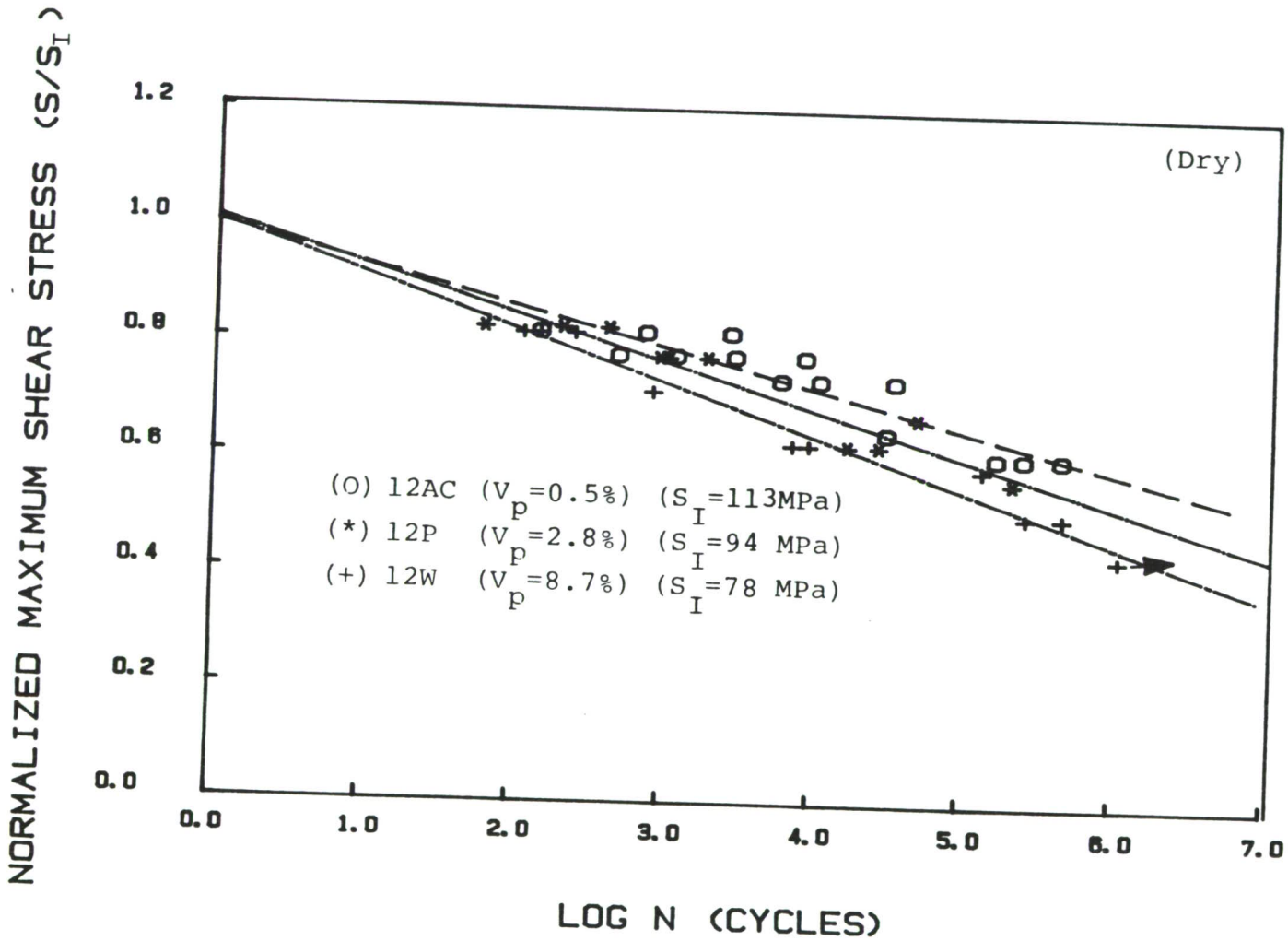

Figure 24. Curve Fits to Cyclic Data Only, Normalized by Intercept at Log N = 0.

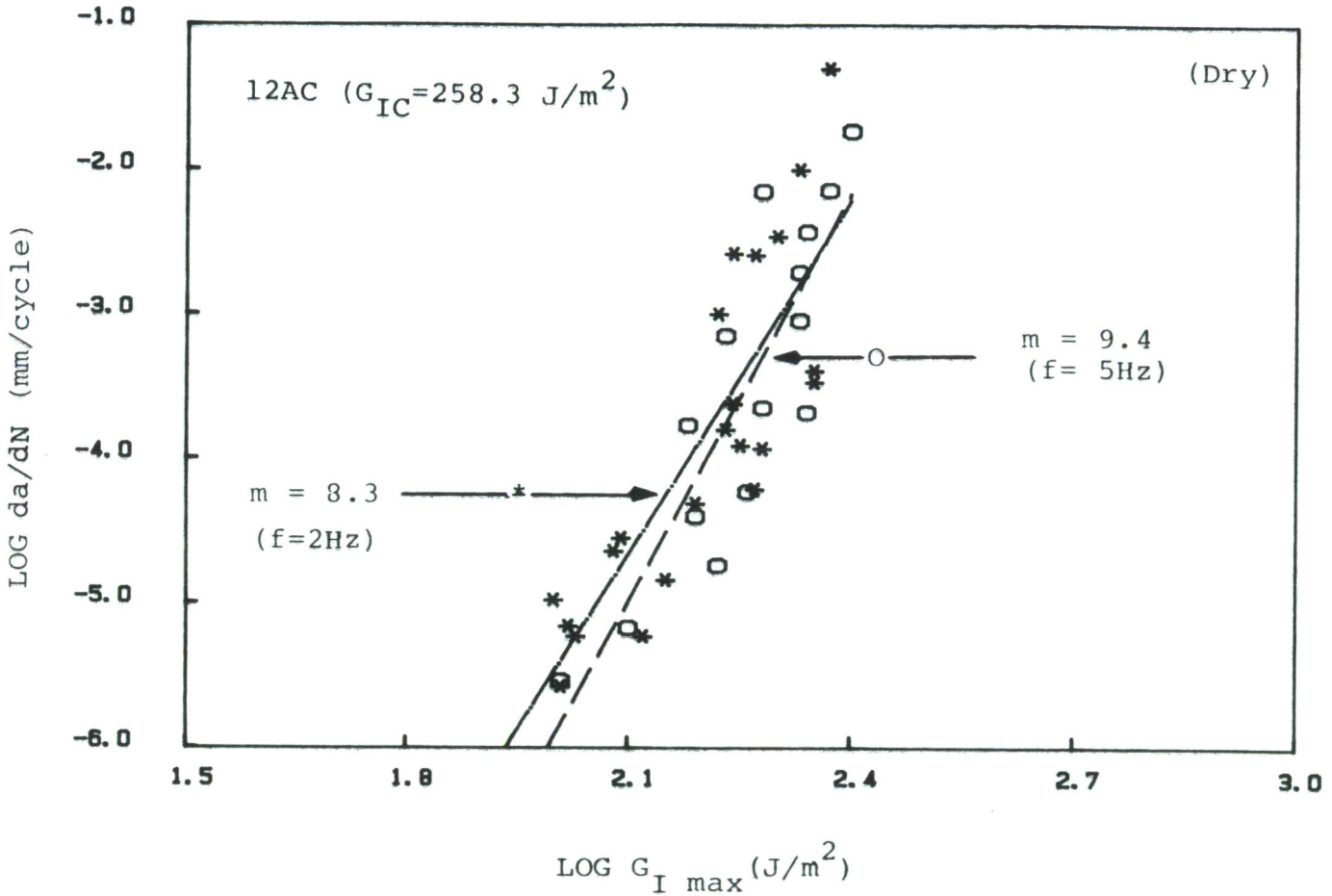

Figure 25. Mode I Fatigue Crack Growth Data at 2 and 5 Hz Frequency (V_p = 0.5%).

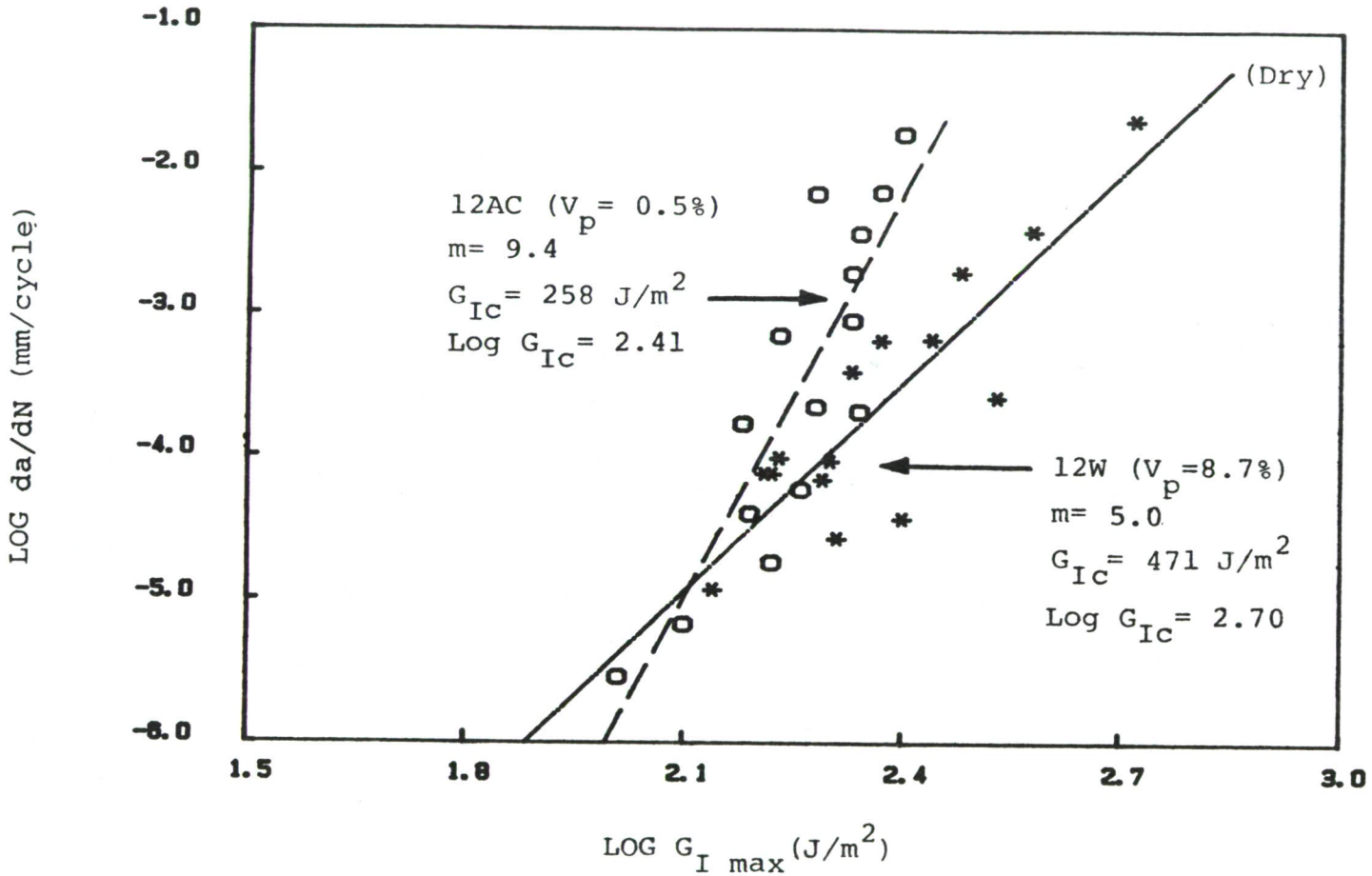

Figure 26. Mode I Fatigue Crack Growth Data for High vs. Low Porosity Materials.

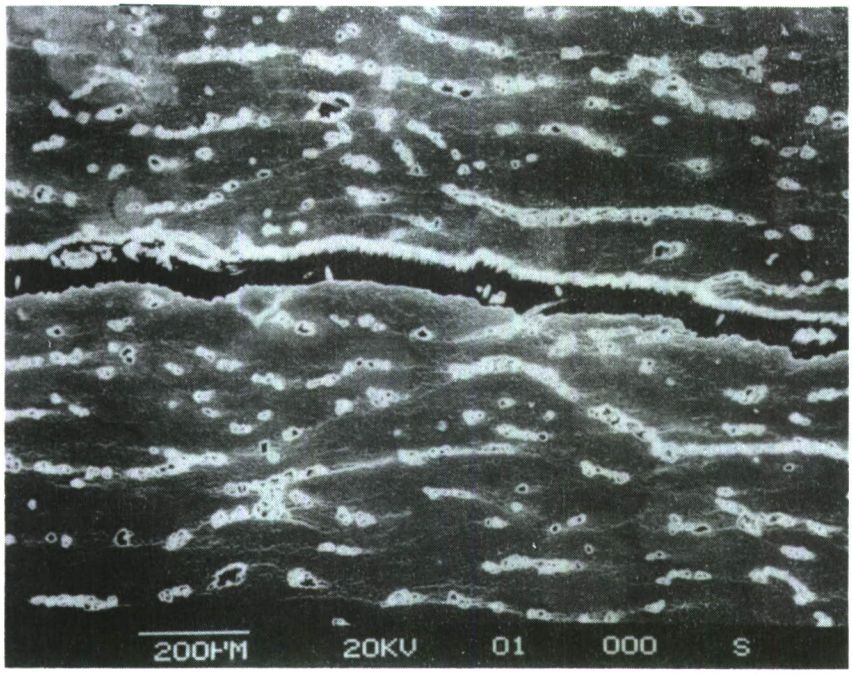

G_{Imax}= 250 J/m^2

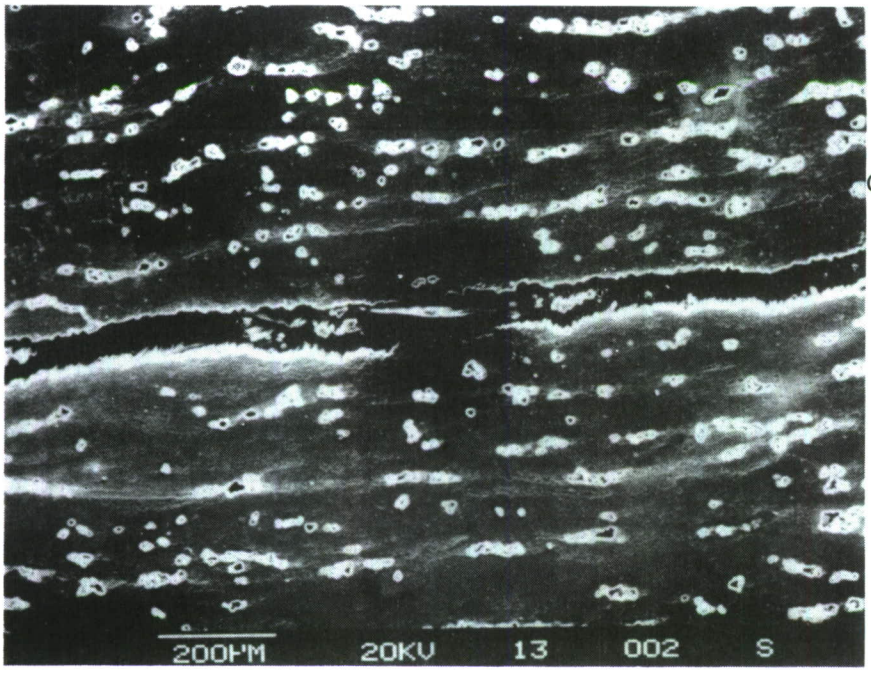

G_{Imax}= 138 J/m^2

Figure 27. Transverse Section through High Porosity Mode I Fatigue Cracks at High and Low G_{Imax} Values Showing Reduction in Multiple Cracking at Low G_{Imax}.

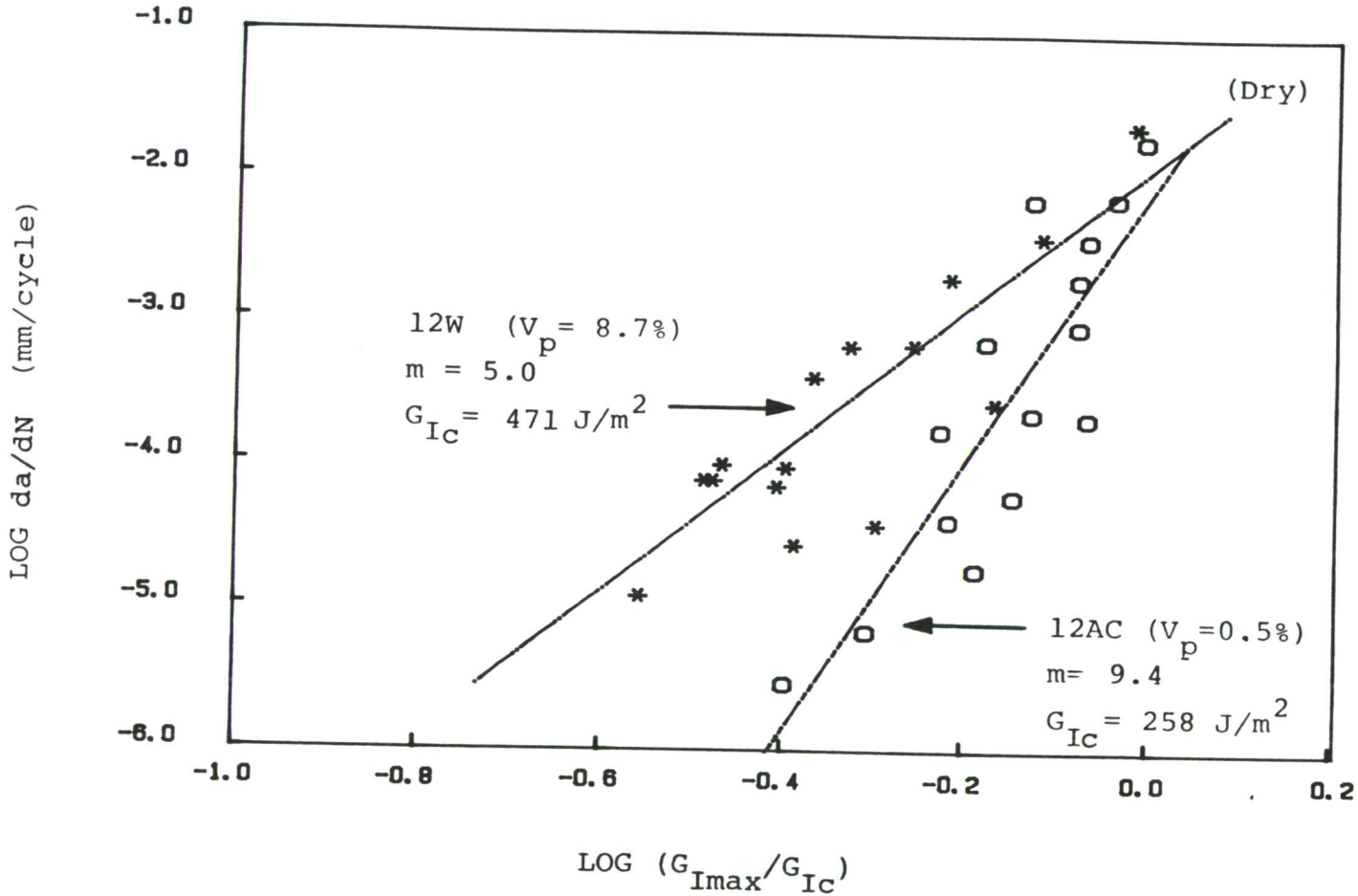

Figure 28. Data from Figure 26 Normalized by G_{IC}.

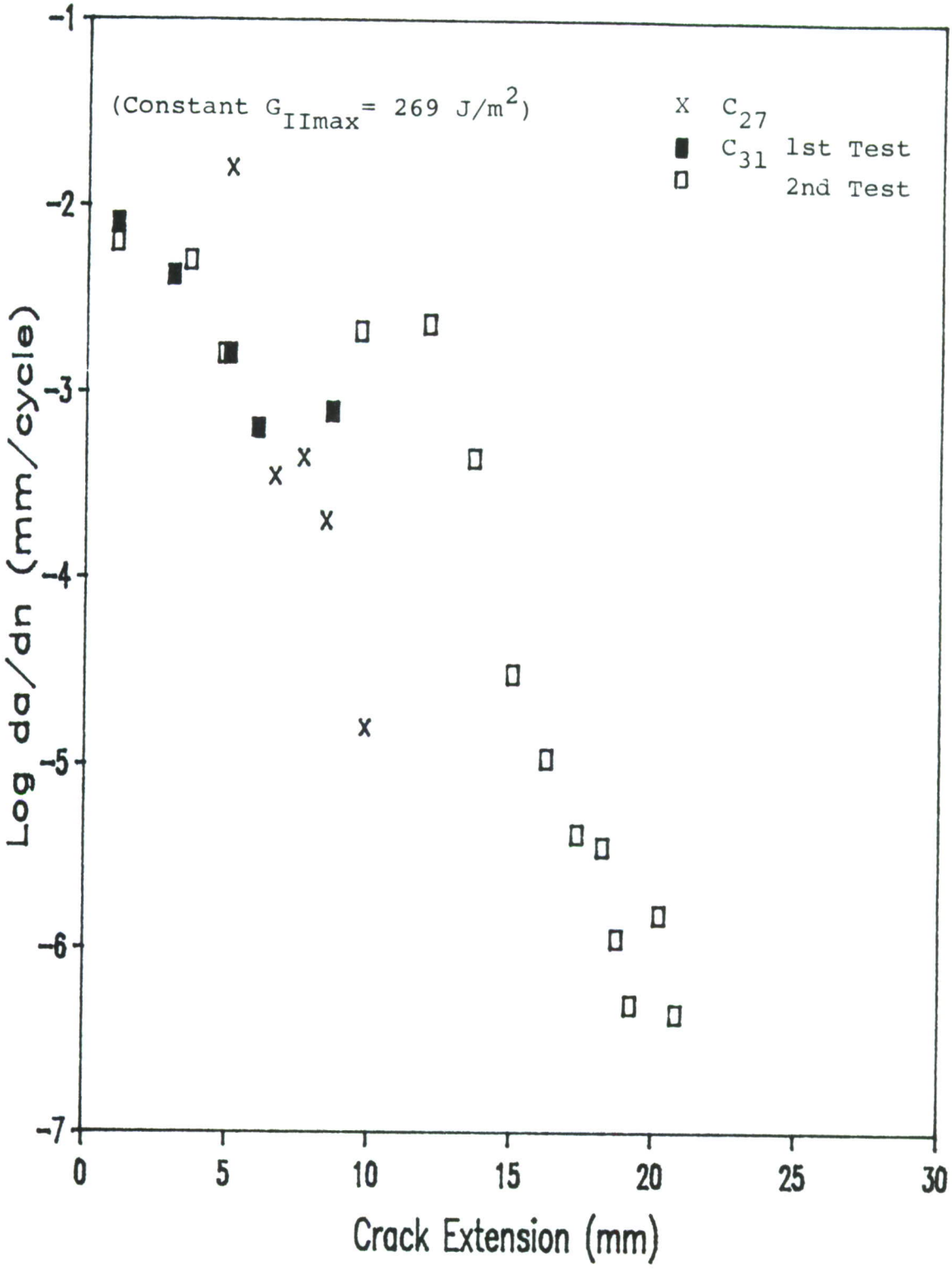

Figure 29. Deceleration of Mode II Fatigue Cracks with Crack Extension Distance at Constant G_{IImax}, Due to Uneven Crack Front Development.

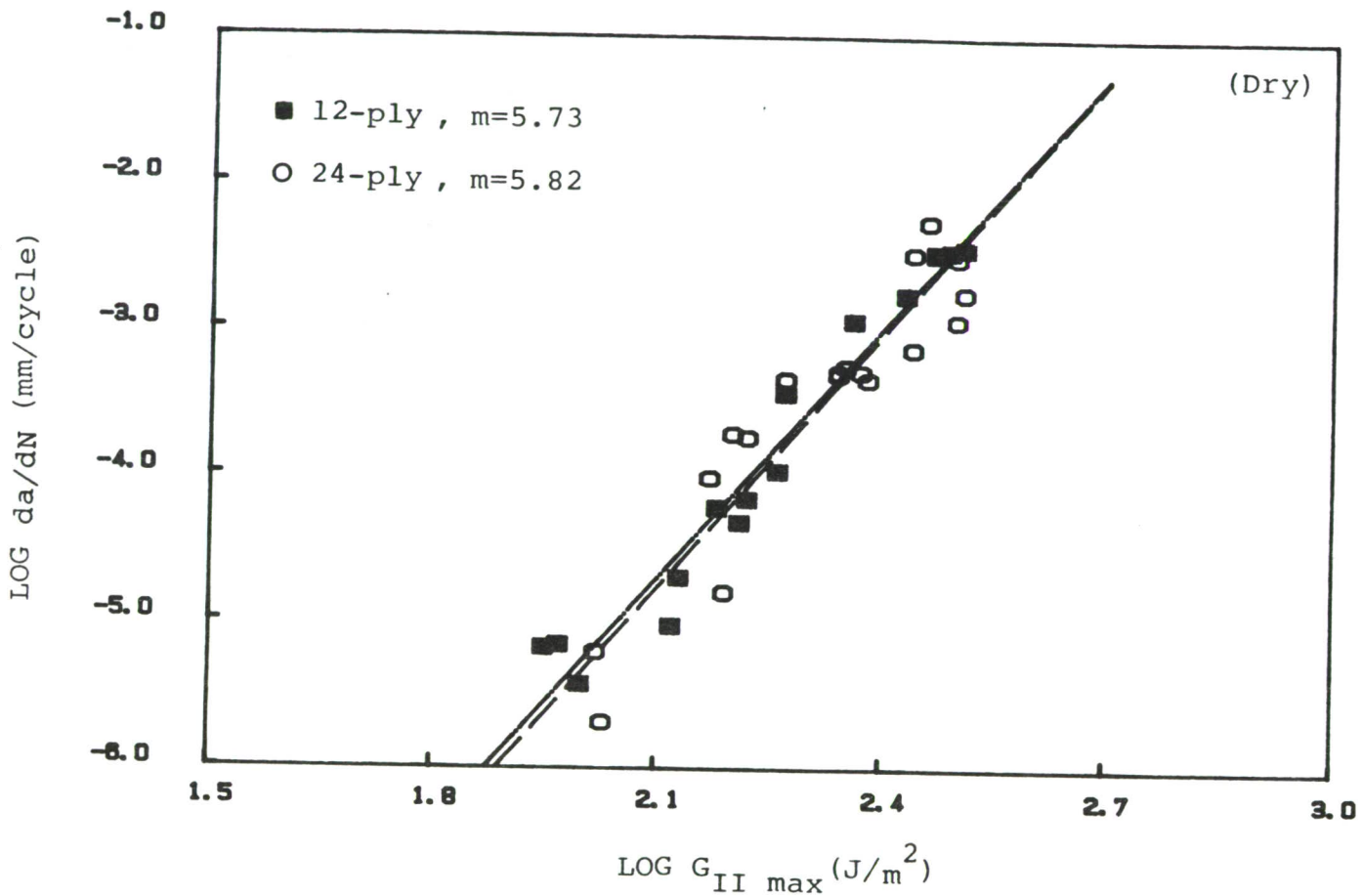

Figure 30. Effect of Laminate Thickness on Mode II Fatigue Crack Growth (V_p=.5%).

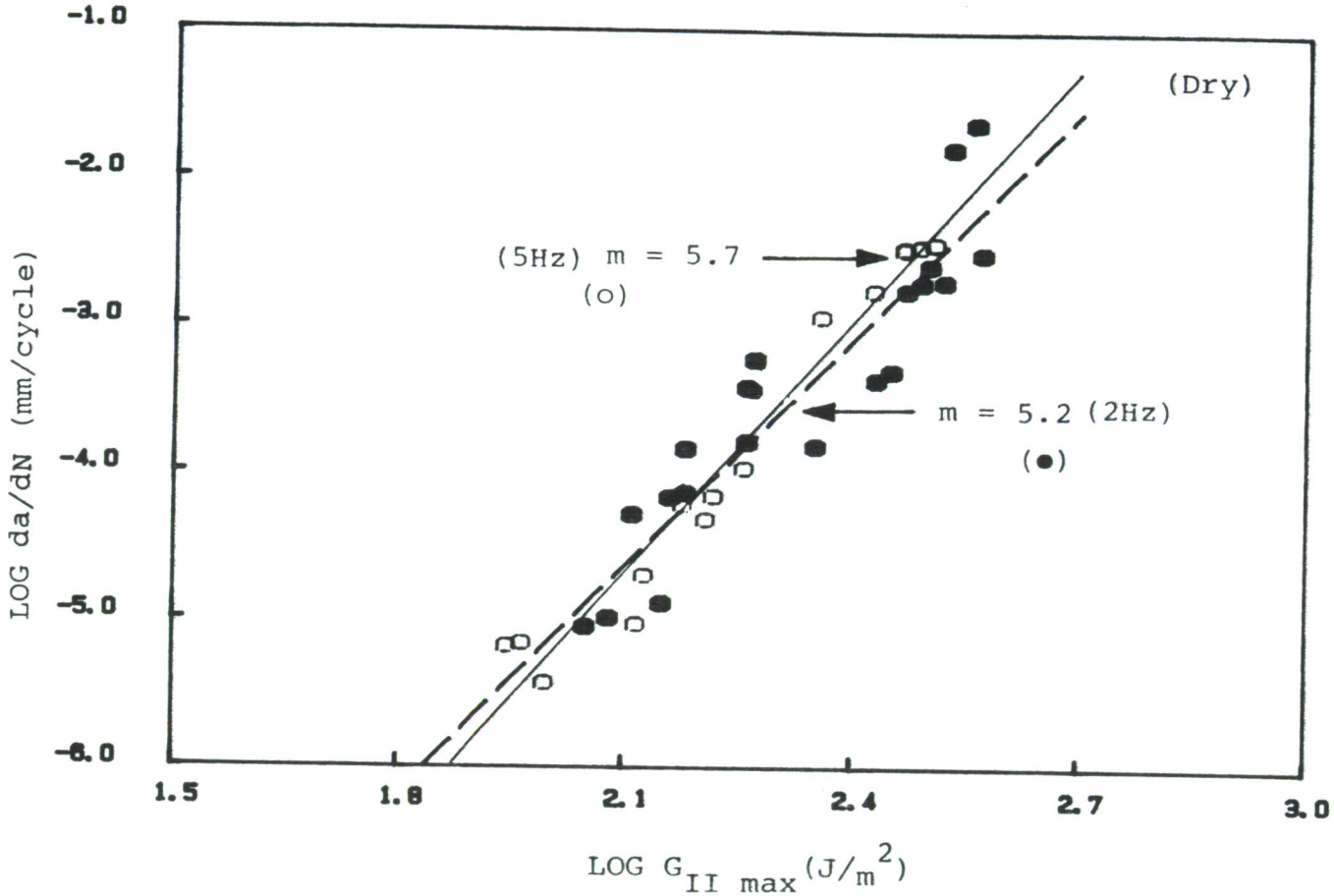

Figure 31. Effect of Frequency on Mode II Fatigue Crack Growth (V_p=.5%).

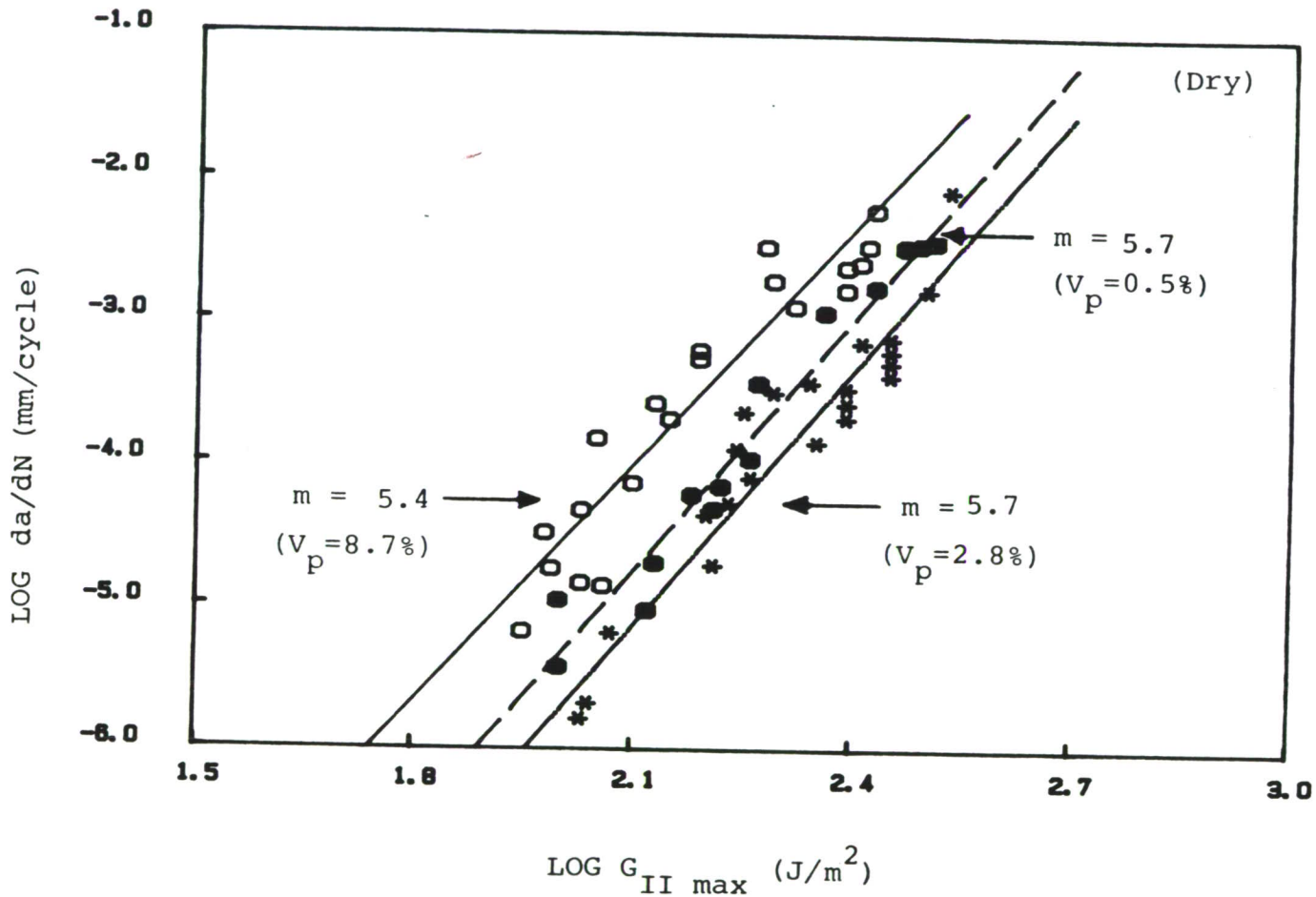

Figure 32. Effect of Porosity Level on Mode II Fatigue Crack Growth.

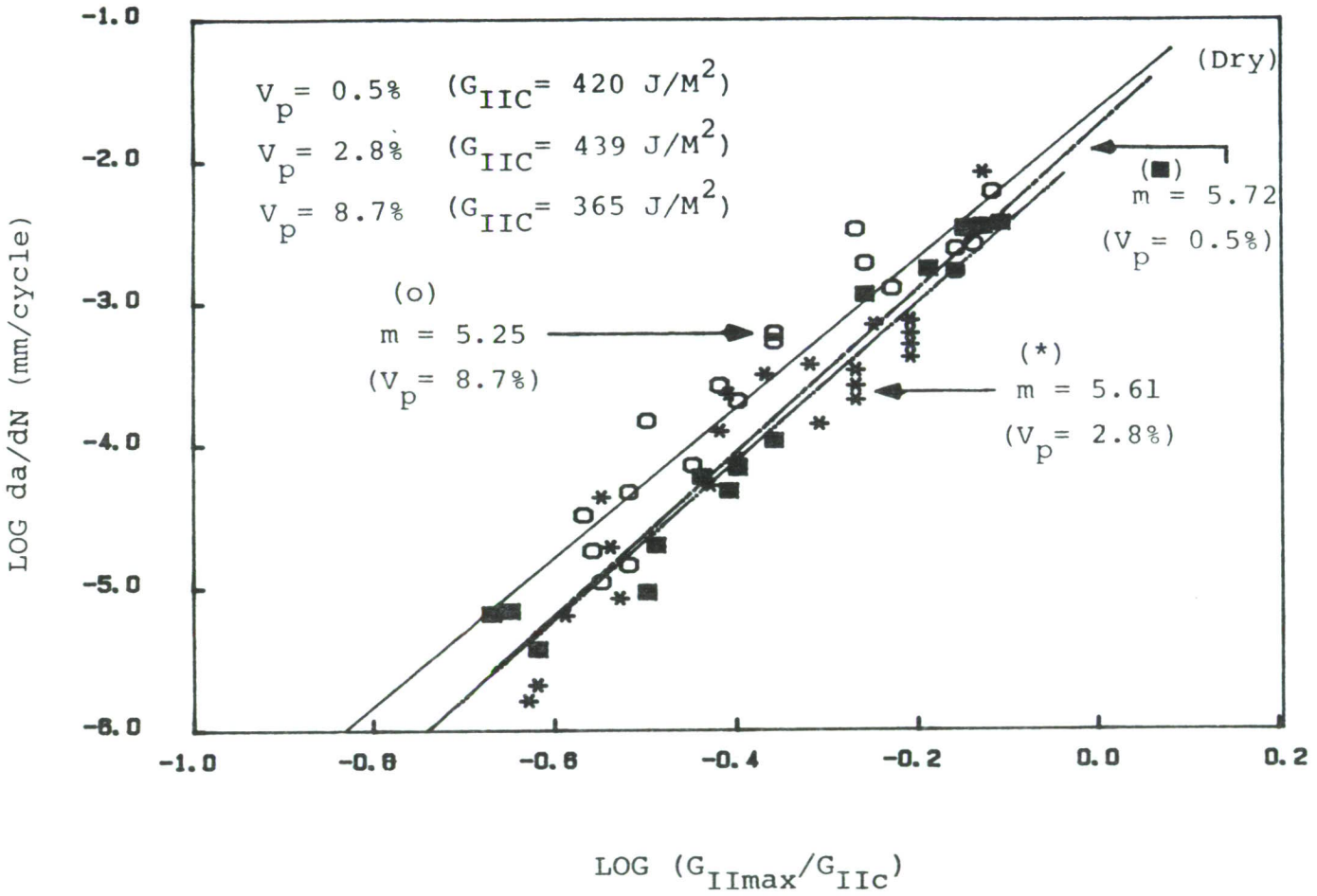

Figure 33. Data from Figure 32 Normalized by G_{IIc}.

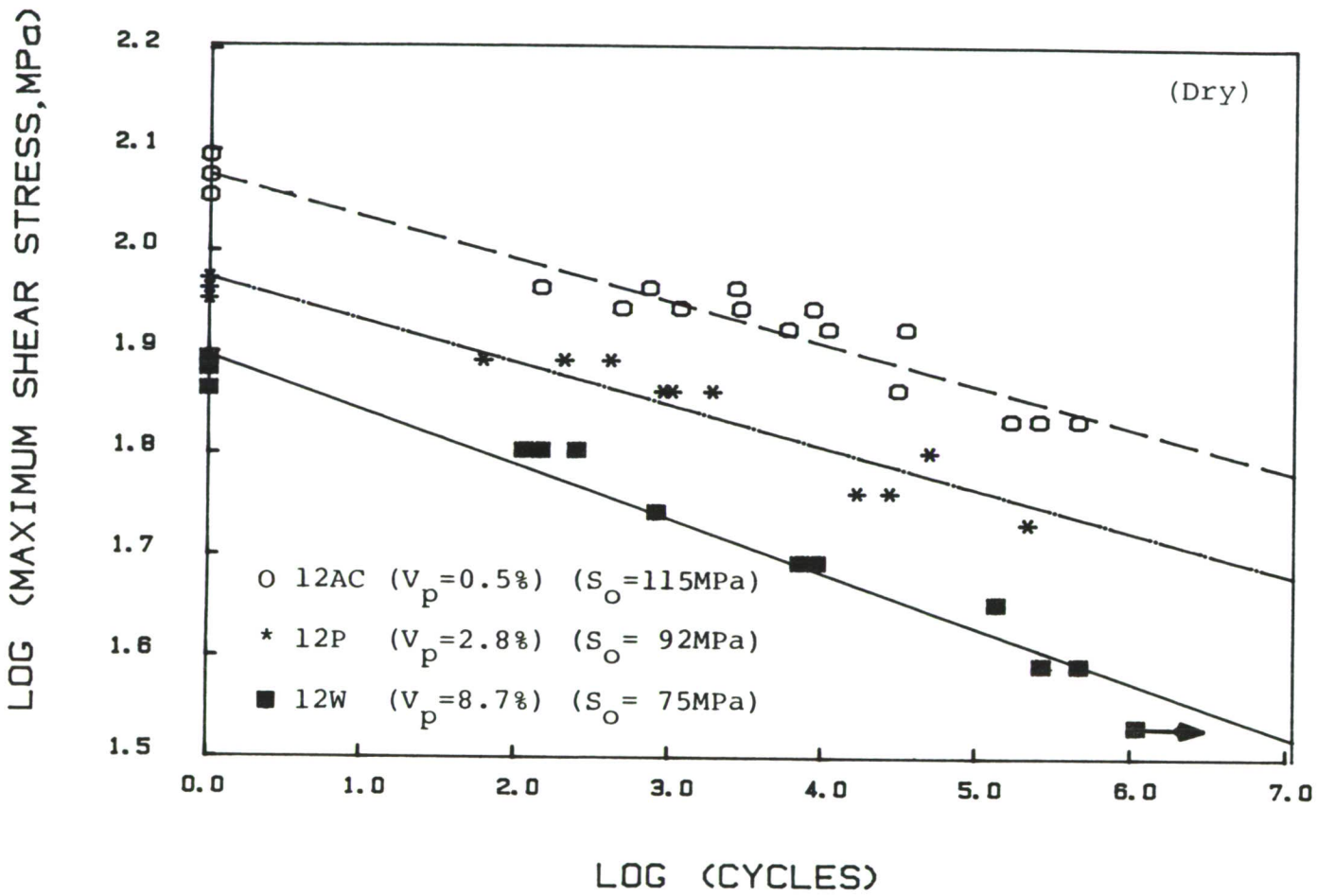

Figure 34. Log-Log Plot of Short Beam Fatigue S-N Data from Figure 21.

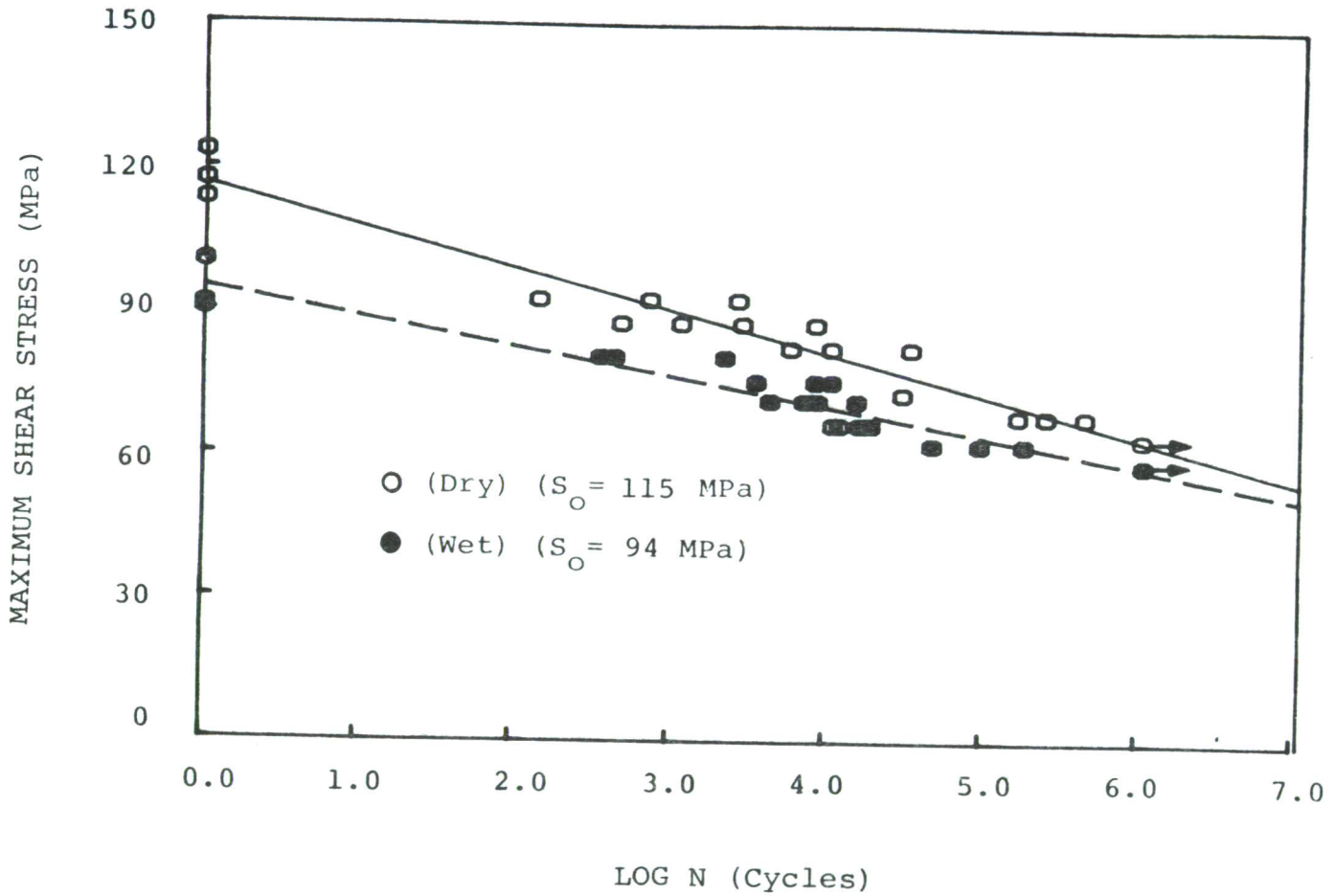

Figure 35. Low Porosity Wet vs. Dry Short Beam Fatigue S-N Data, V_p=0.5%.

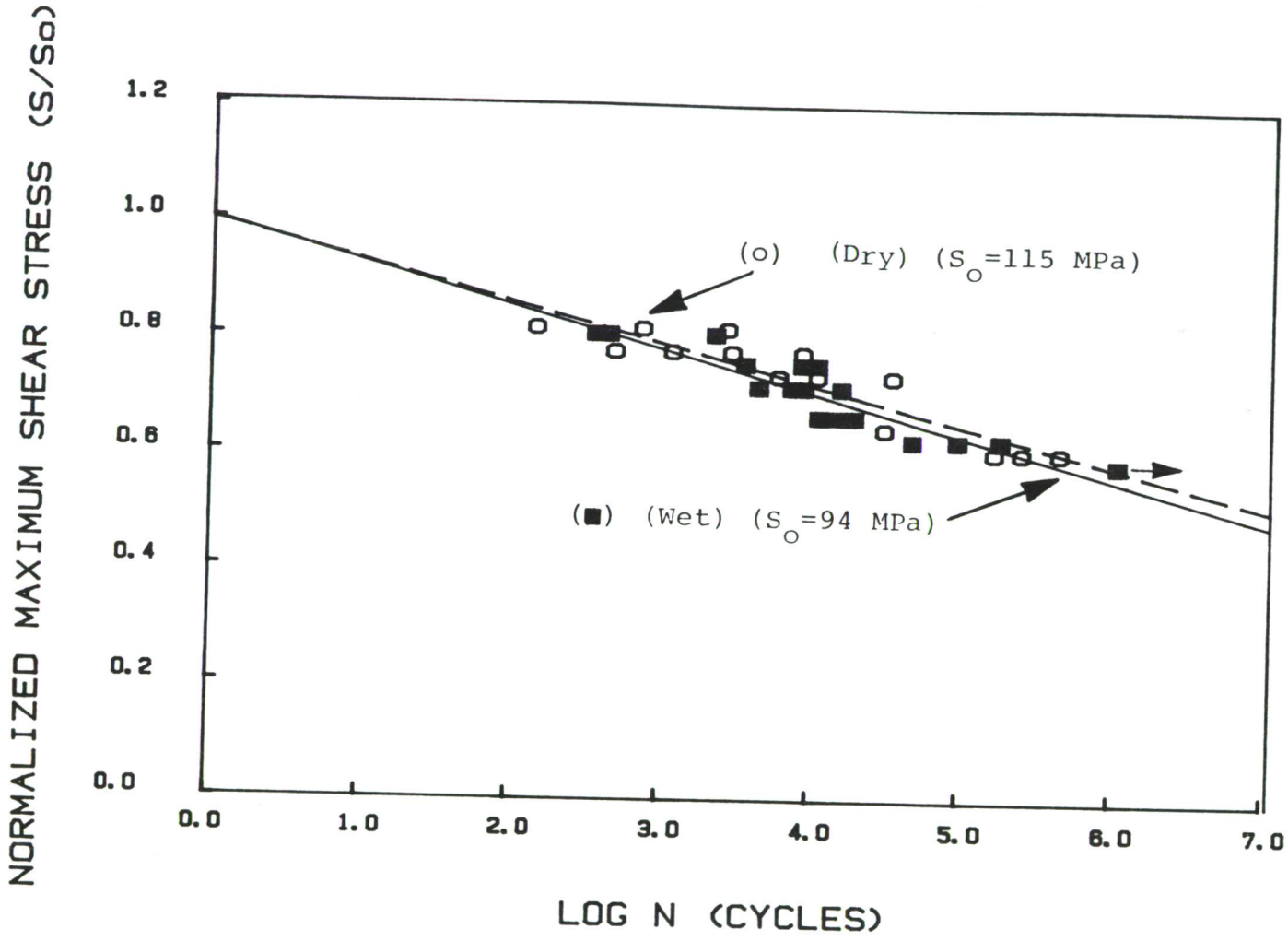

Figure 36. Normalized Low Porosity Data from Figure 35 (forced through $S/S_o=1.0$).

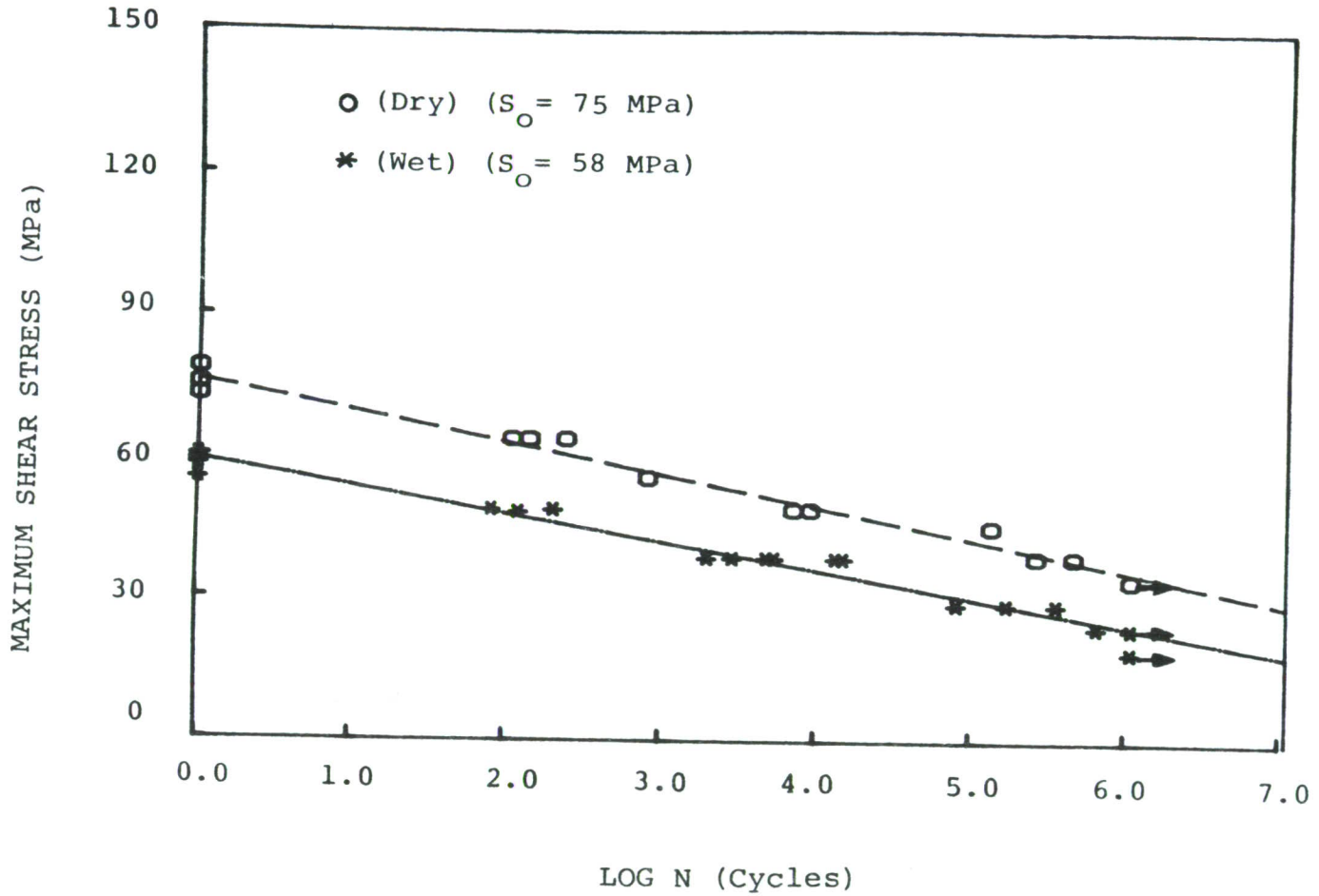

Figure 37. High Porosity Wet vs. Dry Short Beam Fatigue S-N Data, V_p=8.7%.

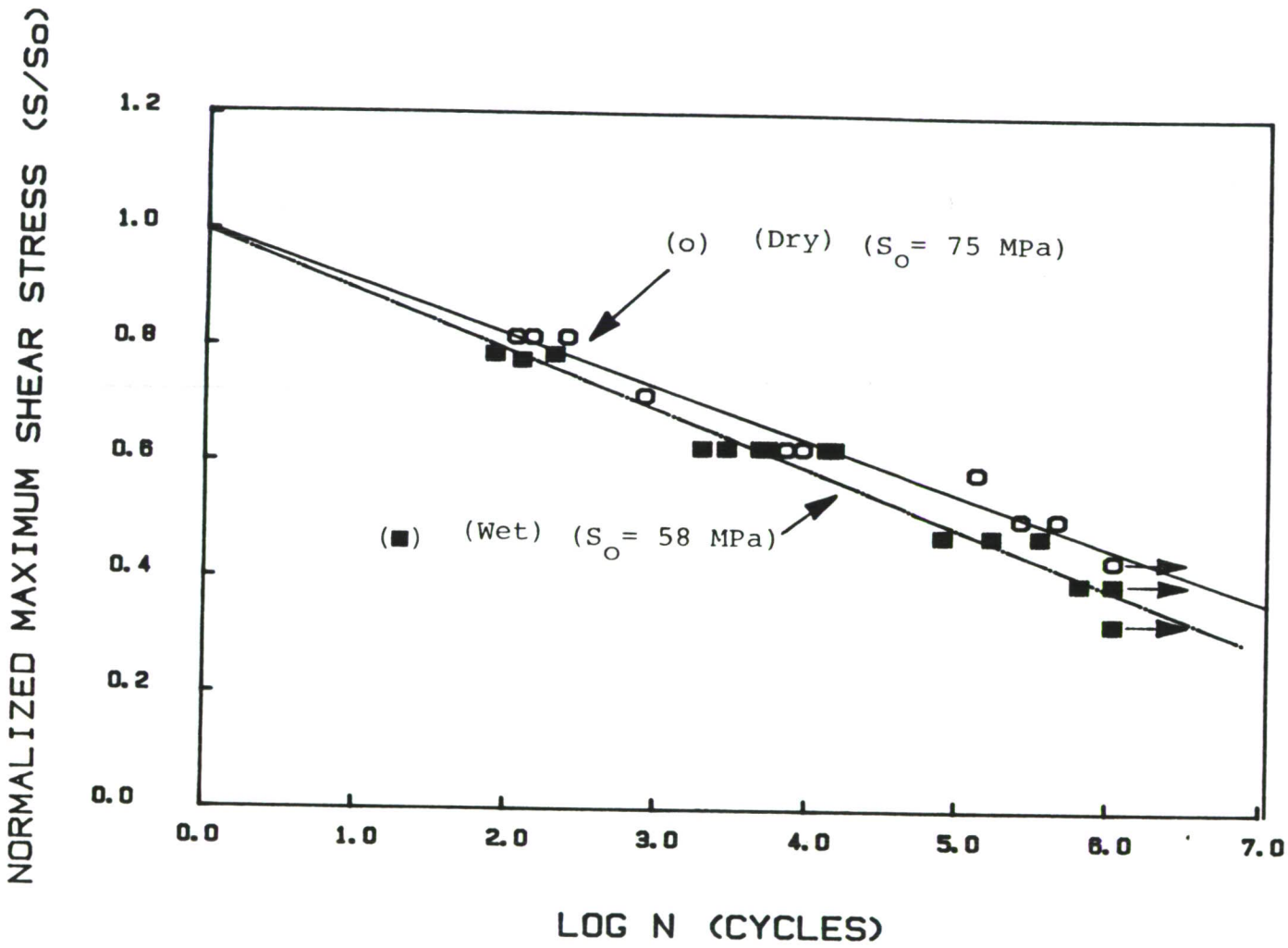

Figure 38. Normalized High Porosity Data from Figure 37 (forced through $S/S_o=1.0$).

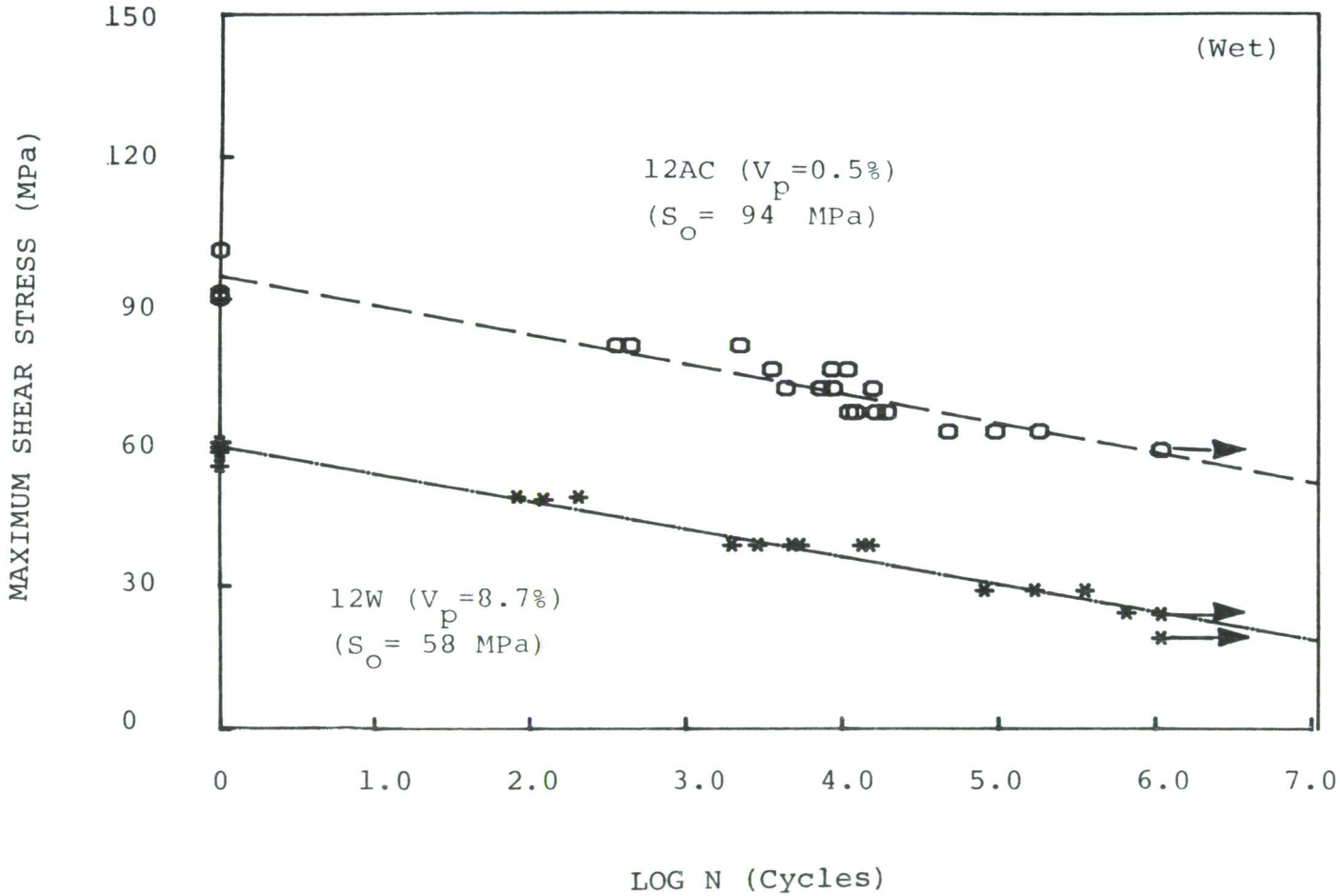

Figure 39. High vs. Low Porosity Wet Short Beam Fatigue Data.

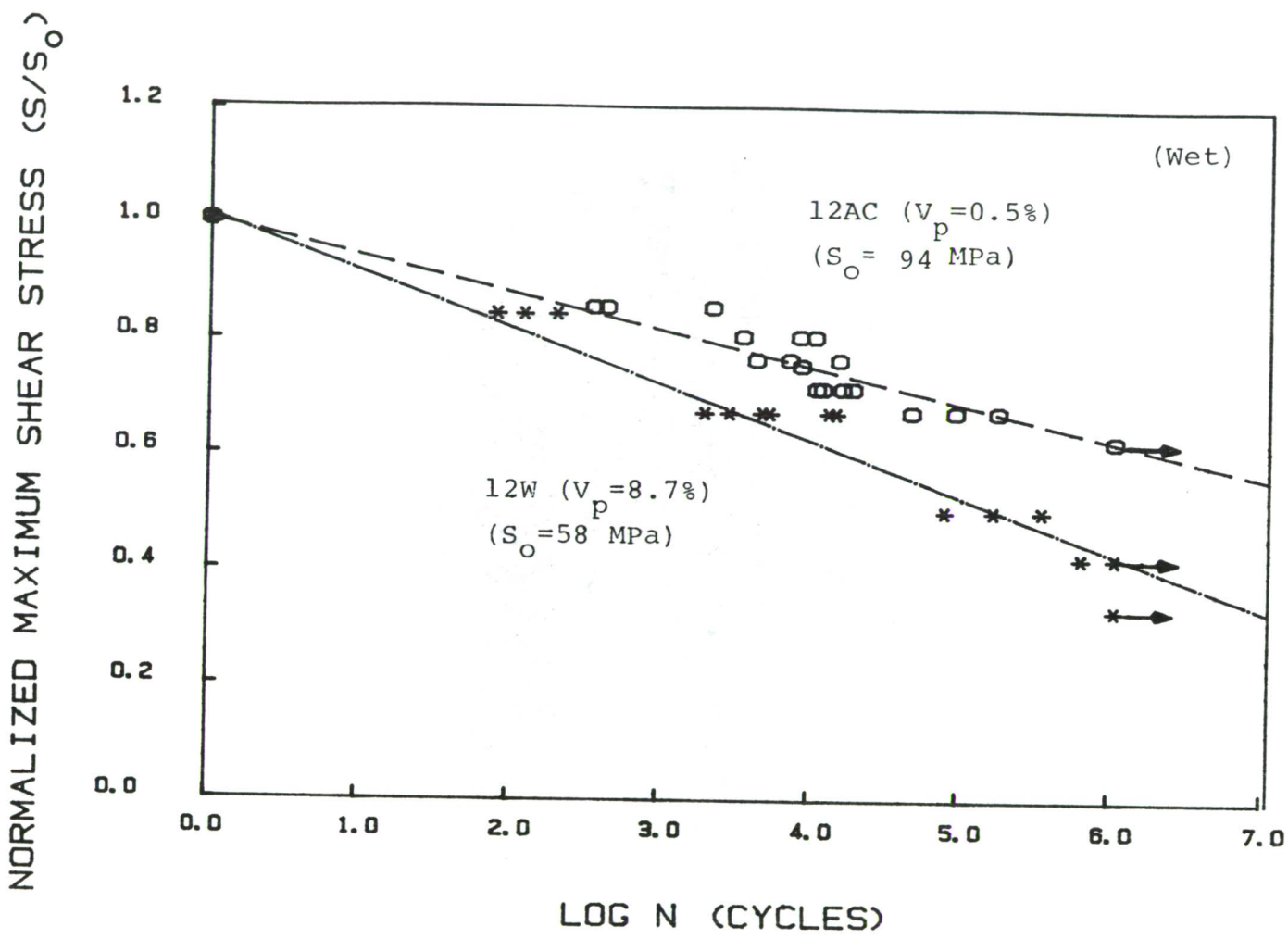

Figure 40. Normalized High vs. Low Porosity Data from Figure 39 (forced through $S/S_o=1.0$).

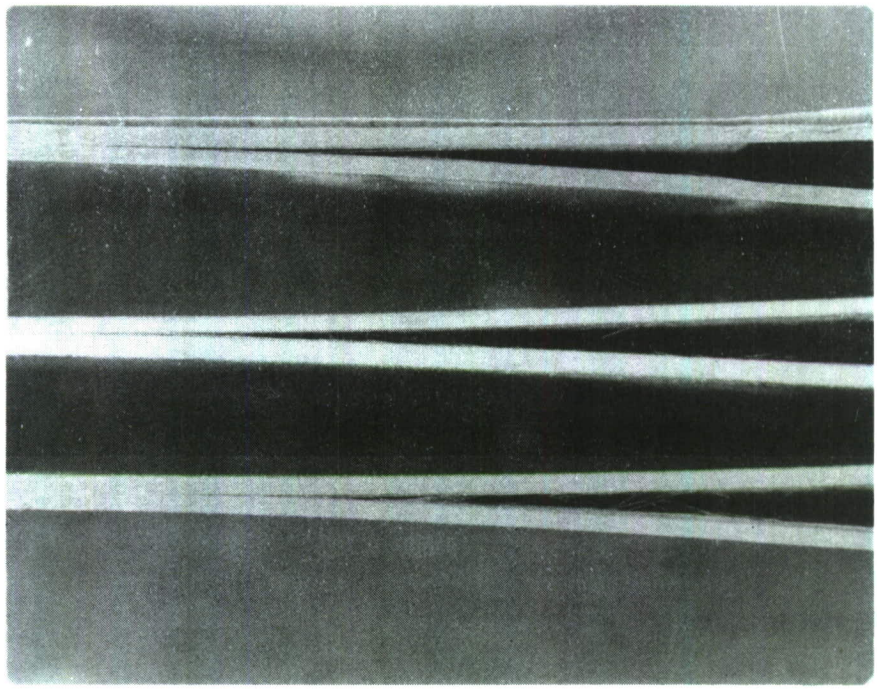

Figure 41. Comparison of Mode I Fiber Bridging in 0.5% Porosity Material: Static Dry (Top); Static Wet(Bottom); and Low G_{Imax} Wet Fatigue (Middle).

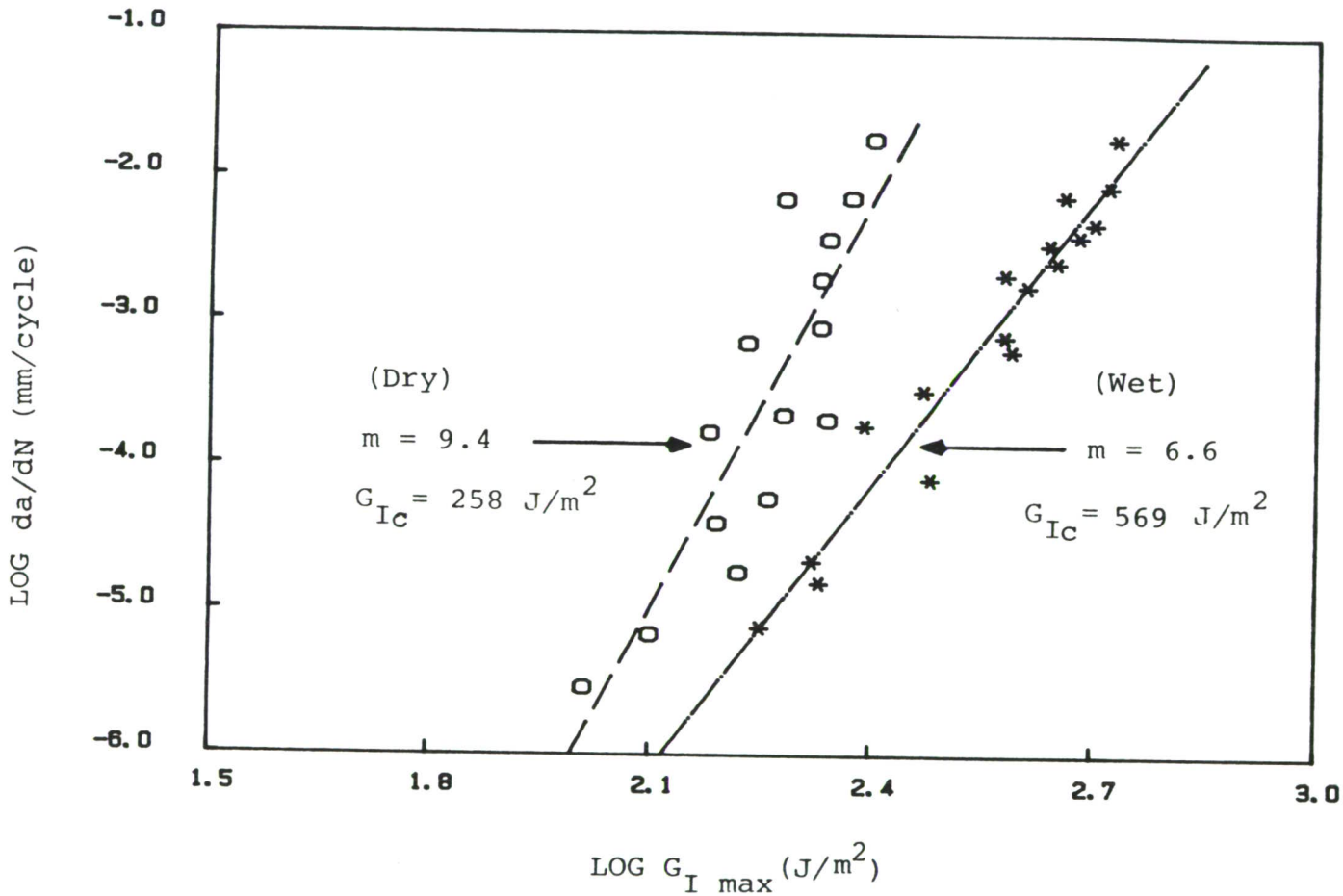

Figure 42. Low Porosity Wet vs. Dry Mode I Fatigue Crack Growth Data, V_p=0.5%.

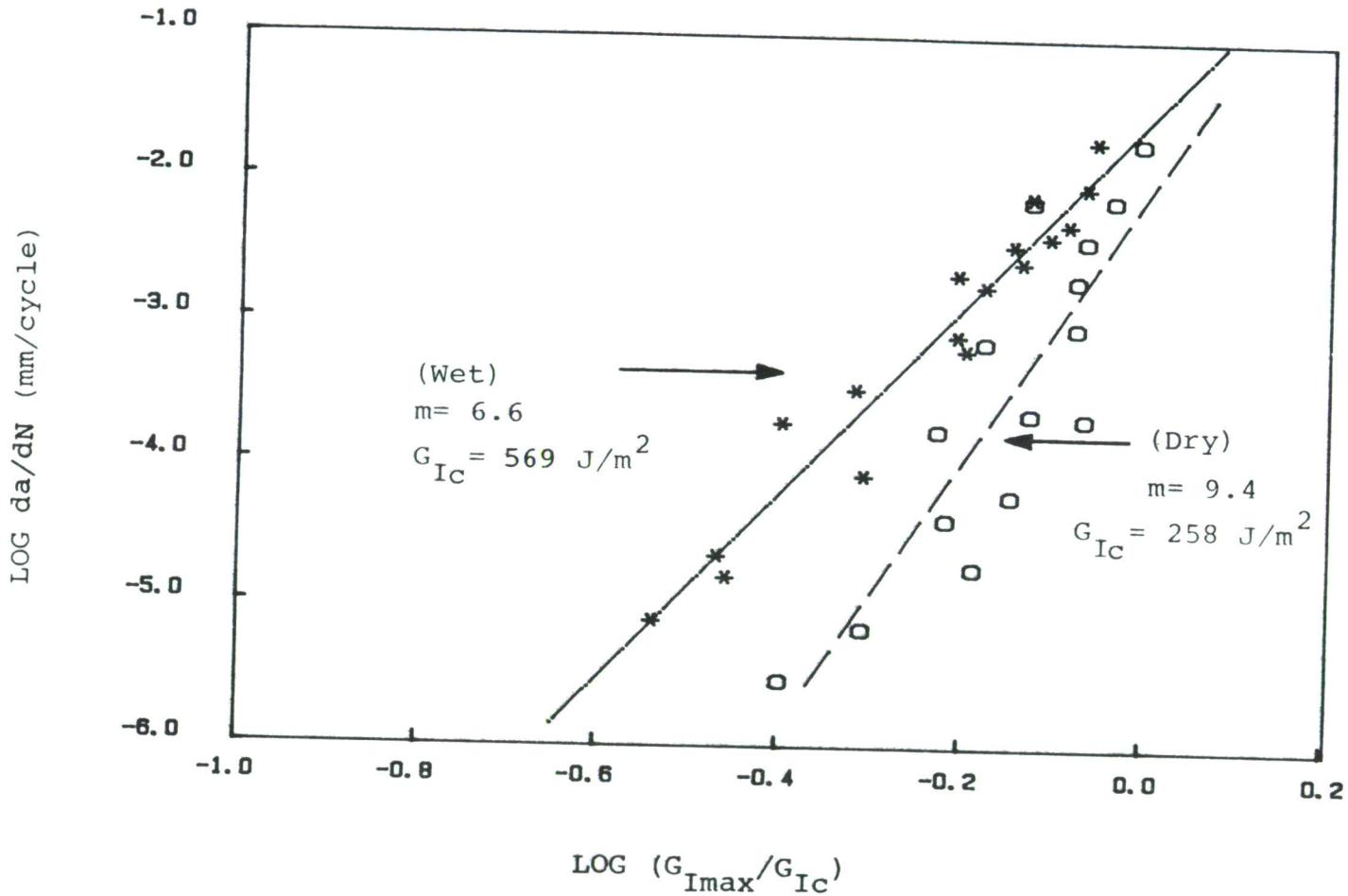

Figure 43. Normalized Low Porosity Wet vs. Dry Mode I Fatigue Crack Growth Data, V_p=.5%.

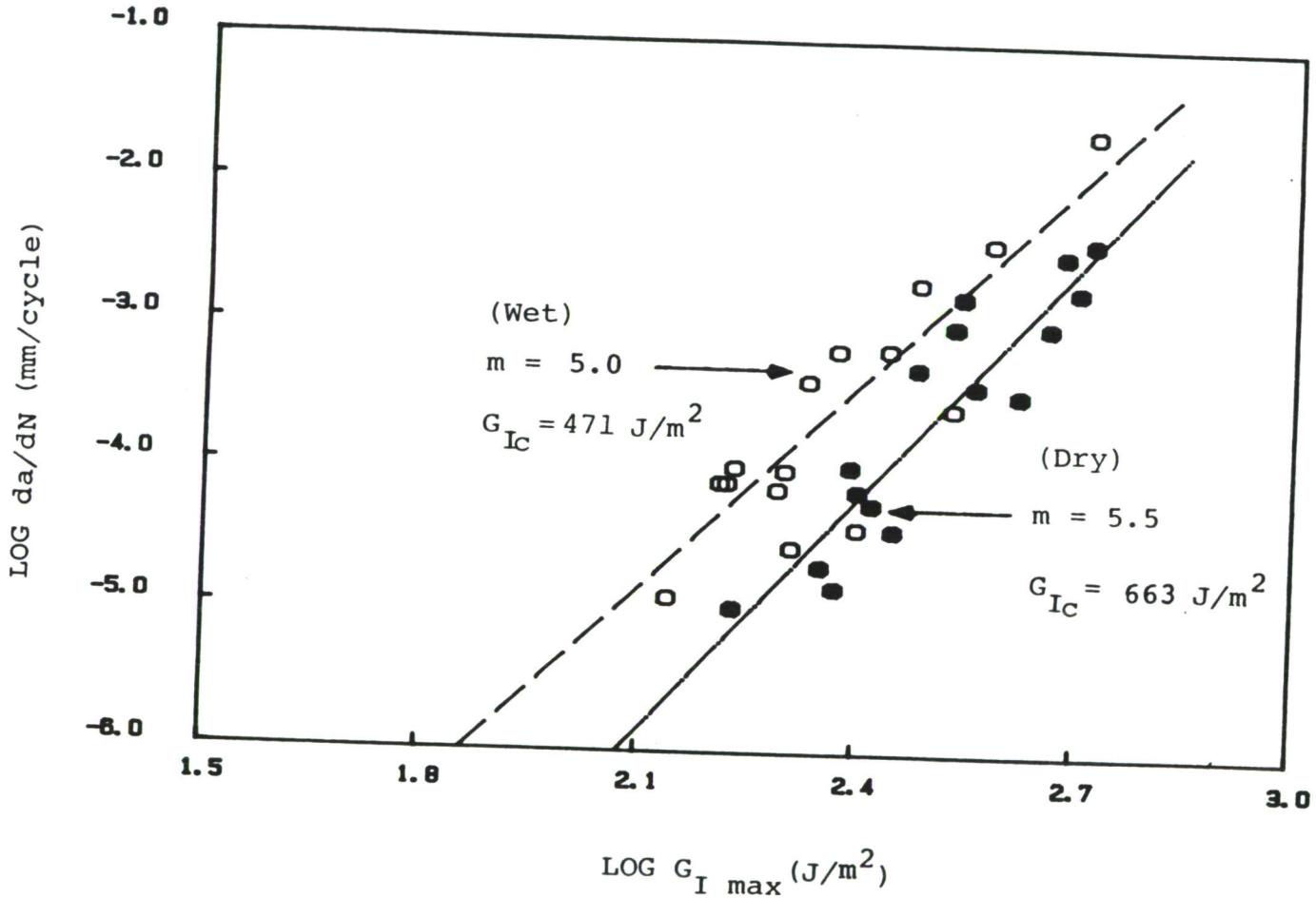

Figure 44. High Porosity Wet vs. Dry Mode I Fatigue Crack Growth Data, V_p=8.7%.

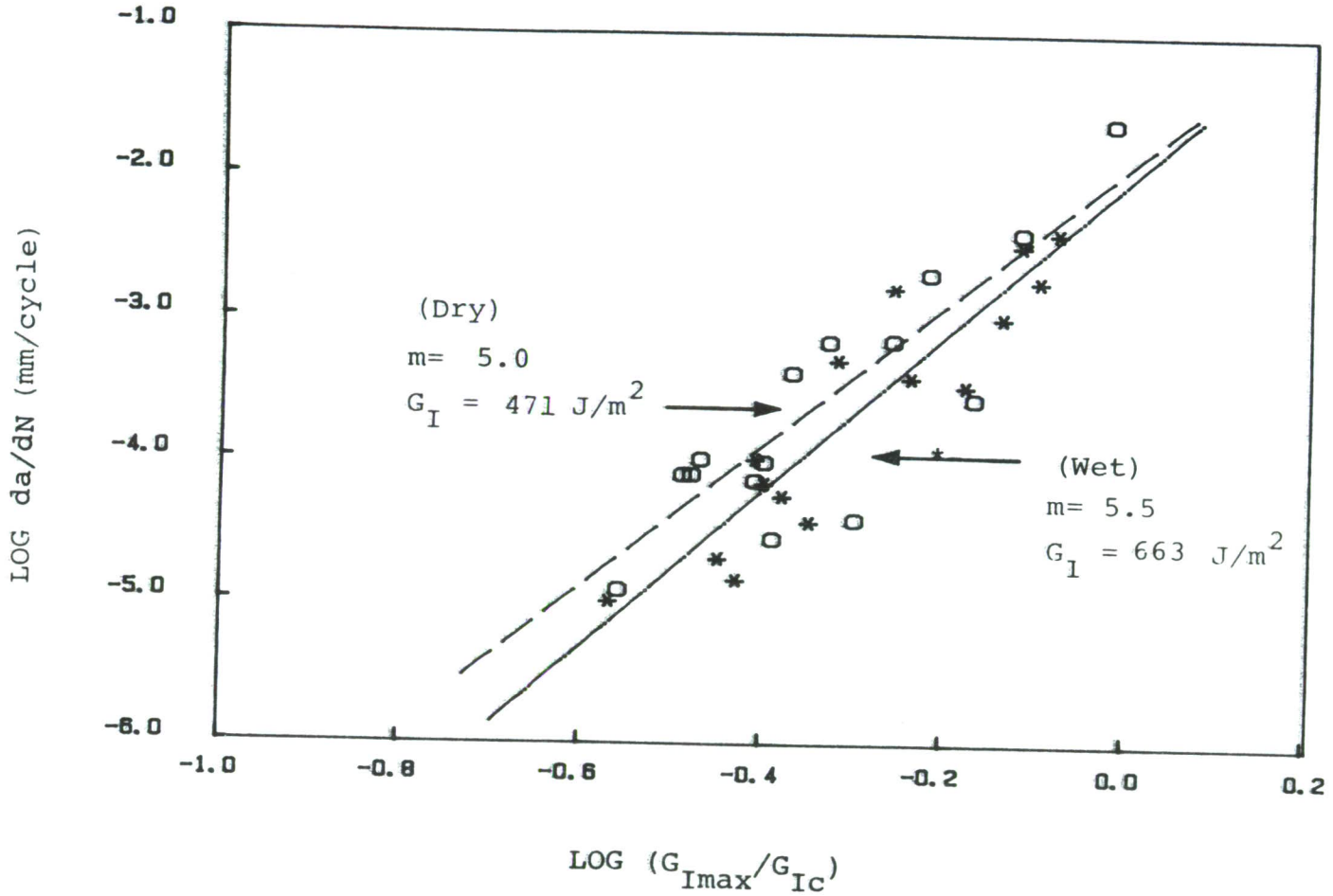

Figure 45. Normalized High Porosity Wet vs. Dry Mode I Fatigue Crack Growth Data, V_p=8.7%.

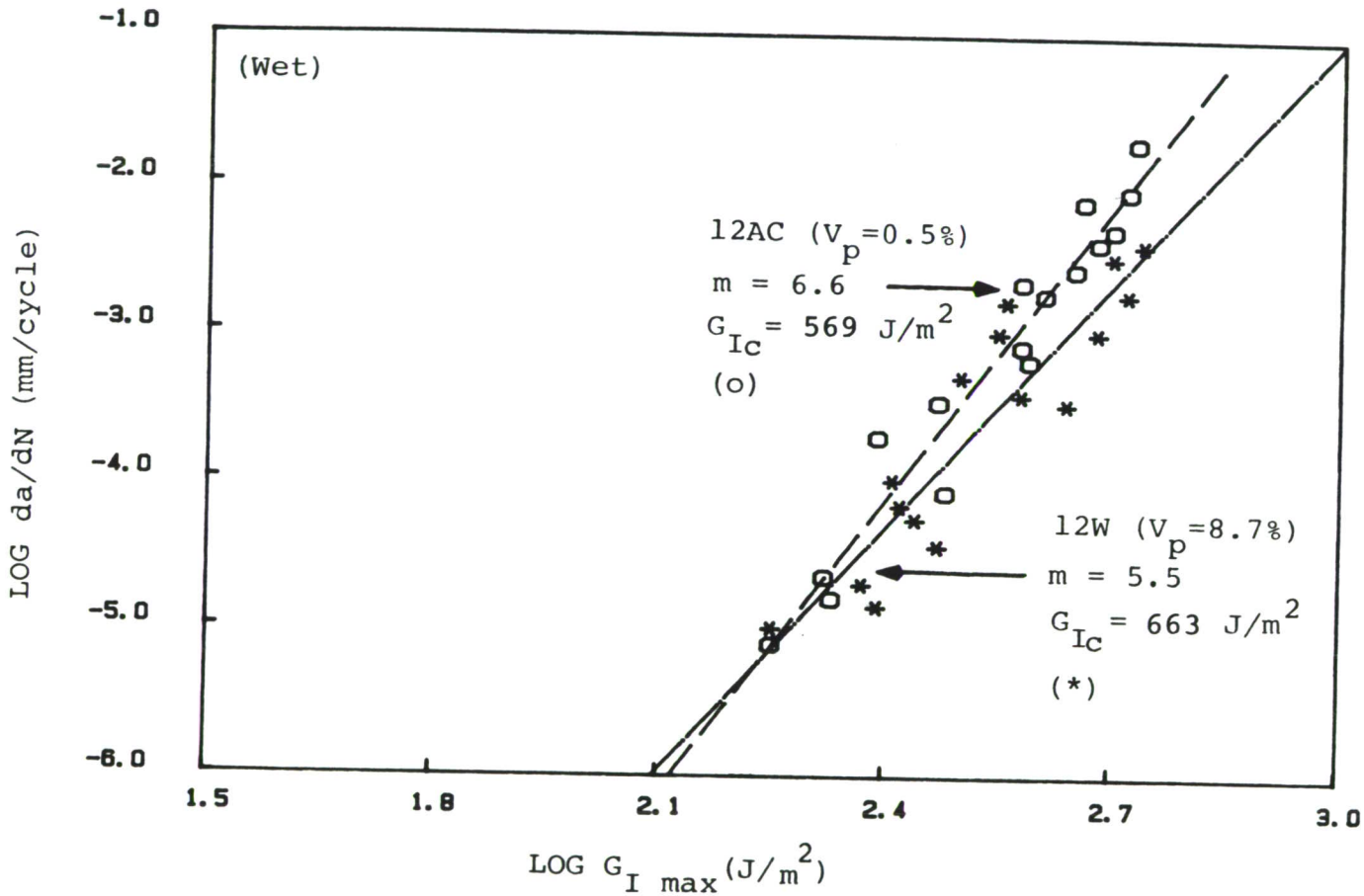

Figure 46. High vs. Low Porosity Mode I Wet Fatigue Crack Growth Data.

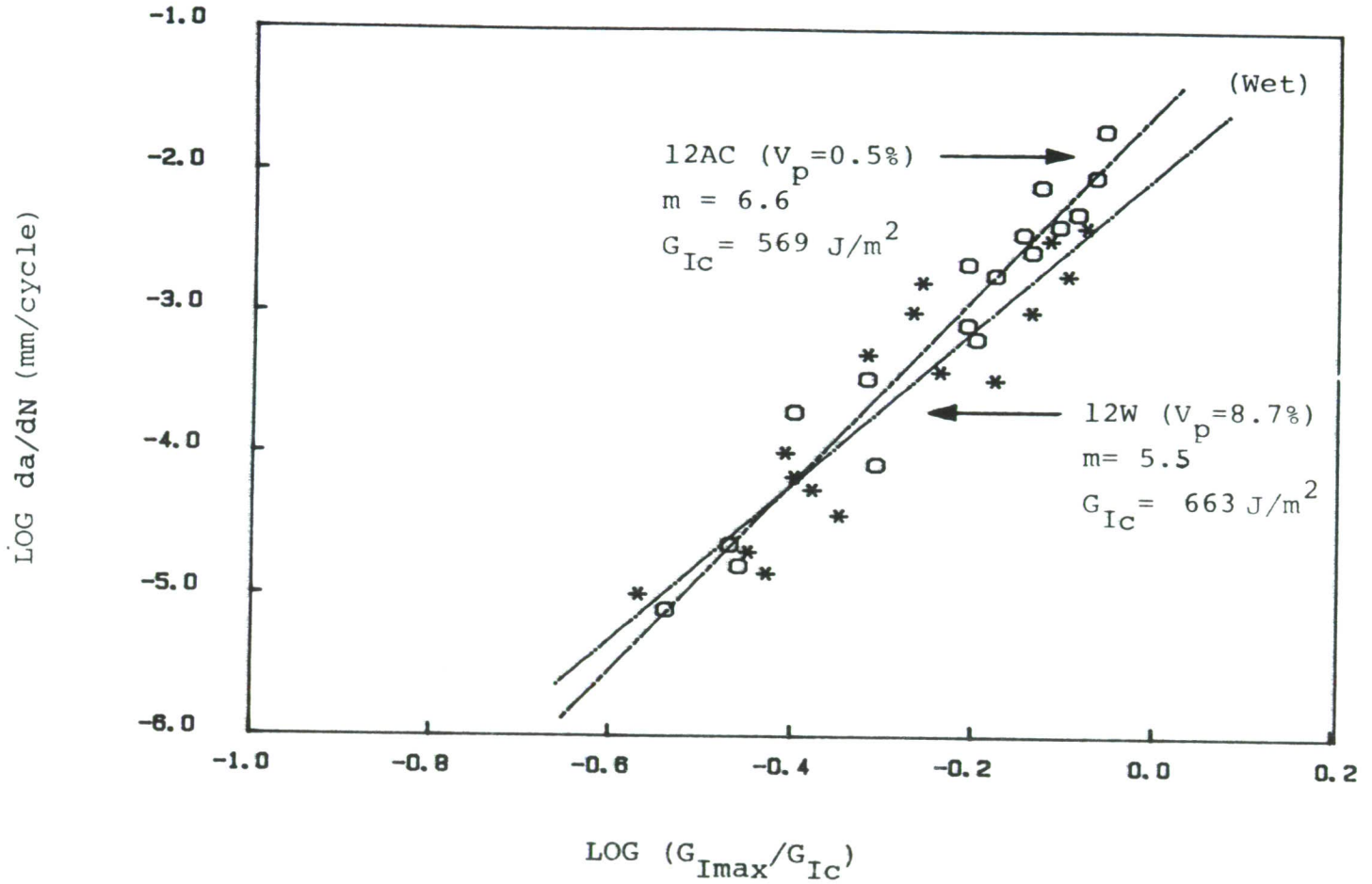

Figure 47. Normalized High vs. Low Mode I Wet Fatigue Crack Growth Data.

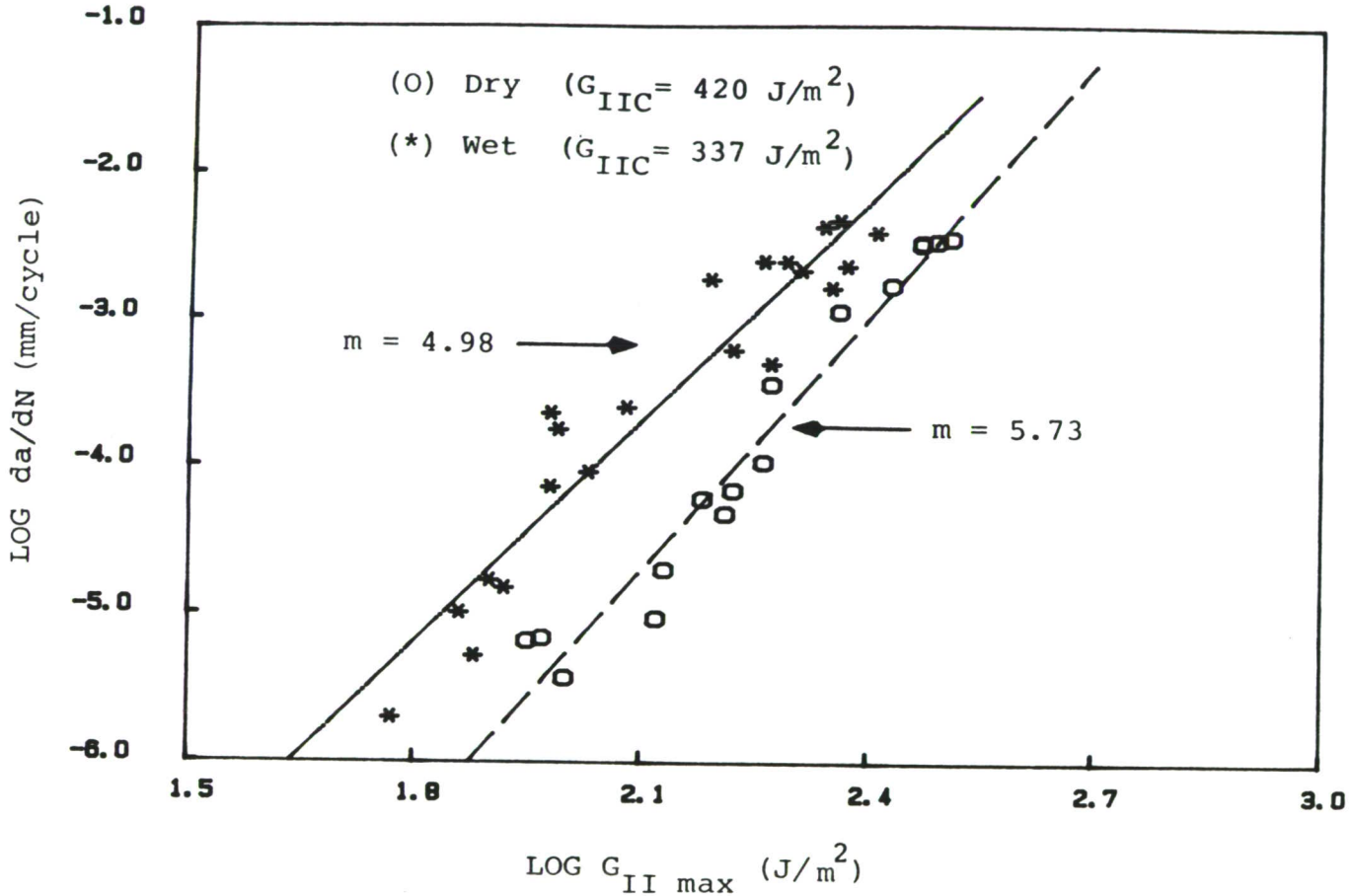

Figure 48. Low Porosity Wet vs. Dry Mode II Fatigue Crack Growth Data (V_p=0.5%).

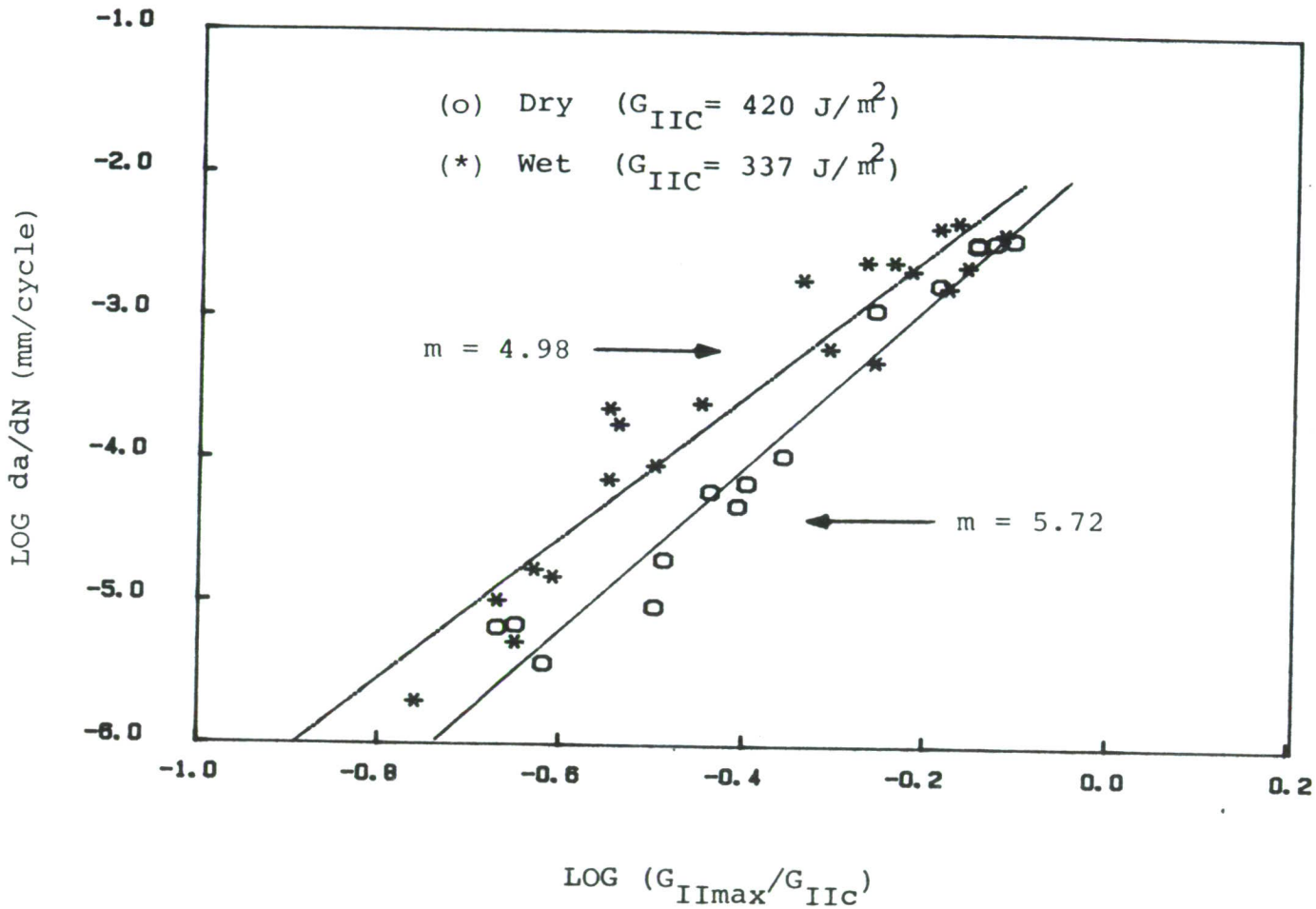

Figure 49. Normalized Low Porosity Wet vs. Dry Mode II Fatigue Crack Growth Data (V_p=0.5%).

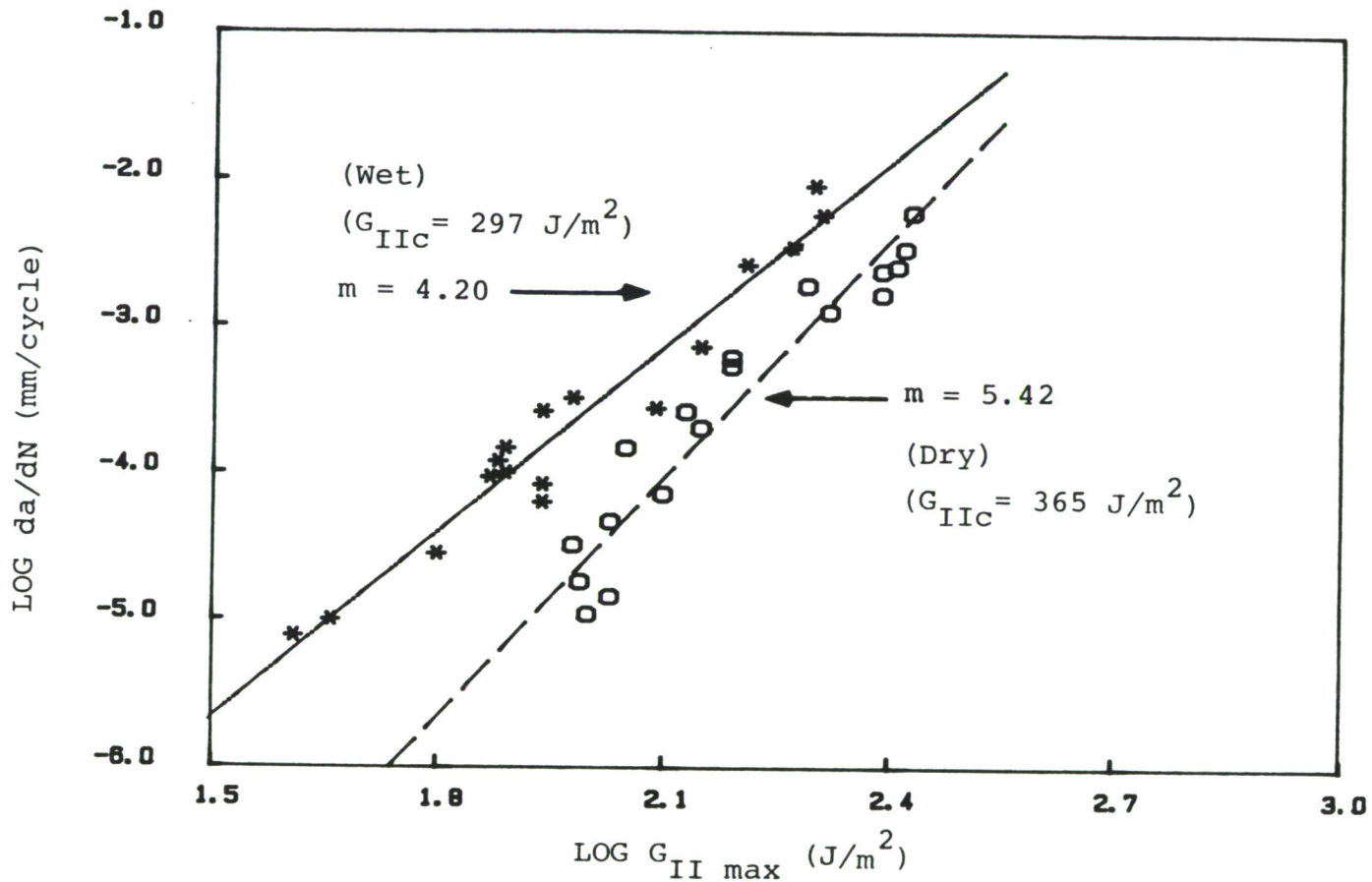

Figure 50. High Porosity Wet vs. Dry Mode II Fatigue Crack Growth Data (V_p=8.7%).

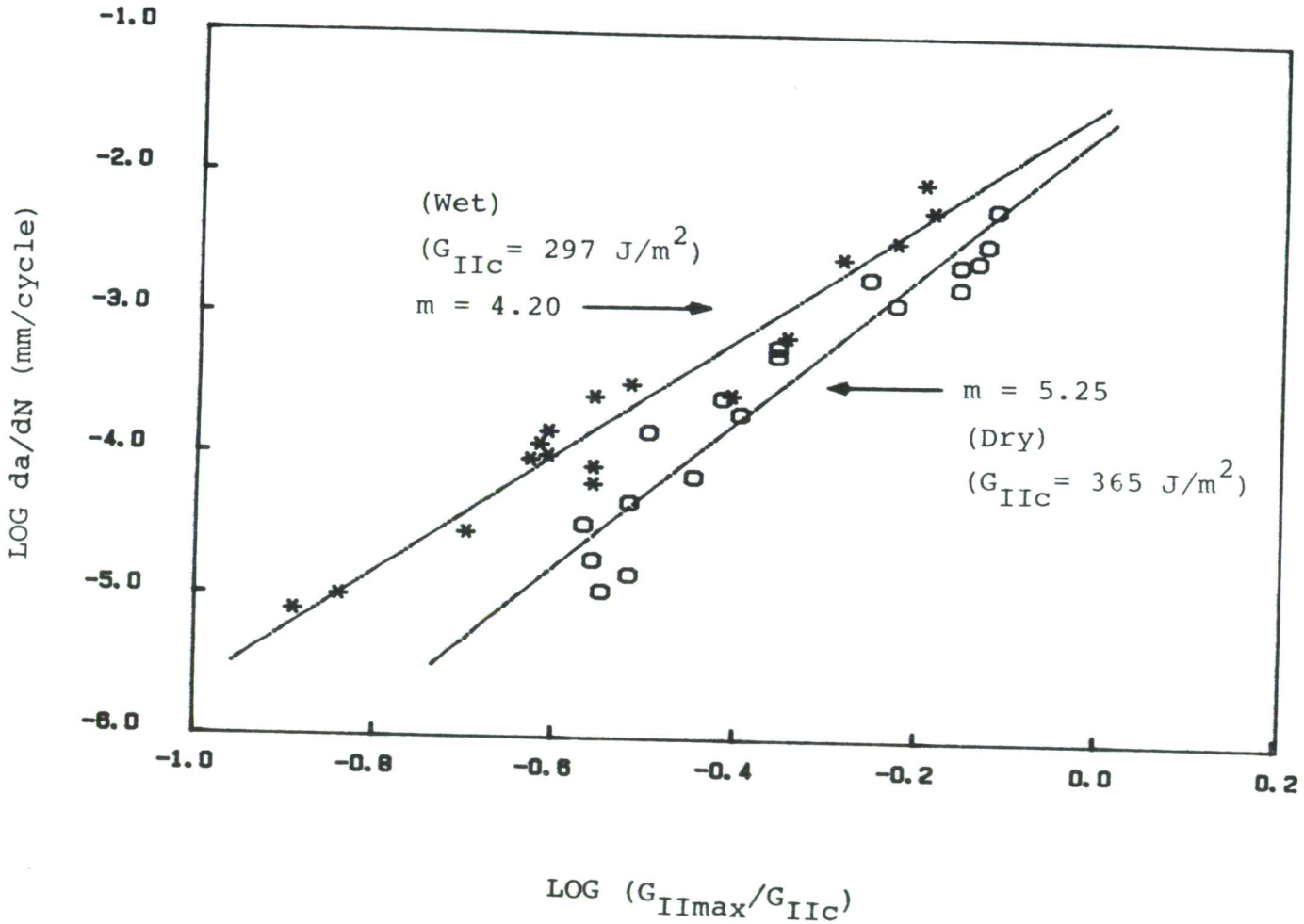

Figure 51. Normalized High Porosity Wet vs. Dry Mode II Fatigue Crack Growth Data (V_p=8.7%).

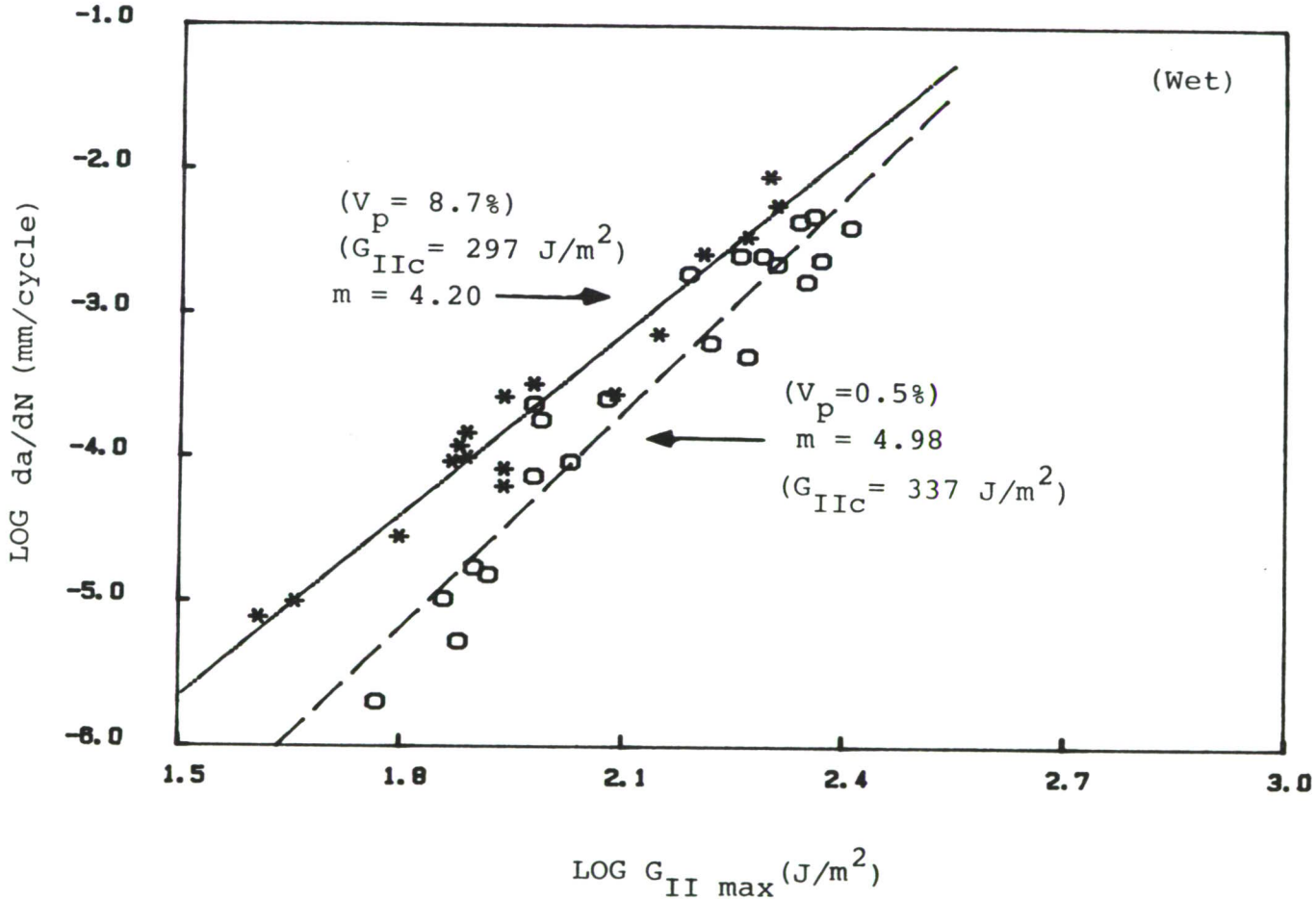

Figure 52. High vs. Low Porosity Mode II Wet Fatigue Crack Growth Data.

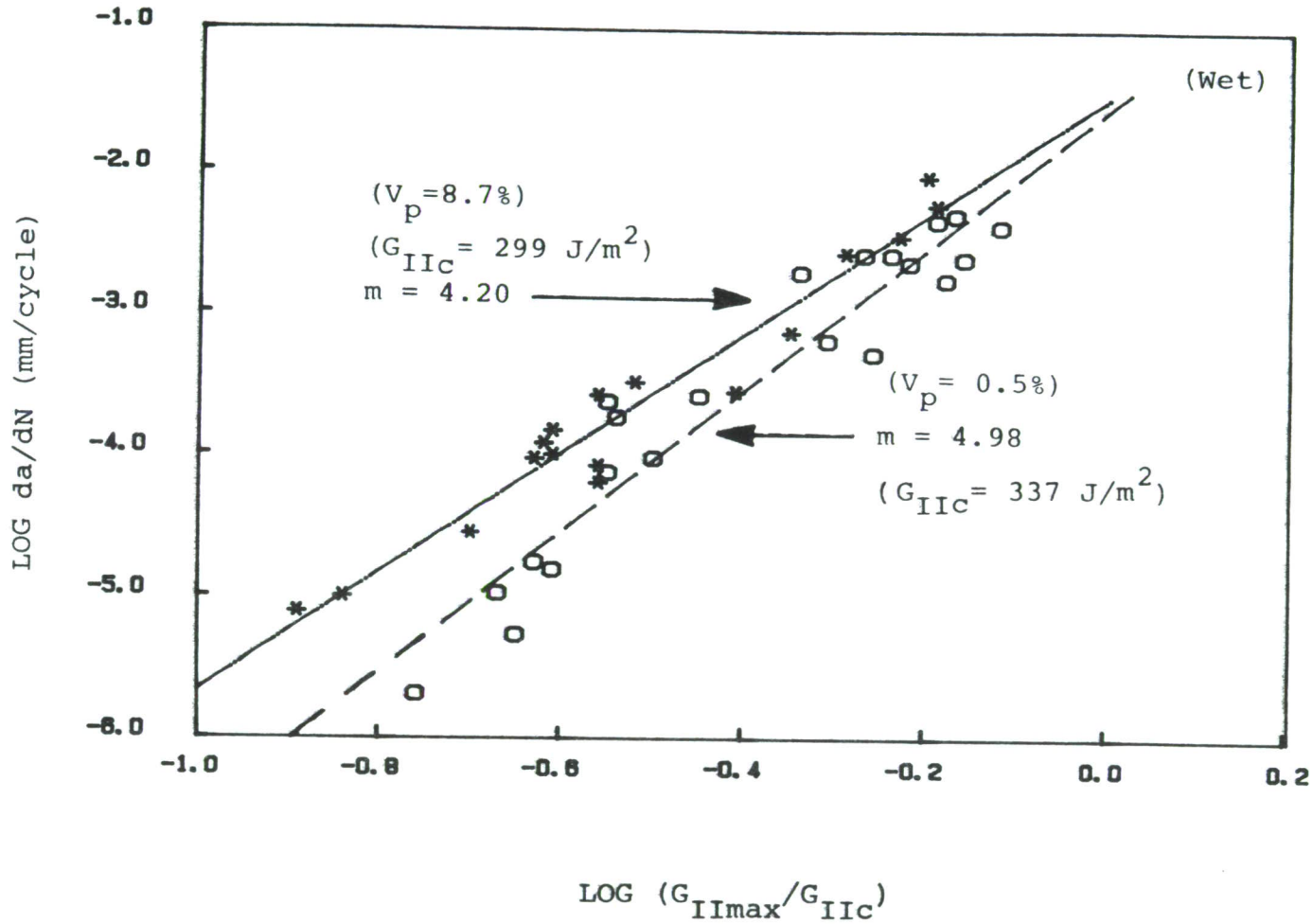

Figure 53. Normalized High vs. Low Porosity Mode II Wet Fatigue Crack Growth Data.

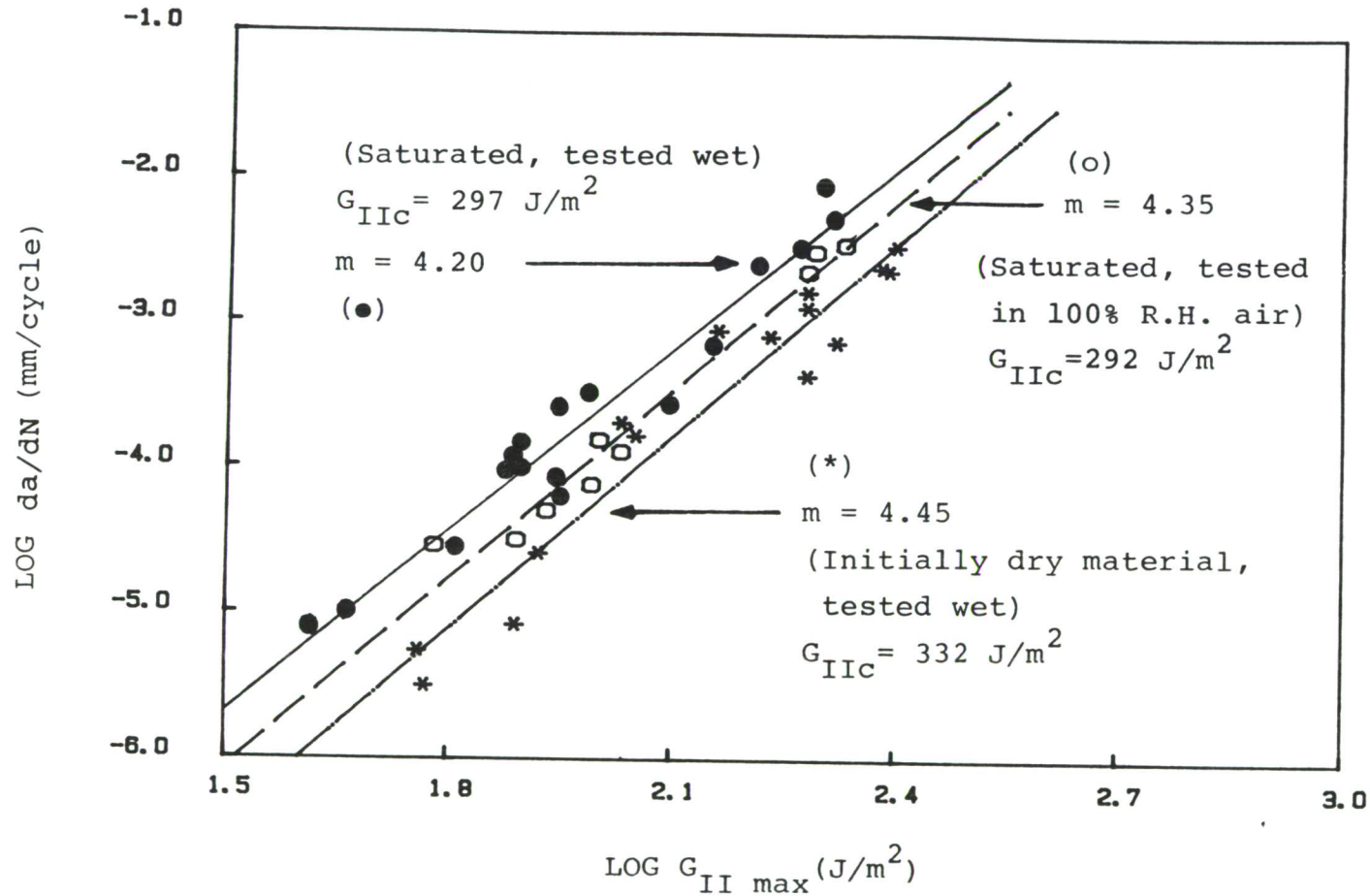

Figure 54. Comparison of Conditioned and Tested Wet Data with Conditioned Wet Material Tested at 100% R.H. and Dry (Ambient) Material Tested Wet, Mode II Fatigue Crack Growth, V_p=8.7%.

APPENDIX

ORIGINAL DATA AND CALCULATIONS

Appendix 1. Moisture Weight Gain and Loss

No. of Plies	Specimen I.D.	Porosity Content	Weight at 7/27	8/26	9/2	9/8	9/16	9/29	10/5	10/16	11/4	4/7/87	5/1	6/1	Weight Change
8	81	< .5%	5.827	5.897	5.919	5.915	5.915	5.920	5.916			5.922	5.935	5.920	1.5
	82		5.915	5.980	5.984	5.998	5.990	5.995	5.998			5.996	6.00	5.990	1.3
12	12A1	< .5%	9.856	10.055	10.020	10.050	10.020	10.017	10.010			10.036	10.028	10.018	1.7
	12A3		10.417	10.561	10.561	10.588	10.575	10.579	10.574			10.586	10.578	10.575	1.5
	12C3		9.694	9.805	9.805	9.822	9.815	9.828	9.817	9.815					1.3
	12C4		9.814	9.958	9.950	9.966	9.967								1.5
	C22		8.191	8.313	8.324	8.325	8.316	8.327	8.317			8.326	8.331	8.327	1.5
	C24		8.247	8.393	8.388	8.389	8.389	8.398	8.391			8.410	8.400	8.404	1.7
	12W2	1.5%	7.866	8.032	8.000	8.011	8.008	8.028	8.018						1.8
	12W4		7.969	8.138	8.112	8.130	8.124	8.140	8.131			8.151	8.154	8.143	1.9
24	241	< .5%	18.824	19.017	19.038	19.053	19.038	19.108	19.115	19.126	19.138	19.200	19.200	19.187	1.9
	243		20.312	20.484	20.505	20.517	20.542	20.577	20.586	20.60	20.615	20.677	20.683	20.667	1.8

* All the specimens were conditioned in deionied water at 75 C for one month, and thern left in deionized water at room temperature.

Weight Loss Data for AS4/3501-6 Laminates
(Dried at 100°C in a Vacuum Oven)

Specimen I.D.	Weight at Date (grams) 0	1	5	6	9	12	14	16	17	Weight Loss	Change (%)	Average (%)
12C0	9.2395	9.2209	9.2193	9.2181	9.2169	9.2170	9.2170	9.2169	9.2171	.022	-.238	-.248
12C38	9.8925	9.8754	9.8705	9.8691	9.8674	9.8668	9.8668	9.8673	9.8669	.026	-.257	
12P3	8.2591	8.2539	8.2527	8.2522	8.2512	8.2512	8.2515	8.2517	8.2515	.018	-.213	-.202
12P5	8.4686	8.4584	8.4555	8.4547	8.4531	8.4524	8.4527	8.4528	8.4529	.016	-.190	
12W11	6.0299	6.0203	6.0197	6.0191	6.0190	6.0190	6.0189	6.0190	6.0191	.011	-.180	-.183
12W6	8.0138	7.9906	7.9898	7.9890	7.9889	7.9887	7.9885	7.9889	7.9888	.015	-.186	
24C6	15.9427	15.9244	15.9189	15.9168	15.9156	15.9143	15.9138	15.9138	15.9141	.029	-.179	-.174
24C12	21.3282	21.3078	21.3021	21.2998	21.2979	21.2967	21.2959	21.2965	21.2966	.032	-.168	

Appendix 2. Pore Dimensions

Longitudinal Pore Dimensions For Various Porosity Levels Of AS4/3501-6 12-Ply Laminates

LAMINATE ID	L (μm)	D (μm)	L/D
12AC	8.8	7.5	1.2
	12.5	10.0	1.3
	17.5	12.5	1.4
	26.3	18.8	1.4
	7.5	5.0	1.5
	10.0	6.3	1.6
	13.8	6.3	2.2
	12.5	5.0	2.5
	16.3	6.3	2.6
	12.5	3.8	3.3
	25.0	6.3	4.0
AVE.	14.8	8.0	
STD.DEV.	6.1	4.3	

LAMINATE ID	L (μm)	D (μm)	L/D
12PRESS	8.8	8.8	1.0
	12.5	10.0	1.3
	11.3	6.3	1.8
	11.3	5.0	2.3
	10.0	3.8	2.7
	37.5	12.5	3.0
	16.3	5.0	3.3
	12.5	3.8	3.3
	93.8	20.0	4.7
	88.8	16.3	5.5
	113.8	18.8	6.1
	78.8	12.5	6.3
	87.5	8.8	10.0
	107.5	8.8	12.3
	56.3	3.8	15.0
	83.8	5.0	16.8
AVE.	51.9	9.3	
STD.DEV.	40.5	5.4	

LAMINATE ID	L (μm)	D (μm)	L/D
12W	8.8	18.8	0.5
	8.8	15.0	0.6
	6.3	8.8	0.7
	8.8	10.0	0.9
	5.0	5.0	1.0

	12.5	12.5	1.0
	7.5	7.5	1.0
	18.8	13.8	1.4
	10.0	6.3	1.6
	6.3	3.8	1.7
	12.5	6.3	2.0
	16.3	7.5	2.2
	8.8	3.8	2.3
	6.3	2.5	2.5
	10.0	3.8	2.7
	18.8	6.3	3.0
	12.5	3.8	3.3
	12.5	3.8	3.3
	15.0	3.8	4.0
	52.5	12.5	4.2
	38.8	7.5	5.2
	77.5	12.5	6.2
	180.0	26.3	6.9
	78.8	10.0	7.9
	125.0	15.0	8.3
	118.8	13.8	8.6
	115.0	11.3	10.2
	123.8	11.3	11.0
	268.8	22.5	11.9
	131.3	10.0	13.1
	50.0	3.8	13.3
	262.5	18.8	14.0
	210.0	13.8	15.3
	460.0	25.0	18.4
	458.8	22.5	20.4
	275.0	11.3	24.4
AVE.	89.8	10.8	
STD.DEV.	120.4	6.5	

LAMINATE ID	L (μm)	D (μm)	L/D
24AC	6.3	10.0	0.6
	11.3	13.8	0.8
	8.8	10.0	0.9
	10.0	7.5	1.3
	18.8	13.8	1.4
	8.8	6.3	1.4
	10.0	6.3	1.6
	17.5	10.0	1.8
	12.5	6.3	2.0
	12.5	6.3	2.0
	12.5	6.3	2.0
	16.3	7.5	2.2
	22.5	10.0	2.3
	15.0	6.3	2.4
AVE.	13.0	8.6	
STD.DEV.	4.5	2.7	

Transverse Pore Dimensions of Various Porisity Levels
for AS4/3501-6 12-Ply Laminates

LAMINATE ID	B (μm)	D (μm)	B/D
24AC	8.8	8.8	1.0
	3.8	3.8	1.0
	3.8	3.8	1.0
	10.0	6.3	1.6
	12.5	6.3	2.0
	12.5	6.3	2.0
	10.0	3.8	2.7
AVE.	8.8	5.5	
STD. DEV	3.7	1.9	
12AC	6.3	6.3	1.0
	6.3	6.3	1.0
	7.5	6.3	1.2
	7.5	6.3	1.2
	7.5	6.3	1.2
	25.0	18.8	1.3
	8.8	6.3	1.4
	8.8	6.3	1.4
	17.5	12.5	1.4
	12.5	7.5	1.7
	12.5	7.5	1.7
	12.5	6.3	2.0
AVE.	11.0	8.0	
STD.DEV	5.5	3.8	

LAMINATE ID	B (μm)	D (μm)	B/D
12PRESS	12.5	6.3	2.0
	15.6	12.5	1.3
	9.4	6.3	1.5
	4.4	4.4	1.0
	6.3	5.0	1.3
	20.0	15.6	1.3
	17.5	31.3	0.6
	50.0	17.5	2.9
	25.0	21.9	1.1
	7.5	6.3	1.2
	6.9	6.3	1.1
	12.5	6.3	2.0
	13.8	18.8	0.7
	6.9	6.3	1.1
	12.5	12.5	1.0
	15.6	15.6	1.0

	12.5	9.4	1.3
	6.3	3.1	2.0
	3.1	3.1	1.0
	6.3	7.5	0.8
	3.1	6.3	0.5
	15.6	16.3	1.0
	6.3	6.3	1.0
	6.3	3.8	1.7
	25.0	18.8	1.3
	6.3	6.3	1.0
	3.1	3.1	1.0
	26.3	13.8	1.9
	43.8	25.0	1.8
	15.6	20.0	0.8
	16.3	15.6	1.0
	6.3	6.3	1.0
	28.1	15.6	1.8
	3.8	3.8	1.0
	18.8	18.8	1.0
	12.5	10.0	1.3
	6.3	3.1	2.0
	4.4	9.4	0.5
	25.0	11.9	2.1
	8.8	5.6	1.6
	16.3	11.9	1.4
	25.0	11.9	2.1
	6.3	7.5	0.8
	26.3	18.8	1.4
	11.3	11.3	1.0
AVE.	14.0	11.0	
STD.DEV	10.3	6.6	

LAMINATE ID	B (μm)	D (μm)	B/D
12W	46.9	8.6	5.5
	31.3	19.5	1.6
	30.5	23.4	1.3
	14.1	15.6	0.9
	32.8	7.8	4.2
	14.8	39.1	0.4
	50.0	15.6	3.2
	21.9	18.8	1.2
	23.4	37.5	0.6
	19.5	22.7	0.9
	7.8	6.3	1.3
	6.3	12.5	0.5
	29.7	35.2	0.8
	8.6	7.8	1.1
	11.7	7.8	1.5
	35.2	12.5	2.8
	23.4	9.4	2.5
	76.6	14.1	5.4

35.2	15.6	2.3
62.5	12.5	5.0
12.5	7.8	1.6
5.5	6.3	0.9
9.4	15.6	0.6
25.0	15.6	1.6
13.3	15.6	0.9
56.3	19.5	2.9
50.8	18.0	2.8
53.9	21.9	2.5
15.6	5.5	2.9
17.2	11.7	1.5
35.2	17.2	2.0
4.7	4.7	1.0
21.9	7.8	2.8
17.2	11.7	1.5
14.1	19.5	0.7
43.8	12.5	3.5
23.4	9.4	2.5
37.5	14.1	2.7
29.7	11.7	2.5
12.5	9.4	1.3
10.9	12.5	0.9
18.0	8.6	2.1
76.6	14.1	5.4
15.6	7.8	2.0
29.7	15.6	1.9
3.9	3.9	1.0
18.8	7.8	2.4
75.0	7.8	9.6
20.3	9.4	2.2
39.1	9.4	4.2
39.1	14.1	2.8
27.3	7.8	3.5
32.8	19.5	1.7
14.1	9.4	1.5
19.5	16.4	1.2
11.7	7.8	1.5
18.8	23.4	0.8
11.7	10.9	1.1
43.0	15.6	2.8
27.3	16.4	1.7
10.2	7.8	1.3
15.6	10.2	1.5
42.2	14.1	3.0
55.5	12.5	4.4
39.1	8.6	4.5
7.8	7.8	1.0
32.0	9.4	3.4
25.8	6.3	4.1
37.5	7.8	4.8
12.5	3.9	3.2
10.2	9.4	1.1
24.2	19.5	1.2
11.7	14.1	0.8
3.9	3.9	1.0

	15.6	7.8	2.0
	19.5	11.7	1.7
	7.8	10.2	0.8
	16.4	7.8	2.1
	39.1	19.5	2.0
	50.0	14.1	3.6
	24.2	7.8	3.1
	18.8	9.4	2.0
	10.2	35.9	0.3
	31.3	23.4	1.3
	71.1	7.8	9.1
	19.5	11.7	1.7
	23.4	7.8	3.0
	23.4	15.6	1.5
	33.6	13.3	2.5
	76.6	14.1	5.4
	39.1	9.4	4.2
	11.7	9.4	1.3
	8.6	6.3	1.4
	7.8	5.5	1.4
	18.0	12.5	1.4
	3.9	3.9	1.0
	15.6	3.9	4.0
AVE.	26.3	12.8	
STD.DEV	17.8	7.0	

Apendix 2. Pore Dimensions

Ranges of Transverse Aspect Ratio for Various Porosity Levels of AS4/3501-6 12-Ply Laminates

LAMINATE ID / L/D RANGE	12AC (V_p=.5%)	12P (V_p=2.8%)	12W (V_p=8.7%)	24AC (V_p=.5%)
0.0			0.0	
0.5		2.0	3.0	
1.0	2.0	17.0	17.0	3.0
1.5	7.0	14.0	21.0	
2.0	3.0	9.0	13.0	3.0
2.5		2.0	9.0	
3.0		1.0	12.0	1.0
3.5			6.0	
4.0			2.0	
4.5			5.0	
5.0			3.0	
5.5			4.0	
6.0				
6.5				
7.0				
7.5				
8.0				
8.5				
9.0			1.0	
9.5			1.0	
10.0				

Ranges Of Longitudinal Aspect Ratio For
Various Porosity Levels Of AS4/3501-6 12-Ply Laminates

Laminate ID / L/B RANGE	12AC (V_p=.5%)	12P (V_p=2.8%)	12W (V_p=8.7%)	24AC (V_p=.5%)
0.0				
2.0	6.0	3.0	10.0	11.0
4.0	5.0	5.0	8.0	3.0
6.0		2.0	3.0	
8.0		2.0	3.0	
10.0		1.0	2.0	
12.0		1.0	3.0	
14.0		1.0	3.0	
16.0		2.0	1.0	
18.0				
20.0			2.0	
22.0				
24.0			1.0	
26.0				

Appendix 3. Differential Scanning Calorimetry Data

(Liquid Water Content of Pores at Saturation)

Specimen I.D.	Treatment	% Pore Volume Filled with Liquid Water
12AC1	None	.031
12AC2	None	.015
12P1	None	.34
12P2	None	.25
12W1	None	1.84
12W2	None	1.75
12W3	None	1.7
12W1	Polished*	1.3
12W2	Polished*	2.4

* Interior 50% of material only; edges and surfaces sanded away.

Representative DSC Curves from Three Primary Materials

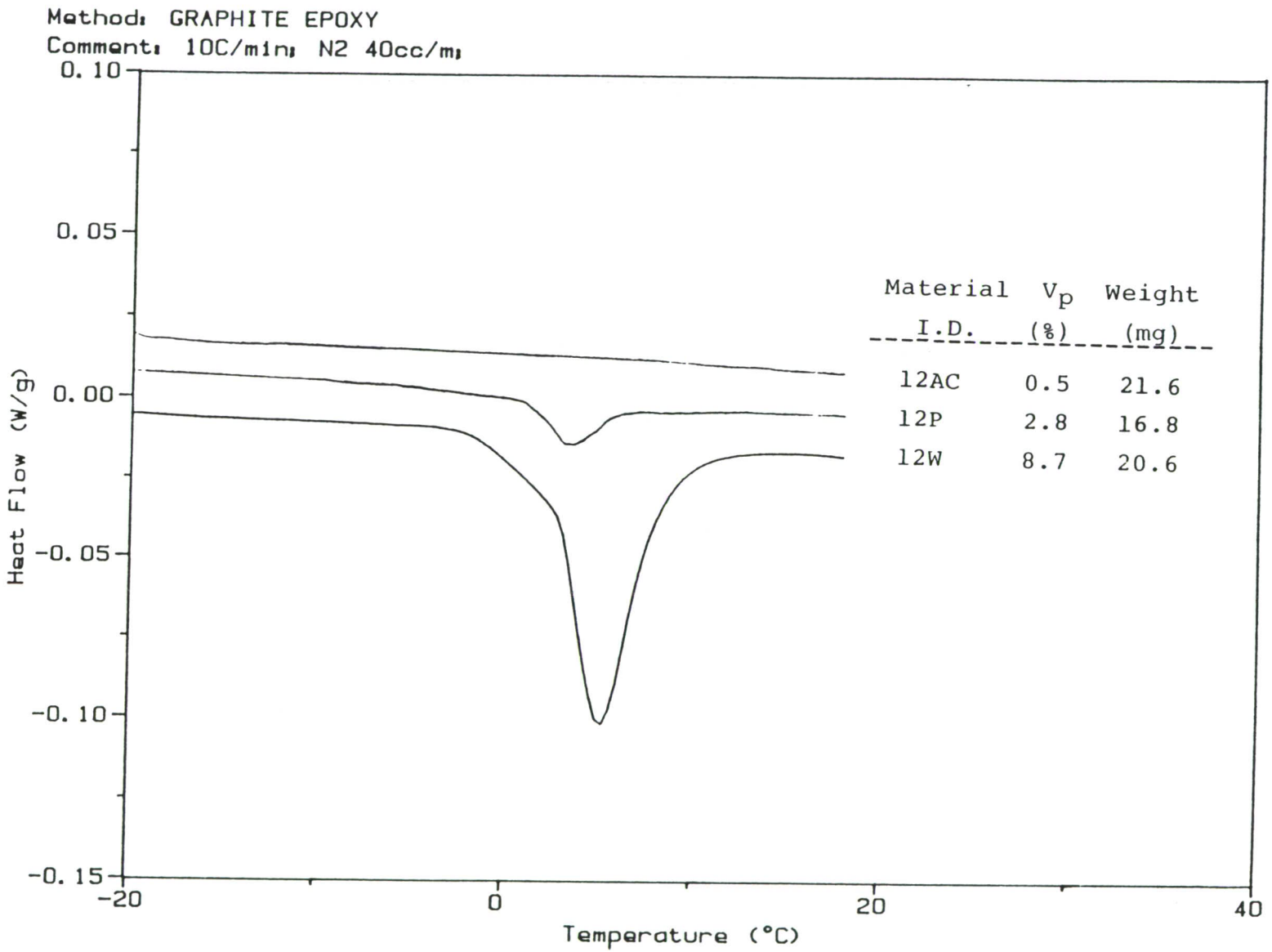

Appendix 4. Short Beam Fatigue Data

1. Material 12AC (V_p = 0.5%) Average ILSS (S_o) = 115 MPa

Log N(cycles)	S(MPa)	S/S_o	S/Intercept
			INTERCEPT 113.00
2.85	92.00	0.78	0.81
2.15	92.00	0.78	0.81
3.41	92.00	0.78	0.81
3.05	87.00	0.74	0.77
3.44	87.00	0.74	0.77
2.67	87.00	0.74	0.77
3.91	87.00	0.74	0.77
3.75	82.00	0.70	0.73
4.01	82.00	0.70	0.73
4.51	82.00	0.70	0.73
4.46	72.00	0.61	0.64
5.62	68.00	0.58	0.60
5.19	68.00	0.58	0.60
5.37	68.00	0.58	0.60
0.00	121.00	1.05	
0.00	113.00	0.96	
0.00	117.00	0.99	

S-N Curve Normalized by the Average Static ILSS, Forced Through S/S_o = 1.0 at 1 Cycle

Parameter	Estimate	Standard Error	T Value	Prob. Level
Intercept	0.996375	7.69318E-3	129.514	0
Slope	-0.0774326	2.36581E-3	-32.7299	0

Analysis of Variance

Source	Sum of Squares	Df	Mean Square	F-Ratio	Prob. Level
Model	.7017	1	.7017	1071.2431	.00000
Error	.015065	23	.000655		
Total (Corr.)	.716736	24			

Correlation Coefficient = -0.989438 R-squared = 97.90 percent
Stnd. Error of Est. = 0.0255931

2. Material 12P (V_p=2.8%) Average ILSS (S_o) = 93 MPa

Log N(Cycles)	S(MPa)	S/S_o	S/Intercept
			INTERCEPT 94.00
4.67	63.00	0.68	0.67
3.00	72.00	0.78	0.77
2.94	72.00	0.78	0.77
3.26	72.00	0.78	0.77
2.60	77.00	0.84	0.82
1.78	77.00	0.84	0.82
2.30	77.00	0.84	0.82
4.41	58.00	0.63	0.62
4.20	58.00	0.63	0.62
5.30	53.00	0.58	0.56
0.00	94.00	1.02	
0.00	92.00	1.00	
0.00	90.00	0.98	

S-N Curve Normalized by the Average Static ILSS, Forced Through S/S_o= 1.0 at 1 cycle

Parameter	Estimate	Standard Error	T Value	Prob. Level
Intercept	1.00641	8.2476E-3	122.025	0
Slope	-0.0738312	2.85868E-3	-25.827	1.11023E-15

Analysis of Variance

Source	Sum of Squares	Df	Mean Square	F-Ratio	Prob. Level
Model	.46130	1	.46130	667.03892	.00000
Error	.012448	18	.000692		
Total (Corr.)	.473749	19			

Correlation Coefficient = -0.986775
Stnd. Error of Est. = 0.0262977

R-squared = 97.37 percent

3. Material 12W (V_p = 8.7%)

Average ILSS (S_o) = 75.23 (MPa)

Log N(cycles)	S(MPa)	S/S_o	S/Intercept
			INTERCEPT 78.00
2.38	63.00	0.84	0.81
2.15	63.00	0.84	0.81
2.04	63.00	0.84	0.81
3.94	48.50	0.64	0.62
3.83	48.50	0.64	0.62
5.63	38.70	0.51	0.50
5.39	38.70	0.51	0.50
6.00	33.90	0.45	0.43
2.90	55.00	0.73	0.71
5.10	45.00	0.60	0.58
0.00	75.00	1.00	
0.00	72.40	0.96	
0.00	78.30	1.04	

S-N Curve Normalized by the Average Static ILSS, Forced Through S/S_o = 1.0 at 1 cycle

Parameter	Estimate	Standard Error	T Value	Prob. Level
Intercept	1.00252	4.39654E-3	228.543	0
Slope	-0.0692e-3	1.4795E-3	-50.2837	0

Analysis of Variance

Source	Sum of Squares	Df	Mean Square	F-Ratio	Prob. Level
Model	.7912	1	.7912	3675.2362	.00000
Error	.003875	18	.000215		
Total (Corr.)	.795080	19			

Correlation Coefficient = -0.99756 R-squared = 99.51 percent
Stnd. Error of Est. = 0.0146724

4. Material 12AC (V_p = 0.5%) (Wet)

Average ILSS (S_o) = 93.7 (MPa)

Log N (cycles)	S (MPa)	S/S_o	S/Intercept
			INTERCEPT 99.80
2.63	80.00	0.85	0.80
3.33	80.00	0.85	0.80
2.54	80.00	0.85	0.80
3.91	75.00	0.80	0.75
3.53	75.00	0.80	0.75
4.01	75.00	0.80	0.75
3.92	71.00	0.76	0.71
3.62	71.00	0.76	0.71
3.84	71.00	0.76	0.71
4.17	71.00	0.76	0.71
4.26	66.00	0.70	0.66
4.02	66.00	0.70	0.66
4.06	66.00	0.70	0.66
4.19	66.00	0.70	0.66
5.23	62.00	0.66	0.62
4.95	62.00	0.66	0.62
4.65	62.00	0.66	0.62
6.00	58.00	0.62	0.58
0.00	90.00	0.96	
0.00	91.00	0.97	
0.00	100.00	1.07	

S-N Curve Normalized by the Average Static ILSS, Forced Through S/S_o = 1.0 at 1 cycle

Parameter	Estimate	Standard Error	T Value	Prob. Level
Intercept	1.00333	7.40965E-3	135.408	0
Slope	-0.0637271	2.83876E-3	-22.4553	0

Analysis of Variance

Source	Sum of Squares	Df	Mean Square	F-Ratio	Prob. Level
Model	.47566	1	.47566	810.27472	.00000
Error	.015243	26	.000587		
Total (Corr.)	.490925	27			

Correlation Coefficient = -0.984332 R-squared = 96.89 percent

Stnd. Error of Est. = 0.0242289

5. Material 12W (V_p=8.7%) (Wet)

Average ILSS (S_o) = 58.0 (MPa)

Log N (cycles)	S (MPa)	S/S_o	S/Intercept
			INTERCEPT 62.00
0.19	48.50	0.84	0.78
2.30	48.50	0.84	0.78
3.66	38.50	0.66	0.62
4.88	29.00	0.50	0.47
5.20	29.00	0.50	0.47
5.52	29.00	0.50	0.47
5.78	24.30	0.42	0.39
2.08	48.00	0.83	0.77
3.71	38.50	0.66	0.62
3.44	38.50	0.66	0.62
6.00	19.00	0.33	0.31
6.00	24.00	0.41	0.39
3.28	38.50	0.66	0.62
4.15	38.50	0.66	0.62
4.10	38.50	0.66	0.62
0.00	59.00	1.02	
0.00	60.00	1.03	
0.00	58.00	1.00	
0.00	55.00	0.95	

S-N Curve Normalized by the Average Static ILSS, Forced Through S/S_o = 1.0 at 1 cycle

Parameter	Estimate	Standard Error	T Value	Prob. Level
Intercept	1.01014	0.0105195	95.1814	0
Slope	-0.0974752	3.15217E-3	-30.9313	0

Analysis of Variance

Source	Sum of Squares	Df	Mean Square	F-Ratio	Prob. Level
Model	1.23503	1	1.23503	956.24652	.00000
Error	.029705	23	.001292		
Total (Corr.)	1.264736	24			

Correlation Coefficient = -0.988186 R-squared = 97.65 percent
Stnd. Error of Est. = 0.035938

Appendix 5. Mode I Crack Growth Data

1. Material 12AC (V_p = 0.5%) (G_{Ic} = 258.3 J/m^2)

G_{Imax} (J/m^2)	Log $G_{Imax.}$ (J/m^2)	Log (G_{Imax}/G_{Ic})	Log ($\Delta a/\Delta n$) (mm/cycle)
125.89	2.10	-0.31	-5.18
151.36	2.18	-0.23	-3.78
102.33	2.01	-0.40	-5.55
190.55	2.28	-0.13	-2.16
169.82	2.23	-0.18	-3.16
154.88	2.19	-0.22	-4.41
165.96	2.22	-0.19	-4.75
218.78	2.34	-0.07	-3.69
213.80	2.33	-0.08	-3.05
251.19	2.40	-0.01	-1.74
234.42	2.37	-0.04	-2.15
218.78	2.34	-0.07	-2.44
213.80	2.33	-0.08	-2.72
190.55	2.28	-0.13	-3.66
181.97	2.26	-0.15	-4.24

2. Material 12AC (Wet)

G_{Ic} = 569.0 J/m^2

G_{Imax} (J/m^2)	Log $G_{Imax.}$ (J/m^2)	Log ($G_{Imax.}/G_{Ic}$)	Log ($\Delta a/\Delta n$) (mm/cycle)
302.00	2.48	-0.22	-2.70
380.19	2.58	-0.12	-2.41
524.81	2.72	-0.02	-1.63
338.84	2.53	-0.17	-3.58
213.80	2.33	-0.37	-3.40
204.17	2.31	-0.39	-4.57
251.19	2.40	-0.30	-4.43
275.42	2.44	-0.26	-3.17
218.78	2.34	-0.36	-2.66
165.96	2.22	-0.48	-4.12
169.82	2.23	-0.47	-4.01
199.53	2.30	-0.40	-4.03
234.42	2.37	-0.33	-3.18
162.18	2.21	-0.49	-4.12
138.04	2.14	-0.56	-4.93
194.98	2.29	-0.41	-4.16

3. Material 12W (V_p = 8.7%)

G_{Ic} = 471 J/m^2

G_{Imax} (J/m^2)	Log $G_{Imax.}$ (J/m^2)	Log (G_{Imax}/G_{Ic})	Log ($\Delta a/\Delta n$) (mm/cycle)
245.47	2.39	-0.40	-3.72
380.19	2.58	-0.21	-3.10
389.05	2.59	-0.20	-3.20
457.09	2.66	-0.13	-2.12
478.63	2.68	-0.11	-2.40
537.03	2.73	-0.06	-1.72
177.83	2.25	-0.54	-5.12
208.93	2.32	-0.47	-4.66
213.80	2.33	-0.46	-4.81
295.12	2.47	-0.32	-3.48
380.19	2.58	-0.21	-2.67
407.38	2.61	-0.18	-2.75
446.68	2.65	-0.14	-2.58
501.19	2.70	-0.09	-2.31
524.81	2.72	-0.07	-2.05
436.52	2.64	-0.15	-2.46
302.00	2.48	-0.31	-4.09

4. Material 12W (Wet)

G_{Ic} = 663.0 J/m^2

G_{Imax} (J/m^2)	Log $G_{Imax.}$ (J/m^2)	Log (G_{Imax}/G_{Ic})	Log ($\Delta a/\Delta n$) (mm/cycle)
354.81	2.55	-0.27	-3.00
363.08	2.56	-0.26	-2.79
316.23	2.50	-0.32	-3.30
263.03	2.42	-0.40	-4.17
234.42	2.37	-0.45	-4.70
245.47	2.39	-0.43	-4.85
501.19	2.70	-0.12	-2.49
549.54	2.74	-0.08	-2.40
478.63	2.68	-0.14	-3.00
436.52	2.64	-0.18	-3.48
257.04	2.41	-0.41	-4.00
295.12	2.47	-0.35	-4.44
380.19	2.58	-0.24	-3.42
524.81	2.72	-0.10	-2.74
275.42	2.44	-0.38	-4.26
177.83	2.25	-0.57	-5.00

Appendix 6. Mode II Crack Growth Data

1. Material 12AC (V_p = 0.5%)

Log G_{IImax} (J/m^2)	Log $\Delta a/\Delta n$ (mm/cycle)
2.49	-2.47
2.27	-3.45
2.26	-3.98
2.13	-4.71
2.12	-5.04
2.0	-5.44
2.43	-2.77
2.36	-2.95
2.21	-4.33
2.18	-4.23
2.22	-4.17
2.47	-2.49
2.51	-2.45
2.47	-2.48
1.95	-5.19
1.97	-5.17

2. Material 12P (V_p = 2.8%)

Log G_{IImax} (J/m^2)	Log $\Delta a/\Delta n$ (mm/cycle)
2.04	-5.68
2.03	-5.79
2.21	-4.71
2.2	-4.36
2.29	-3.5
2.34	-3.43
2.26	-4.1
2.35	-3.85
2.39	-3.47
2.45	-3.21
2.45	-3.12
2.45	-3.12
2.45	-3.38
2.45	-3.29
2.5	-2.78
2.53	-2.08
2.41	-3.15
2.39	-3.58
2.39	-3.68
2.23	-4.28
2.25	-3.64
2.24	-3.9
2.07	-5.19
2.22	-5.07

3. Material 12W (V_p = 8.7%)

Log G_{IImax} (J/m^2)	Log $\Delta a/\Delta n$ (mm/cycle)
2.1	-4.15
2.19	-3.28
2.19	-3.22
2.39	-2.79
2.03	-4.85
2.43	-2.23
1.98	-4.5
1.99	-4.75
2.15	-3.7
2.28	-2.49
2.05	-3.84
2.06	-4.87
2.13	-3.59
2	-4.97
2.42	-2.48
2.32	-2.91
2.29	-2.73
2.03	-4.34
2.39	-2.63
2.41	-2.6

4. Material 12 AC (V_p = 0.5%) (Wet)

Log G_{IImax} (J/m^2)	Log $\Delta a/\Delta n$ (mm/cycle)
2.08	-3.6
1.98	-3.64
2.26	-2.6
2.34	-2.36
2.31	-2.66
2.37	-2.63
2.36	-2.32
2.35	-2.78
2.41	-2.4
2.19	-2.73
2.22	-3.21
2.03	-4.04
1.98	-4.14
1.99	-3.75
1.77	-5.7
1.88	-5.28
1.92	-4.82
2.29	-2.6
2.27	-3.3
1.86	-4.99
1.9	-4.77

5. Material 12W (V_p = 8.7%) (Wet)

Log G_{IImax} (J/m^2)	Log $\Delta a/\Delta n$ (mm/cycle)
2.15	-3.14
2.09	-3.56
2.21	-2.58
2.27	-2.46
2.31	-2.24
2.3	-2.04
1.87	-4.03
1.98	-3.49
1.94	-4.2
1.94	-3.58
1.94	-4.08
1.89	-4
1.88	-3.92
1.89	-3.83
1.61	-5.11
1.66	-5.0
1.8	-4.55

U.S. GOVERNMENT PRINTING OFFICE 750-113